^{57}Fe MÖSSBAUER INVESTIGATIONS IN DIAMOND, SiGe AND Ge SINGLE CRYSTALS

Deena Naidoo

Submitted in fulfilment of the academic requirements for the degree of Doctor of Philosophy in the School of Physics, University of KwaZulu-Natal (UKZN).

September 2006

Abstract

In the projects presented in this thesis, Mössbauer Spectroscopy is employed as an investigative tool in which ion implanted ^{57}Fe is used as a probe. Hyperfine interactions measured by this method provide information on isomer shift, the electric field gradient and the magnetic field at the implanted probe nucleus. In the case of non-magnetic crystalline material, the Mössbauer parameters of importance are the isomer shift and the electric quadrupole splitting of the spectral components required to fit the spectra. The dynamics and the vibrational behaviour of the implanted atoms can be monitored and information of its electronic structure, their positions in the host matrix and local environment can be deduced. The isomer shift of the Mössbauer spectral lines gives a measure of the *s*-electron density at the probe, its dependence on temperature and a measure of the Debye temperature of probe ions at their sites in the crystalline lattice. This serves as a means to differentiate between probe ions at substitutional and interstitial sites. The quadrupole splitting gives a measure of the interaction of the quadrupole moment of the ^{57}Fe nucleus in the 14.4 keV excited state with the electric field gradient created at the nucleus by the electronic shell and by neighbouring ions which gives an indication of the valence of the ion.

The following measurements were performed:

(a) Source based Conversion Electron Mössbauer Spectroscopy on High-Temperature High-Pressure (HTHP) and Chemical Vapour Deposition (CVD) synthesized diamonds which were implanted with 5×10^{14} ^{57}Fe ions/cm^2.

(b) ^{57}Fe Mössbauer Spectroscopy investigations on diamond (Type IIa and Chemical Vapour Deposition) following implantation of $^{57}Mn^*$, and

(c) ^{57}Fe Mössbauer Spectroscopy investigations on $Si_{1-x}Ge_x$ single crystals following implantation of $^{57}Mn^*$.

The spectra for all diamond samples at temperatures < 500 K were dominated by two broad doublets (D1 and D2) associated with Fe atoms resting at low-symmetry defect sites. An additional doublet (D3) was included at the wings of the resonance spectra for the Conversion Electron Mössbauer Spectroscopy (CEMS) measurements on

High-Temperature High-Pressure (HTHP) synthesized diamond which could be due to Fe-N complexes. A sudden collapse of the resonance spectra was observed in the Conversion Electron Mössbauer Spectroscopy (CEMS) measurements on Chemical Vapour Deposition synthesized diamond indicative that a large fraction of the implanted Fe, presumably in graphitized complexes close to the grain surface, had diffused out of the sample. At the highest temperatures, the high-symmetry component (S1) was clearly evident in the Mössbauer Spectroscopy following implantation of ^{57}Mn measurements on the diamond samples due to the annealing of implantation damage. The isomer shift and quadrupole splitting values of the spectral components are in good agreement with the In-Beam Mössbauer Spectroscopy (IBMS) results obtained by Bharuth-Ram *et al.* and also with the data obtained by de Waard and co-workers. Further, our results compares well with the theoretical calculations performed within local density approximation of spin-density functional theory (LSDA) for the interstitial Fe, however, the isomer shift of single line, S1 differs from the theoretical values of substitutional Fe since the approximations has limitations to take into account the high compressional forces acting on the *s*-electron shell of the substitutional Fe.

The Mössbauer spectra recorded after implantation of ^{57}Mn into n-type $Si_{1-x}Ge_x$ ($x = 0.017$, 0.05 and 0.10), p-type $Si_{1-x}Ge_x$ ($x = 0.024$, 0.083, 0.20 and 0.50) and intrinsic $Si_{1-x}Ge_x$ ($x = 0.80$ and 1.0) single crystals held at 300-850 K in the implantation chamber were generally characterized by sites assigned to damage, tetrahedral interstitial Fe, substitutional Fe and Fe_i-V pairs. The diffusion coefficients for neutral and ionized interstitial Fe have been determined from temperature dependent line broadening and our data show that diffusivity of Fe_i^+ is larger than that of Fe_i^0 for $Si_{1-x}Ge_x$ ($x \leq 0.50$) as in the case of Si. The Debye temperatures of the different spectral components compares well with the theoretical values determined by the mass defect approximation. Our results presented in this thesis show that the spectral features, electronic and vibrational properties for $0.017 \leq x \leq 0.50$ shows very similar resemblance to silicon whilst for $x = 0.80$ is comparable to Ge. A comparison of the hyperfine results between diamond, Si, SiGe alloys, Ge and α-Sn shows a linear dependence between the hyperfine parameters (isomer shifts and quadrupole splittings) and the bond lengths.

Preface

The measurements described in this thesis were carried out at the Institut für Kernphysik, Darmstadt, Germany, and at the online isotope separator facility, ISOLDE, at CERN, Geneva. The work at CERN was carried out within the Aarhus University (Denmark), University of KwaZulu-Natal (Durban), Laboratorio MDM-INFM (Italy) and Hahn-Meitner Institute (Germany) collaboration.

This thesis is being submitted for the degree of Doctor of Philosophy in the University of KwaZulu-Natal, Durban and has not been submitted before for any degree or diploma examination in any other tertiary institution.

The data analysis and interpretation is my original work, and were carried out under the supervision of Professor K. Bharuth-Ram.

The work of other scientists is duly acknowledged in the text when used as a reference.

(Signature of Candidate)

18 Th Day of September 20 06

Acknowledgements

I am grateful to my supervisor, Professor K. Bharuth-Ram, for his guidance, patience and constant encouragement throughout this project. Further, I thank Prof. Bharuth-Ram for introducing me to the field of Nuclear Solid State Physics, and in particular Mössbauer Spectroscopy, and giving me an opportunity to carry out research in leading experimental facilities around the world.

This work would not be possible without the assistance provided by my inspiring friend and former colleague, Dr V.V. Naicker, in particular in developing a method to analyze the complex spectra. I would also like to express my sincere appreciation to my colleagues of the School of Physics, University of the Witwatersrand, and in particular Sanjeev Shrivastava, Mervin Naidoo, Dr J. Keartland, Dr C. Albers and Phil Ferrer for their help, useful suggestions, and stimulating discussions during my research program.

I am also indebted to Dr H.P. Gunnlaugsson and Professor G. Weyer from Aarhus University, Denmark for their invaluable assistance provided during the experimental work, as well as the partners in the collaboration and the students with whom I interacted at CERN, and to Dr Jim Butler of the Naval Research ZLabs., Washington, who supplied the synthetic diamonds used in this study.

I am grateful for the financial assistance of the National Research Foundation (NRF) and the University Bursary Scheme.

I would like to take this opportunity to express my deepest gratitude to my wife, Essavanie, my children, Sebastian and Mercia who have been a continual source of support and encouragement during the years as a student. Finally, I would like to thank my parents both for their financial and moral support during my education.

LIST OF CONTENTS

List of Figures

List of Tables

List of Abbreviations/Acronyms/Symbols

MS	:	Mössbauer Spectroscopy
UV	:	Ultraviolet
IR	:	Infrared
HTHP	:	High-Temperature High Pressure
CVD	:	Chemical Vapour Deposition
ESR	:	Electron Spin Resonance
CMOS	:	Complimentary metal-oxide semiconductor
IC	:	Integrated Circuits
GPS	:	Global Position Systems
TDPAD	:	Time Differential Perturbed Angular distributions
PAC	:	Perturbed Angular Correlations
EC	:	Emission Channeling
IBMS	:	In-Beam Mössbauer Spectroscopy
FWHM	:	Full Width Half Maximum
TMS	:	Mössbauer Spectroscopy in transmission geometry
CEMS	:	Conversion Electron Mössbauer Spectroscopy
SCA	:	Single-channel analyzer
PPAC	:	Parallel plate avalanche counter
ISOLDE	:	Isotope Separator On Line
LHC	:	Large Hadron Collider
PS	:	Proton Synchrotron
SPS	:	Super Proton Synchrotron
NTOF	:	Neutron Time-of-Flight
AD	:	Antiproton Decelerator
PSB	:	Proton-Synchrotron Booster
GPS	:	General Purpose Booster
HRS	:	High Resolution Separator

XRD	:	X-ray diffraction
MVBA	:	Microsoft Visual Basic Applications
xVBF	:	Extended Voigt-based fitting
HWHM	:	Half width half maximum
c-silicon	:	Crystalline silicon
a-silicon	:	Amorphous silicon
nn	:	Nearest neighborhood
a_o	:	Lattice parameter
E_g	:	Energy gap
τ	:	Mean lifetime
$t_{1/2}$	:	Half-life
I	:	Nuclear spin quantum number
ω_E	:	Einstein frequency
f	:	Recoil-free fraction
θ_D	:	Debye temperature
E0	:	Electric monopole interaction
E2	:	Electric quadrupole interaction
M1	:	Magnetic dipole interaction
δ	:	Isomer shift
ΔE_Q	:	Electric quadrupole splitting
ΔE_M	:	Magnetic splitting
E_I	:	Electric monopole interaction
E_Q	:	Electric quadrupole interaction
SOD	:	Second-order Doppler Shift
eQ	:	Electric quadrupole moment
EFG	:	Electric field gradient
η	:	Asymmetry parameter
m_I	:	Nuclear magnetic spin quantum number

$\vec{\mu}$	:	Magnetic dipole moment
$\vec{H}$	:	Magnetic field
g_N	:	Nuclear Lande' factor
β_N	:	Nuclear magneton
α	:	Internal conversion coefficient

Chapter 1

INTRODUCTION

1.1 Properties of Diamond and Applications

Diamond has been prized for centuries as the most fascinating gemstone of exceptional brilliance and lustre. To scientists, however, diamond is interesting for its wide range of exceptional and extreme properties. As well has being regarded as the hardest material[1] (Knoop's hardness of 10.40 $kgmm^{-2}$), it is the least compressible[1] (Bulk modulus >110 GPa), the stiffest material[1] (Young's modulus >1.2 GPa), and is an excellent thermal conductor[1] (k = 20 $Wcm^{-1}K^{-1}$ for pure diamond) with extremely low thermal expansion[1] $\left(\alpha = 1.05 \times 10^{-6}\ K^{-1} \text{ at } 300\ K\right)$. It is chemically inert and wear resistant to heat, most acids and radiation, offers low friction and is optically transparent from ultra-violet (UV) to the far infrared (IR). In terms of hardness, only boron nitride comes close with a Knoop's hardness of 4.5 $kg.mm^{-2}$. Diamond has a wide band gap of 5.48 eV, and high mobility for both p and n-type carriers. These properties, coupled with those mentioned above make diamond an ideal material for a variety of scientific and technological applications, in particular as a base for the fabrication of semiconducting and opto-electronic devices. Some of the properties of diamond are listed in Table 1.1, together with those of the group IV elements silicon and germanium.

Table 1.1 : Some properties of Diamond, Silicon and Germanium[2-6].

PROPERTY/MATERIAL	DIAMOND	SILICON	GERMANIUM
Structure (All Cubic)	Fd3m	Fd3m	Fd3m
Lattice Parmeter a_o at 300 K	0.35668 nm	0.54311 nm	0.56579 nm
Nearest Neighbour Distance at 300 K	0.15445 nm	0.235 nm	0.245 nm
Density at 300 K	3.51525 g cm^{-3}	2.3290 g cm^{-3}	5.3234 g cm^{-3}
Atomic Concentration at 300 K	1.763×10^{23} cm^{-3}	5.00×10^{22} cm^{-3}	4.42×10^{22} cm^{-3}
Linear Expansion Coefficient at 300 K	1.05×10^{-6} K^{-1}	2.6×10^{-6} K^{-1}	5.8×10^{-6} K^{-1}
Melting Point	3773 K	1683 K	1210 K
Energy Gap, E_g at 300 K	5.48 eV	1.12 eV	0.66 eV
Dielectric constant at 300 K	5.70	11.9	16.0
Electron Hall Mobility at 300 K	2800 $cm^2V^{-1}s^{-1}$	1600 $cm^2V^{-1}s^{-1}$ for $p = 1.0\times10^{14}$ cm^{-3}	3900 $cm^2V^{-1}s^{-1}$ for $n = 1.0\times10^{15}$ cm^{-3}
Hole Mobility at 300 K	130 to 2010 $cm^2V^{-1}s^{-1}$	430 $cm^2V^{-1}s^{-1}$ for $p = 1.0\times10^{14}$ cm^{-3}	1900 $cm^2V^{-1}s^{-1}$ for $n = 1.0\times10^{15}$ cm^{-3}

1.1.1 Classification of Diamond

Diamonds are classified into two types, namely Type I and Type II, according to their nitrogen concentrations, crystalline perfection and by their absorption features in the IR, visible and UV regions of the electromagnetic spectrum[7-9]. Most natural diamonds are

Type I and have their absorption edge at 330 nm, while Type II has their edge at 220 nm. Platelike features (platelets) have been observed in Type I diamonds and varies markedly in size and density from specimen to specimen but are absent in Type II diamonds. Type I diamond contains high concentration of nitrogen which preferably occupies substitutional sites in the carbon lattices. Type Ib diamonds produce electron spin resonance (ESR) signals, whilst Type Ia do not. Diamonds that show no infrared absorption are classified as Type II. Type IIa contain so little nitrogen that it is not easily detected by usual IR or UV absorption measurements. According to the classification of Custers[10-11], Type IIa diamonds are good electrical insulators whilst Type IIb diamonds shows semiconductivity, occasionally accompanied by blue colour. Nitrogen is an unintended but common impurity found in synthetic diamond and can be eliminated or drastically reduced by adding dopants such as Al, Ti and Zr in the synthesis process. Table 1.2 shows some of the main points of classification of diamond.

Table 1.2: Diamond Types and Nitrogen content.

Type	Abundance	Nitrogen
Ia	98% of natural	Nitrogen up to 0.3% (i.e. 10^{19} to 10^{20} atoms.cm^{-3})
Ib	Very rare in nature (0.1%) Mainly synthetic	A and B aggregates; Low levels of single N atoms (< 10^{16} atoms.cm^{-3}); platelets
IIa	Very rare in nature (2%)	Very low Nitrogen level
IIb		Extremely low Nitrogen level; Semiconducting due to Boron acceptors.

Type II diamonds are transparent in the range $220\,\text{nm} - 6\,\mu\text{m}$ whilst Type I from $330\,\text{nm} - 10\,\mu\text{m}$. The most common colours are yellow and brown which are due to the absorption band in the visible range of the electromagnetic spectrum. Type I are predominately yellowish in colour associated with the substitutional nitrogen impurity. Colourless diamonds are rare and the most valuable gemstone.

Natural diamonds are rare and very expensive for technological applications and have been supplemented with synthetic (industrial) diamonds which are economically more viable. Synthetic diamonds are produced essentially by two methods viz. High-Temperature and High-Pressure (HTHP) and Chemical Vapour Deposition (CVD). Synthetic diamond resembles natural diamonds in the most fundamental properties but may differ in size, shape and impurities. HTHP diamonds are synthesised by either the solvent-crystal approach or the reconstitution method in a "belt type apparatus[12-14]" when carbonaceous material (graphite or diamond grit) is dissolved in molten iron or nickel and is subjected to temperatures above 1800 K and pressures of the order of 60 kbar. Single-crystal diamonds of good quality (inclusion-free) and appreciable size are produced at faster growth times and lower costs using the latter technique. Diamonds which are free of inclusions appear yellowish in colour because of the impurity nitrogen atoms which are present within the starting materials in the reaction chamber and are incorporated in the diamond lattice during the crystallization process. In a number of experiments[15], colourless diamonds have been produced by initially doping the starting material with certain elements to remove the impurity atoms. Semiconducting diamonds were produced[15,16] by doping the starting materials with boron.

CVD diamond is synthesized when a gas of organic compound, such as methane, containing carbon is dissociated at low temperature (25 to 250 °C) low pressure ($\frac{1}{10}$ of atmospheric pressure) under which diamond is thermodynamically stable and then deposited on a substrate maintained at a temperature between 800 to 1000 °C. If the substrate is made of a single crystal diamond, then a single crystal grows, when the substrate is made of silicon, tungsten or molybdenum, polycrystalline diamond (a few millimetres thick), in the form of intergrown microcrystallites is produced. A huge amount of energy is required to activate the source gas and methods such as hot filament, microwave plasma, high frequency and combustion-flame methods have been employed. The microwave plasma method is suitable to synthesize high-quality single crystals of appreciable sizes. CVD diamonds exhibits the extreme chemical and physical properties of

natural and HTHP synthetic diamond viz. chemically inert, outstanding thermal conductivity and excellent abrasive resistance. Compared to the HTHP method, the CVD method uses a small and simple device and can be used for coating in any form of polycrystalline diamond, and therefore can be applied as coating of machine equipment, and heat sinks of semiconductor devices.

1.1.2 Uses of Diamond

The high thermal conductivity of diamond (about five times that of copper) and its extreme hardness make it ideally suited for industrial applications such as in machining, grinding, cutting and polishing tools. Type II diamonds have the highest thermal conductivity whereas other types have lower conductivities due to impurities, nitrogen aggregates, platelets and dislocations. Good quality synthetic diamonds have a similar conductivity to natural diamond. Undoped diamond has an energy gap of 5.48 eV, a low specific heat, therefore a good insulator and is an excellent conductor of heat which makes it an excellent substrate for a variety of electronic devices. CVD diamond based devices such as radiation detectors, transistors and electron emitters are currently in the market and HTHP diamonds are being used for thermally conducting substrates in semiconducting devices. Type IIb diamonds are p-type semiconductors and the acceptor centre is a substitutional boron.

The extreme strength and chemical inertness of diamond coupled with its spectral transmission range makes diamond an ideal material in the field of optical applications. Some applications of active devices include optoelectro-switches, lasers, optical fibres and microwave diodes are currently being used in military applications. CVD diamond has improved the field of IR optics by being ultra-hard as compared to the conventional materials such as Ge and ZnS which have excellent transmission characteristics but are brittle and vulnerable to abrasion and erosion. Research is in progress to improve the

surface of polycrystalline CVD diamond with the aim of reducing the attenuation and the transmission of IR signals.

1.2 Properties of Silicon, Germanium and Silicon Germanium

Diamond, silicon and germanium have the same cubic structure as shown in Table 1.1 and therefore a comparison of their properties have been made, in particular their semiconducting abilities. Silicon and germanium were the first two elemental semiconductors and it is silicon that has been the most widely examined material in science and technology. Silicon has dominated (> 90% sales) the semiconductor global market with electronic devices for many years due to its large bandgap (1.12 eV), low manufacturing cost and because of the superior enhanced insulating properties of stable natural SiO_2 as compared to GeO_2. The combination of the chemical, mechanical and electrical properties of SiO_2 are vital to the fabrication of transistors and to reduce leakage currents. The inherent properties of silicon coupled with the unique properties of SiO_2 gives it the edge as compared to faster materials (high speed IC devices) such as GaAs and other group III-V semiconductor compounds. Further, it is more expensive to fabricate devices from group III-V materials because of different processing techniques as compared to the Si complimentary metal-oxide semiconductor (CMOS) which is 200 times cheaper than GaAs per square mm. Germanium is a very important semiconductor which with small amounts of As and Ga can be used as transistors and integrated circuits (IC). Also when Ge oxide is added to glass it increases the index of refraction of glass which can then be used as wide-angle lenses in optical instruments.

By replacing a fraction of Si with Ge, it is possible to design a wide variety of electronic devices at the same cost of silicon. Silicon germanium ($Si_{1-x}Ge_x$), known as "Siggie" by industrialists, has a bandgap in the range 1.12 to 0.67 eV[17] and can be grown onto silicon wafers in which the electrical properties of silicon are combined with germanium to design

chips to operate more efficiently. SiGe processing is relatively simple because Si and Ge have similar chemical and physical properties and is usually produced by chemical vapour deposition at low temperature and low costs. The operating frequency, current, noise, and power capabilities of transistors have improved vastly when germanium is used as a base layer. Therefore, SiGe is ideal for low-cost, low-power, low-frequency silicon chips as compared to high-cost and high-power, high-frequency chips fabricated from III-V semiconductor materials such as GaAs and InP. Silicon operates at frequencies less than a few GHz and is therefore not suitable for very high speed wireless telecommunications devices. The size of chips in circuitry are currently being made smaller and smaller to achieve greater speeds, silicon chips will not be able to cope hence SiGe with speeds of up to 120 GHz (4.3 trillionths of a second) will be the future technology. SiGe offers manufacturers the possibilities to reengineer the bandgap of silicon for higher performance resulting in a heterojunction system that is comparable with silicon. Even though silicon and germanium have the same crystal structure, their lattice constants differs by 4% and hence introducing larger germanium atoms into silicon causes its structure to expand and become strained to create the alloy. It is the stress that modifies the bandgap. Therefore, it is expected that the growth in the semiconductor industry in high-speed optical networking and inexpensive, lightweight personal-communication devices will be addressed not by Si or GaAs based devices but rather SiGe is expected to dominate the future of wireless and integrated circuits. This technology increases the operating speed, reduces electronic noise, lowers power consumption, supports higher levels of integration, and enables the design of more functional components on a chip. Future applications of SiGe could include the creation of new powerful microcommunication devices such as single-chip, watch-sized cellular phones, Global Position Systems (GPS), and faster Internet access in a single package.

In order to fully realize these applications, understanding of the defect and dopant diffusion mechanism in SiGe is essential. The study of the defect and dopant diffusion in SiGe with

varying concentration of Ge will provide a comprehensible knowledge of the nature of defects and impurity states in SiGe.

1.3 Literature Survey: Relevant Studies in Diamond, Si and Ge

Ion implantation which offers precise control of implanted ion species, and implantation dose and profile is expected to play a major role in incorporating suitable dopant ions in diamond and SiGe. Hence, several techniques such as in-beam time differential perturbed angular distributions (TDPAD)[18], perturbed angular correlations (PAC)[19-21], emission channelling (EC)[22-24] and Mössbauer Spectroscopy[25-31] have been used to investigate implantation sites and implantation induced defects in diamond and Si and Ge. In diamond, electron emission channelling measurements have showed that ion implantation generally results in substantial fractions of implanted atoms at or close to substitutional sites with site fractions ranging from approximately 35% for ^{111}In to 70% for ^{33}P[32-37]. A combination of EC and PAC studies on In, Cd and Hf implanted diamonds[38] show that after annealing at 1600 K, considerable lattice damage was still present in the vicinity of the implanted probes, and practically none of the implanted probes were located in defect-free lattice sites. This study also demonstrated the crucial role played by hyperfine investigation methods (such as PAC) in elucidating details of the sites of implanted nuclear probes and their interactions with defects. Mössbauer Spectroscopy too is particularly useful in providing hyperfine interaction information such as the electric field gradients and *s*-electron density at the site of the probe nucleus in the lattice, and hence on the nature of the site, and is therefore the method of investigation followed in the present study. Relevant Mössbauer studies of ^{57}Co and ^{57}Fe implanted in diamond are reviewed below. This is followed by a literature survey of previous Mössbauer investigations after ^{57}Mn implantations in Si and Ge. No earlier Mössbauer studies of Fe in SiGe have been reported.

In an early study, Latshaw *et al.*[26] used the in-beam technique to excite and implant ^{57}Fe into diamond grains and observed a resonance spectrum characterized by a broad doublet. Sawicka *et al.*[25] performed temperature dependent measurements on ^{57}Co implanted into natural diamonds and resolved the spectrum for the as-implanted sample into a broad doublet and a weak single line. The large width (1.50 mm/s) of the doublet indicated an unresolved structure corresponding to the distribution of several quadrupole doublets. This is characteristic for Fe atoms resting in highly damaged or amorphous low-symmetry sites in implanted samples. The single line contribution for the as-implanted sample was only 3% of the total resonance effect, but increased to 20% upon annealing the sample to temperatures >600 K. The growth of the single line indicated a transition of Fe atoms from low-symmetry (LS) sites to high-symmetry (HS) sites which is associated with the healing of damaged bonds between carbon atoms and a recovery of the regular lattice in the neighbourhood of the Fe atoms. The large value of the isomer shift (δ = -0.95 mm/s) of the single line indicated an unusually large *s*-electron density. The internal pressure of the high-symmetry Fe sites in diamond was estimated on the basis of the isomer shift, to be ≈1500 kbar. This high pressure was attributed to the strong bonds between carbon atoms in diamond resulting in its extreme hardness.

Further Mössbauer measurements were carried out by Sawicki *et al.*[28] in their study of ^{57}Co implanted into natural diamond at 830 K. The spectra obtained by hot implantation were very similar to those obtained for the as-implanted sample at room temperature and then annealed at 950 K. A single line and an asymmetric doublet were fitted using least square analysis and Lorentzian lineshape approximations. The spectra were fitted assuming equal areas for the two lines of the doublet. The results showed no temperature dependence for the intensity of the single line as observed previously but the doublet showed a strong dependence below 100 K, resulting in an unusually high *f*-factor at low temperatures.

In a subsequent experiment, Sawicki *et al.*[28] performed a study of ^{57}Fe implanted into heated diamond crystals. The measurement was carried out in the temperature range 4 K to

300 K and showed that 20% of the implanted ions were found in the HS substitutional sites whilst the remaining 80% were in LS sites in diamond. The HS sites exhibited a high Debye temperature (θ_D = 1300 K) and a high *s*-electron density characteristic of Fe^{4+} ($3d^4sp^3$) electron configuration, whereas the low symmetry sites were characterized by a Debye temperature of 550 K and a very large electric field gradient V_{zz} = 1.2 x 10^{18} V/cm^2. The abnormal increase of the recoil-free factor for LS sites below 100 K was evidence of localized jumps of impurity atoms between adjacent tetrahedral and hexagonal positions in the host lattice.

A systematic study of the amorphization of the diamond lattice produced by ion implantation was conducted by de Potter *et al.*[29]. Mössbauer measurements were performed on ^{57}Co implanted into Type Ia natural diamonds as a function of implantation dose and annealing temperature. The spectra were resolved into two single lines and two doublets but the components varied in linewidth and symmetry with implantation dose. At implantation doses of $\leq 10^{14}$ atoms/cm^2, the spectra were attributed to ^{57}Fe in highly damaged surroundings. A strongly damaged layer was observed which transformed into amorphous carbon between 10^{14}–10^{15} atoms/cm^2. Implantation at a dose of 10^{15} atoms/cm^2 resulted in the formation of a completely amorphous layer. No change was observed when the implantation was increased to 10^{16} atoms/cm^2. The spectrum at 10^{17} atoms/cm^2 was again different and consisted of a fairly symmetric doublet with a small splitting of 1 mm/s, in agreement with that observed for graphite. A similar result was observed by Sawicki *et al.*[30] for higher implantation doses of ^{57}Fe in diamond.

In a recent study, in-beam Mössbauer Spectroscopy (IBMS) measurements were performed by Bharuth-Ram *et al.*[31] in which a heavy ion beam was used to Coulomb excite and recoil implant the ^{57}Fe into HTHP produced Type Ib diamond crystals at an extremely low implantation dose of 10^{11} atoms/cm^2. The spectra, which were collected at sample temperatures of 300 to 800 K, were characterized by two symmetric doublets and a weak single line and changed very little with temperature. The isomer shift of the single line was

determined as 0.16(4) mm/s, and was attributed to interstitial Fe. The quadrupole splittings of the doublet, ΔE_Q = 2.10(5) mm/s and 2.33(5) mm/s remained fairly constant in the temperature range, corresponds to electric field gradients of 0.9×10^{18} V/cm^2 and and 1.07×10^{18} V/cm^2, respectively. These were in general agreement with those observed by Sawicki *et al.*[28] and supported their conclusion that electric field gradients at Fe nuclei in diamond originate from non-cubic distribution of nearest carbon neighbours.

In Si and Ge, the larger lattice constants allow dopant incorporation by thermal diffusion. Hence recent Mössbauer studies for these materials have focussed on understanding the charge state dependence and diffusivity of interstitial Fe. In silicon, the results obtained either compare well with, or contradict each other due to different experimental approaches and sample preparation[39-43]. For example, the results obtained by Heiser and Mesli[40] show that positively charged Fe_i^+ diffuse faster than that of neutral Fe_i^0 whereas Koveshnikov and Rozgonyi[35] found the opposite behaviour.

In order to detect diffusional jumps of interstitial Fe in silicon, Gunnlaugsson *et al.*[44], employed ^{57}Fe Mössbauer Spectroscopy after implantation of ^{57}Mn into P-doped and B-doped silicon single crystals held at 400-813 K. Their results show that radiation damage was annealed within the ^{57}Mn lifetime ($t_{1/2}$= 1.5 minutes) and that recoil energy of 40 eV imparted on the Fe atoms resulted in the relocation of the majority of the Fe atoms into interstitial sites. At temperatures ≤475 K, the spectra were dominated by previously assigned substitutional Fe[45] (δ = 0.04 mm/s) and interstitial Fe in the tetrahedral site[45-46] (δ = 0.776 mm/s), no line broadening was evident. As the temperature was increased, the interstitial line showed clear line broadening and a new line (δ = 0.51 mm/s) assigned to Fe_i – vacancy pairs became evident. The new line was found to depend on material type. Similar line broadening was previously observed by Schwalbach *et al.*[46] in their experiment involving recoil implantation of Coulomb-excited ^{57m}Fe in silicon. This line broadening was attributed to diffusional jumps of interstitial Fe during the lifetime of the

Mössbauer state ($t_{1/2}$= 100 ns). At highest temperatures, the interstitial line practically disappeared and the spectra were dominated by a substitutional line and the new line attributed to Fe_i-V pairs. A plot of line broadening against temperature revealed that the line broadening in the p^{++} - material was greater than for the n^+-type material which implies that the diffusivity of Fe_i^+ is larger than that of neutral Fe_i^0. Further, from the data analysis performed by Gunnlaugsson *et al.*, the extracted activation energy values compared well with those obtained by Heiser[40] and Koveshnikov[41] and varied at most by 0.11 eV as observed in the resulting Arrhenius plots.

In a subsequent measurement, Gunnlaugsson *et al.*[47] investigated the radiation damage in ion-implanted silicon-based materials held at 77-500 K. In the n-type Si sample, at the lowest temperature, three spectral components were observed corresponding to substitutional Fe (Fe_S), interstitial Fe (Fe_i) and an asymmetric quadrupole-doublet (Fe_D) attributed to the damage caused by ion implantation. At 77 K, the substitutional Fe fraction was small, less than 5% whilst 30-40% was determined to be in tetrahedral interstitial sites and the balance were found in damage sites. A similar pattern was observed for SiSn single crystals. During the annealing series for the temperature range of 77 and 150 K, the Fe_D component decreased by 19% whilst the Fe_i increased by 13%. The Fe_D, component showed considerable annealing at 300 K and the population of the substitutional site increased by 6%. Total annealing of the damage site occurs in the temperature range 300-450 K and the area fraction (20-30%) of the Fe_S component remained fairly constant at the higher implantation temperatures.

In a comparative Mössbauer study of ^{57}Mn implanted in Ge single crystals held at temperatures 77-800 K, Gunnlaugsson *et al.*[48] found that at low temperatures, the spectra were dominated by a broad asymmetric doublet which was assigned to Fe in implantation damage related sites similar to that observed in silicon. These defects showed considerable annealing at approximately 350 K, with the appearance of a strong single line assigned to substitutional Fe and a quadrupole split component which was attributed Fe_i-V pairs. The

majority of the Fe atoms, due to the recoil in the $^{57}Mn \rightarrow {}^{57}Fe$ β - decay, were expelled into tetrahedral interstitial sites. The isomer shift of this component was determined to be 0.8 mm/s. This component shows appreciable line broadening above 700 K, reflecting diffusion of the implanted probe nuclei. The major difference between the Si and Ge results is the lower spectral intensity of the interstitial line in Ge and the strong increase in the fraction attributed to Fe_i-V complexes. This allowed for a more accurate determination of the temperature behaviour of the Fe_i-V complexes which was questionable in Si. The Debye temperatures for the damage and the substitutional sites were determined to be in the range 350-450 K whilst the Debye temperature for the interstitial site and the Fe_i-V complexes was found to be in the region of 150-250 K.

1.4 Objectives of Research Study

The exceptional and extreme properties of diamond, such as its wide band gap (5.48 eV), high thermal conductivity, high mobility for both *p* and *n*-type carriers, make it an ideal base for the fabrication of semiconducting and opto-electronic devices. This can be achieved by the incorporation of foreign atoms within the lattice either by diffusion or by ion implantation. In Si and Ge, incorporation of dopants maybe accomplished by thermal diffusion but specific applications required tailored structures that can only be achieved by ion implantation. In diamond doping by diffusion is difficult to attain due to the lattice rigidity, the small covalent radius of carbon and the high formation energy of most potential dopants resulting in the extremely low solubility of dopant atoms. Therefore, ion implantation is a favoured alternative as it offers precise control of depth profile and concentration, and practically any ion can be accelerated and implanted. A major disadvantage of this technique is that lattice damage is induced by the implantation process and this result in the creation of a large variety of defects. The healing of radiation damage is necessary and is achieved by thermal treatment of implanted samples to reduce the concentration of such defects. Hyperfine interactions such as Perturbed Angular Correlation

(PAC) and Mössbauer Spectroscopy (MS) offer very sensitive means to examine the immediate neighbourhood of implanted atoms and study the annealing of defects following heat treatment.

Mössbauer spectroscopy has been adopted as the investigative tool used in the investigations presented in this thesis. ^{57}Co source based MS has many advantages. As an off-line measurement it is free from restrictions imposed by limited beam-time on on-line measurements. Implantation and annealing temperatures can be independently varied, and all measurements can be done at the same temperature, thus avoiding second order Doppler shifts of the isomer shifts of the spectral components. However in the case of crystalline samples, the implantation dose of the ^{57}Fe Mössbauer nuclei must be kept below the amorphization threshold of the sample. This makes measurement times prohibitively long. For example, a diamond sample implanted with 5 x 10^{14} cm^{-2} ^{57}Fe ions and a 30 mCi ^{57}Co source requires a measurement time, T_M, ≥ 14 days for a CEMS spectrum with acceptable statistics. MS studies following ^{57}Mn* implantation, the sample under study acts as a source and hence implantation doses of $\leq 10^{11}$ cm^{-2} are required to achieve good spectra, making $T_M \leq 10$ mins. The ^{57}Mn* half-life (1.5 min) is also sufficient to allow thermal treatment to take effect before decay to the 100 ns Mössbauer level in ^{57}Fe. This method hence allows a full temperature-dependent study to be done on a sample in ≤ 120 mins. Five shifts of beam-time (40 hours) at ISOLDE per year yield over 300 Mössbauer spectra. High amongst novel techniques is MS using synchrotron radiation, a discussion of which, however, is beyond the scope of the present study.

The present study therefore had the following aims:

(i) to investigate the lattice sites of Fe in ion implanted natural and synthetic diamonds and the annealing characteristics of implantation-induced lattice damage, and

(ii) to identify substitutionally and interstitially incorporated Fe in $Si_{1-x}Ge_x$, and study their diffusion characteristics as function of temperature.

The following measurements were performed:

(a) Source based Conversion Electron Mössbauer Spectroscopy on High-Temperature High-Pressure (HTHP) and Chemical Vapour Deposition (CVD) synthesised diamonds which were implanted with 5 x 10^{14} ^{57}Fe ions/cm^2.

(b) ^{57}Fe Mössbauer Spectroscopy investigations on diamond (Type IIa and Chemical Vapour Deposition) following implantation of ^{57}Mn*, and

(c) ^{57}Fe Mössbauer Spectroscopy investigations on $Si_{1-x}Ge_x$ single crystals following implantation of ^{57}Mn*.

The principles of the Mössbauer Effect are presented in Chapter 2 where the hyperfine interaction parameters that allow the effect to be used as a sensitive tool are also discussed. Experimental details of the source-based measurements and measurements following ^{57}Mn* implantation at the on-line isotope separator facility, ISOLDE, at CERN, Geneva, are presented in Chapter3, the results are presented and discussed in Chapter 4, and conclusions drawn from the investigations are presented in Chapter 5.

Chapter 2

THEORY

2.1 The Mössbauer Effect

The phenomenon of the emission or resonant absorption of gamma-ray photons without loss of energy due to recoil and without thermal broadening is known as the Mössbauer Effect. This effect was discovered in 1957 by Rudolph Mössbauer while studying the resonance absorption of γ-rays metallic ^{191}Ir (129 keV state)[55]. A brief review of the Mössbauer Effect is outlined below, this is followed by a discussion of the relevant hyperfine parameters, which allow the effect to be applied as a diagnostic tool.

2.1.1 Natural Line Width

Consider the emission of γ-ray photons from a nucleus, which undergoes a transition from an excited state to the ground state. The emitted gamma-rays have a very small spread of energies. The uncertainty in energy corresponds to the width Γ of the nuclear state and can be obtained from the energy-time uncertainty relation:

$$\Delta E.\Delta t \geq \hbar \qquad (2.1)$$

where $\hbar = h/2\pi$, h is the Planck's constant and Δt is the time interval to measure the energy E which is in the order of the meanlife τ of the state under consideration.

Weiskopf and Wigner[56] showed that by setting $\Delta t \cong \tau$, the approximate width $\Gamma = \Delta E$ of a level is given by $\Gamma = \hbar/\tau$ where Γ represents the full width of the transition spectral line at half maximum. Further, Weiskopf and Wigner found that the spectral line has a Lorentzian or Breit-Wigner shape described by:

$$I(E) = (\text{constant})\frac{\Gamma/2\pi}{(E - E_o)^2 + (\Gamma/2)^2} \tag{2.2}$$

where *I(E)* is the transition energy intensity, E the transition energy and E_o represents the most probable transition energy. Γ is called the natural linewidth of the spectral line.

The width of the transition line is governed by the mean lifetime τ of the excited state. In Mössbauer spectroscopy, the lifetime of excited states range from $\approx 10^{-6}$ to 10^{-11} s, and for ^{57}Fe, the mean lifetime for the first excited Mössbauer state is $\tau = 1.43 \times 10^{-7}$ s. The resulting value for the linewidth Γ is 4.55×10^{-9} eV.

2.1.2 Nuclear Resonance Flourescence

Consider a nucleus in an excited state of energy E_e which undergoes a transition to the ground state of energy E_g. A quantum of energy $E_o = E_e - E_g$ in the form of a γ-ray is emitted which can be absorbed by another nucleus of the same kind if both processes are recoilless. Since the absorption in general can occur only for a nucleus in the ground state, only a γ-ray emitted in a transition to the ground state is useful for practical application of the Mössbauer Effect. The principle of the Mössbauer Effect is illustrated in Figure 2.1.

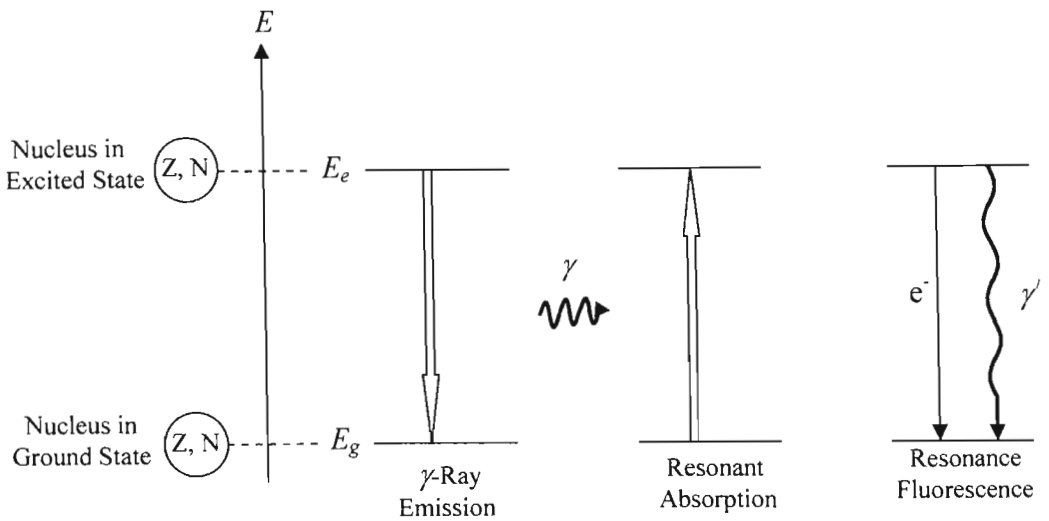

Figure 2.1: Recoilless emission and absorption of a γ- ray.

If a spectral line for the emission and absorption processes coincide at the same energy position E_o, then the maximum resonance absorption occurs. The resonance absorption cross-section is given by the Breit-Wigner formula:

$$\sigma = \frac{\sigma_o \Gamma^2}{[\Gamma^2 + 4(E - E_o)^2]} \tag{2.3}$$

where σ_o is the maximum cross-section and is given by:

$$\sigma_o = \frac{\lambda^2}{2\pi} \cdot \frac{2I_e + 1}{2I_g + 1} \cdot \frac{1}{\alpha + 1} \tag{2.4}$$

where I_e and I_g are the nuclear spin quantum numbers for the excited and ground states, respectively. λ is the wavelength of the γ-ray and α the internal conversion co-efficient (For ^{57}Fe, $\alpha = 8.21$).

The nucleus remains in the excited state of energy E_o for the mean lifetime after the absorption process and then undergoes a transition back to the ground state by emission of either a γ-ray or conversion electrons due to internal conversion (the transfer of the photon energy to an electron in the innermost electron shells of the atom). This process is referred to as nuclear resonance fluorescence.

2.1.3 Recoil Energy Loss

Consider a γ-ray (photon) emitted from an excited nucleus of mass M (initially at rest), shown in Figure 2.2 below.

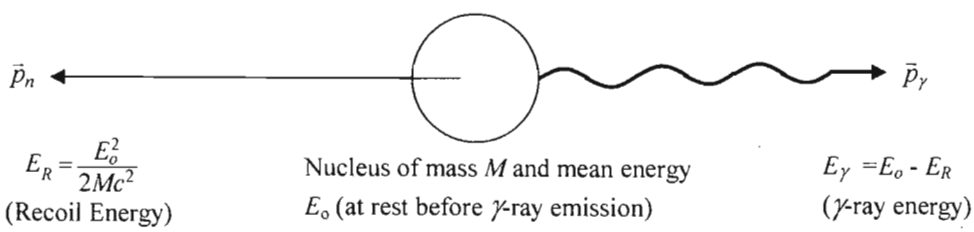

Figure 2.2: Ilustration of the recoil effect experienced by a nucleus of mass *M*.

This process gives rise to a recoil imparted to the emitting nucleus. As a result the nucleus moves in the opposite direction to the γ-ray emission with a velocity, say $\vec{v}$. The kinetic recoil energy is given by $E = \frac{1}{2}Mv^2$.

Applying the conservation of momentum to the above process gives:

$$p_n = -p_\gamma = -\frac{E_\gamma}{c} \tag{2.5}$$

where p_n and p_γ are the linear momenta of the nucleus and the γ-ray, respectively and $E_\gamma = E_o - E_R$. Taking into consideration the large mass of the nucleus and using non-relativistic approximations gives:

$$E_R = \frac{p_n^2}{2M} = \frac{E_\gamma^2}{2Mc^2}. \tag{2.6}$$

For $E_R << E_o$, we can set $E_\gamma \approx E_o$ in equation (2.6) which reduces to:

$$E_R = \frac{E_o^2}{2Mc^2}. \tag{2.7}$$

Evaluating equation (2.7) into numerical form results in:

$$E_R(\text{eV}) = 5.37\times10^{-4}\,\frac{E_o^2(\text{keV})}{A} \tag{2.8}$$

where A is the mass number of the decaying nucleus.

For ^{57}Fe, the Mössbauer transition between the first excited state and the ground state ($E_o = E_e - E_g = 14.4$ keV) results in $E_R = 1.95\times10^{-3}$ eV.

2.1.4 Thermal Broadening

During the decay process, the recoil effect causes a displacement from E_o by an amount E_R shown in Figure 2.3.

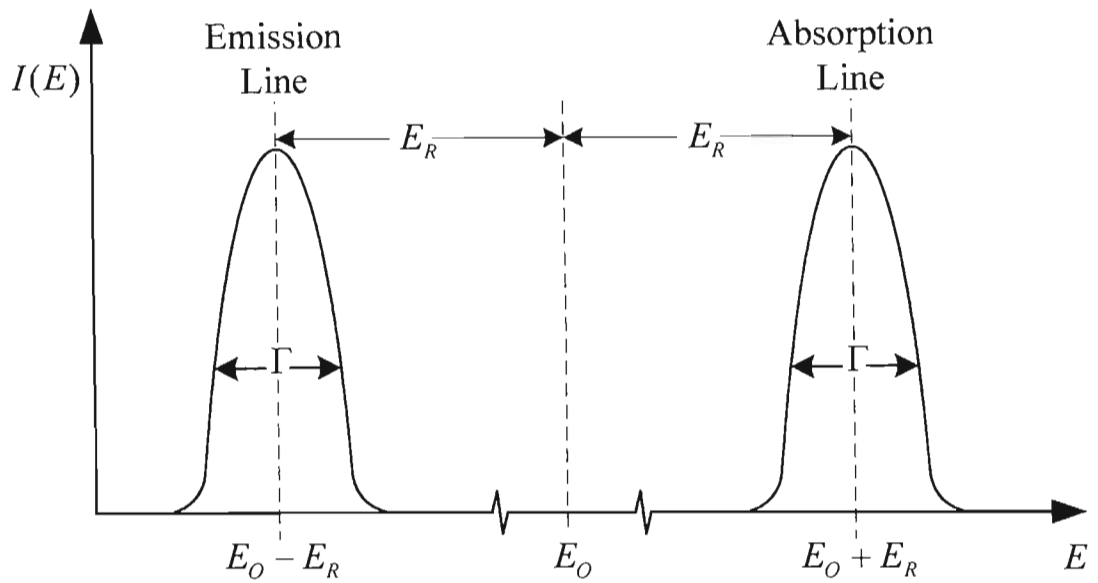

Figure 2.3: Schematic diagram of the recoil effect showing the transition lines for emission and absorption.

In the absorption process, for the γ-ray to be absorbed by a nucleus requires a total energy of $E_\gamma = E_o + E_R$ to make up for the transition from the ground state to the excited state and the recoil effect. The transition lines for absorption and emission are separated by a distance of $2E_R$, which is 10^6 times larger than the natural line width ($\Gamma = 4.55 \times 10^{-9}$ eV), as a result, the γ-ray emission line does not overlap the absorption line, and nuclear resonance absorption is not observable.

In a gas, atoms are not at rest and move with large velocities. If γ-ray emission occurs while the nucleus (or atom) is moving at a velocity of v_n in the direction of γ-ray propagation then the γ-rays of energy E_γ receives a Doppler energy E_D given by:

$$E_D = \frac{v_n}{c} E_\gamma, \tag{2.9}$$

which is added to E_γ:

$$E_\gamma = E_o - E_R + E_D . \tag{2.10}$$

The mean Doppler broadening can be determined from:

$$\bar{E}_D = E_\gamma \left(\frac{2E_K}{Mc^2} \right)^{1/2} . \tag{2.11}$$

where E_K is the mean kinetic energy of the moving nucleus (or atom) given by:

$$E_K = \tfrac{1}{2} M v_n^2 = \tfrac{3}{2} k_B T . \tag{2.12}$$

For ^{57}Fe, E_o = 14.4 keV, $E_R = 1.95 \times 10^{-3}$ eV and $E_D \cong 10^{-2}$ eV at 300 K.

Consider an an Einstein solid with $3N$ vibrational modes (N is the number of atoms in the solid) each having the same frequency ω. The solid is characterized by the quantum numbers of its oscillators and any changes in its state is a result of an increase or decrease in one or more of the quantum numbers. This corresponds to the absorption or emission of quanta of energy $\hbar\omega$ which in solids is of the order of 10^{-2} eV. The emission of γ-ray is accompanied by the transfer of integral multiples of this photon energy ($0\hbar\omega$, $\pm\hbar\omega$, $\pm 2\hbar\omega$, ...) to the lattice. Therefore, the fraction of events, f, which takes place without lattice excitation, provided $E_R << \hbar\omega_E$ is given by:

$$E_R = (1 - f)\hbar\omega_E \tag{2.13}$$

and

$$f \cong \frac{1 - E_R}{\hbar\omega_E} = 1 - k^2 < x^2 > \tag{2.14}$$

where $< x^2 >$ is the expectation value of the squared vibrational amplitude in the x-direction and k is the propagation vector. The above equation can be written in the following general form:

$$f = \exp\left(-\frac{E_R}{\hbar\omega_E}\right) = \exp\left(-k^2 < x^2 >\right). \tag{2.15}$$

From the Debye model[57] for solids, the recoil-free fraction can be written as:

$$f = \exp\left[-\frac{6E_R}{k_B\theta_D}\left\{\frac{1}{4}+\left(\frac{T}{\theta_D}\right)^2 \int_0^{\theta_T/T} \frac{x}{e^x - 1}dx\right\}\right]. \tag{2.16}$$

For $T << \theta_D$, the above equation reduces to:

$$f = \exp\left(\frac{-6E_R T}{k_B\theta_D^2}\right) \tag{2.17}$$

where $\theta_D = \hbar\omega/k_B$ is the Debye temperature. The recoil-free fraction, f is also referred to as the Debye-Waller factor or Lamb-Mössbauer factor.

- f increases with decreasing recoil energy loss, E_R i.e. decreasing transition energy, E_γ.
- f increases with decreasing temperature, T.
- f increases with increasing Debye temperature, θ_D. θ_D maybe considered as a measure of the strength of the bonds between the Mössbauer atom and the lattice.

The f-value for the 14.4 keV γ- transition in ^{57}Fe at 0 K can be determined from the above equations to be 0.91.

2.2 Factors determining the Mössbauer Effect

In a typical Mössbauer experiment, the source and the absorber are moved relative to each other in a controlled manner and the transmitted γ - quanta are recorded as a function of the Doppler velocity. A Mössbauer spectrum is a plot of the relative transmission versus Doppler velocity and is characterised by the number, shape, position and relative intensity of the absorption line. These features result from the nature of various nuclear hyperfine interactions which is a perturbation of nuclear energy levels due to the interaction of nuclear moments with the electric and magnetic fields surrounding the nucleus. In Mössbauer Spectroscopy three kinds of interactions are considered:

(a) electric monopole interaction (E0),
(b) electric quadrupole interaction (E2), and
(c) magnetic dipole interaction (M1).

The E0 interaction affects the position of the resonance lines and gives rise to the chemical shift or isomer shift, δ. The E2 and M1, interactions are due to the splitting of degenerate nuclear energy levels into sublevels with the resulting Mössbauer parameters corresponding to the electric quadrupole splitting ΔE_Q and the magnetic splitting ΔE_M, respectively. These parameters together with δ are important for obtaining chemical information in Mössbauer Spectroscopy.

2.2.1 Electric Hyperfine Interactions

The total energy of the electrostatic interaction between a nucleus with a charge Ze and surrounding charges can be written in the following form[58]:

$$E_{el} = \int \rho_n(r) V(r) d\tau \qquad (2.18)$$

where $\rho_n(r)$ represents the nuclear charge density at a point $r = (x_1, x_2, x_3)$. The Coulomb potential at point r is denoted by $V(r)$ and $d\tau = dx_1 \bullet dx_2 \bullet dx_3$ is the volume element.

Now apply Taylor series for $V(r)$ at $r = 0$ and inserting into equation (2.18) gives:

$$E_{el} = V_o \int \rho_n(r) d\tau + \sum_{i=1}^{3} \left(\frac{\partial V}{\partial x_i} \right)_o \cdot \int \rho_n(r) x_i d\tau + \frac{1}{2} \sum_{i,j}^{3} \left(\frac{\partial^2 V}{\partial x_i \partial x_j} \right)_o \cdot \int \rho_n(r) x_i x_j d\tau + \ldots \qquad (2.19)$$

The first term reduces to eZV_o because the nuclear charge $eZ = \int \rho_n d\tau$ represents the electrostatic interaction between the nucleus and other surrounding charges, which contributes to the potential energy of the crystal as a whole and can be ignored. The second term which represents the electric dipole interaction and higher order terms do not exist because of symmetry arguments. The third term $\left(\partial^2 V / \partial x_i \partial x_j\right)_o = V_{ij}$ forms a 3×3 second-rank tensor and is significant in providing useful information in determining Mössbauer parameters.

By applying an appropriate co-ordinate system, the tensor elements $V_{ij} = 0$ and only the diagonal elements remain. The third term in equation (2.19) therefore reduces to:

$$E = \frac{1}{2} \sum_{i=1}^{3} V_{ii} \cdot \int \rho_n(r) x_i^2 d\tau = \frac{1}{2} \sum_{i=1}^{3} V_{ii} \cdot \int \left(x_i^2 - \frac{r^2}{3} \right) d\tau + \frac{1}{6} \sum_{i=1}^{3} V_{ii} \cdot \int \rho_n(r) r^2 d\tau \qquad (2.20)$$

where $r^2 = \sum_{i=1}^{3} x_i^2$.

By applying Laplace's equation at $r = 0$ gives:

$$(\Delta V)_o = \left(\sum_{i=1}^{3} V_{ii}\right)_o = 4\pi e|\psi(0)|^2 \qquad (2.21)$$

where $\rho_n = -e|\psi(0)|^2$ is the charge density at the nucleus due to the surrounding electrons. Substituting equation (2.21) in (2.20) gives:

$$E = \frac{2}{3}\pi e|\psi(0)|^2 \int \rho_n(r) r^2 d\tau + \frac{1}{2}\sum_{i=1}^{3} V_{ii} \cdot \int \rho_n(r)\left(x_i^2 - \frac{r^2}{3}\right) d\tau = E_I + E_Q \qquad (2.22)$$

where $E_I \equiv$ electric monopole interaction and $E_Q \equiv$ electric quadrupole interaction.

2.2.2 Electric Monopole Interaction: Isomer Shift

This interaction represents the electrostatic interaction between the nuclear charge and the electrons inside the nuclear region. The probability of *s*-electrons penetrating the nucleus is greater than the $p_{½}$ electrons but electrons with non-zero angular momentum (*p-, d-, f-)* do not have the ability of entering the nucleus.

Now consider the first term of equation (2.22) and substitute $\int \rho_n(r) r^2 d\tau = < r^2 > .Ze$ where $\int \rho_n(r) d\tau$ is the nuclear charge *Ze* gives:

$$E_I = \frac{2}{3}\ \pi\ Ze^2\ |\psi(0)|^2 < r^2 > \equiv \delta E \cong 10^{-8}\text{eV} \qquad (2.23)$$

which represents a very small change in energy called the interaction energy. This is the amount of energy that a nuclear level of a nuclear state is shifted due to the Coulomb

interaction. The nuclear volume and $< r^2 >$ differs from nuclear state to nuclear state hence δE will also differ and this illustrated in the Figure 2.4.

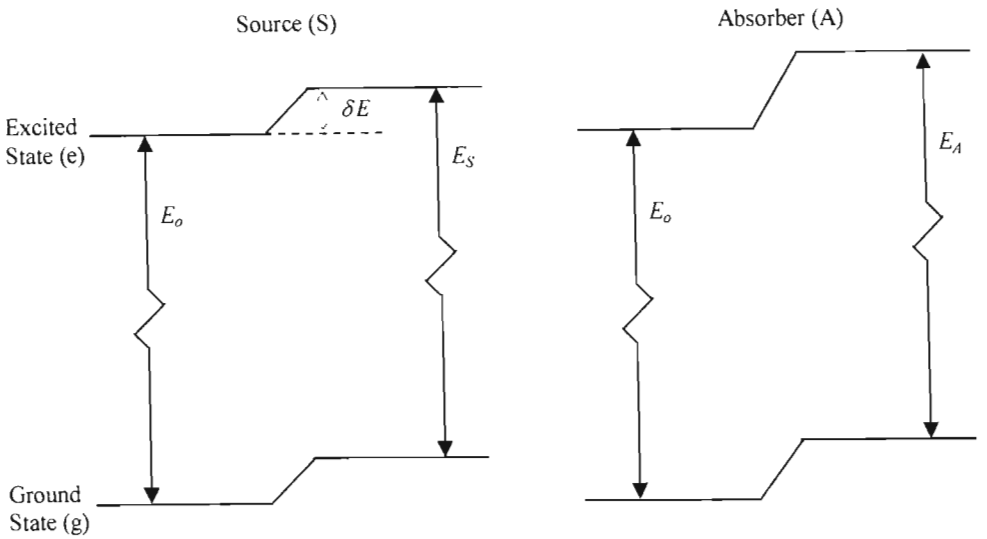

(a)

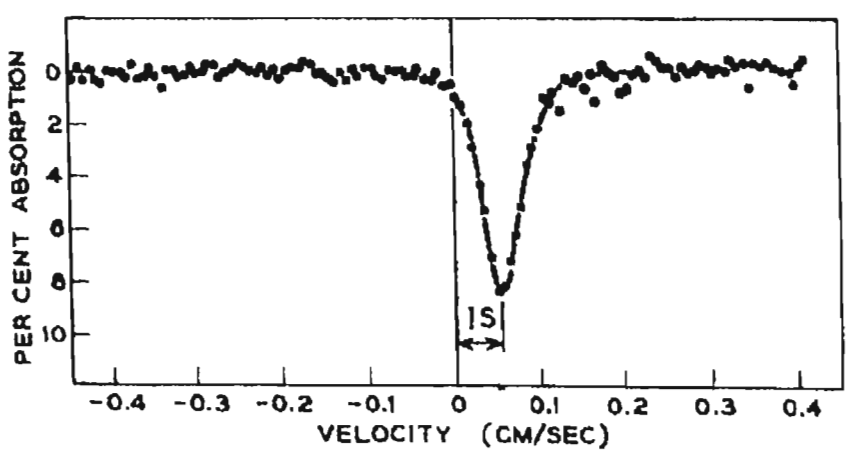

(b)

Figure 2.4 : (a) Electric monopole interaction between the nuclear charge and electrons depicting the isomer shift.

(b) A typical Mössbauer spectrum of Ferricinium Bromide showing the effect of the electric monopole interaction[59].

For a nuclear transition between the ground state (g) and an excited state (e), the energy change of a γ-ray is given by:

$$\Delta E = E_S - E_O = \delta(E)_e - \delta(E)_g = \frac{2}{3}\pi Ze^2 |\psi(0)|^2 \left[< r^2 >_e - < r^2 >_g \right]. \qquad (2.24)$$

The corresponding electrostatic shift between the absorber (A) and the source (S) is given by $\delta = (\Delta E)_A - (\Delta E)_S$ where δ is the isomer shift and is given by:

$$\delta = \frac{4}{5}\pi Ze^2 \left\{ |\psi(0)|_A^2 - |\psi(0)|_S^2 \right\} \left(\frac{\delta R}{R} \right) R^2 \qquad (2.25)$$

where R is the radius of a spherical nucleus and $\delta R = R_e - R_g$.

The total electron density is sensitive to changes taking place in the outer valence shells and increases or decreases when $\frac{\delta R}{R}$ is positive or negative, respectively. When $\frac{\delta R}{R}$ is positive (as for ^{119}Sn), an increase in the s-electron density results in a positive isomer shift. For ^{57}Fe, $\frac{\delta R}{R}$ is negative, implying an increase in the s-electron density at the absorber resulting in a more negative isomer shift.

The corresponding Doppler velocity v_D in a Mössbauer experiment is:

$$v_D = \left(\frac{4\pi c}{5E_\gamma} \right) Ze^2 R^2 \frac{\delta R}{R} \left[|\psi(0)|_A^2 - |\psi(0)_S^2| \right] \qquad (2.26)$$

and can be determined from the Mössbauer spectrum by measuring the distance of the resonance line from the zero Doppler velocity.

The observed line shift of the energy levels is not entirely due to the isomer shift but can also arise from the thermal motion of the Mössbauer atoms and this effect is appreciable but considerably smaller than the isomer shift. This temperature dependent contribution is called the second-order Doppler shift (SOD).

2.2.3 Electric Quadrupole Interaction: Quadrupole Splitting

In the previous sections, the nuclear charge distribution has been considered as uniform and spherical therefore the nuclear quadrupole moment and the second term in equation (2.22) becomes zero. In general, the charge distribution in a number of nuclei is not spherical and this deviation from the normal spherical symmetry can be measured by the electric quadrupole moment eQ.

If we choose the charge symmetry as cylindrical then the electric quadrupole moment can be written as:

$$Q \equiv \int \rho_n(r) r^2 (3\cos\theta - 1) d\tau \,. \tag{2.27}$$

Nuclear states with spin quantum number $I = 0, ½$ have zero quadrupole moment whereas nuclear states with $I > ½$ have non-zero quadrupole moment and thus interacts with an electric field described by the electric field gradient (EFG). Molecular and electronic structure information of a Mössbauer atom can thus be determined from the electric field gradient.

2.2.3.1 Electric Field Gradient

Consider a point charge placed at a distance $r = (x^2 + y^2 + z^2)^{1/2}$ from a nucleus (located at the origin of the coordinate system) which produces a potential $V(r) = q/r$ at the nucleus. The electric field $\vec{E}$ can be determined from the gradient of the potential given by $-\vec{\nabla}V$ and the electric field gradient from:

$$EFG = \vec{\nabla}\vec{E} = -\vec{\nabla}\vec{\nabla}V = \begin{pmatrix} V_{xx} & V_{xy} & V_{xz} \\ V_{yx} & V_{yy} & V_{yz} \\ V_{zx} & V_{zy} & V_{zz} \end{pmatrix} \tag{2.28}$$

where $V_{ij} = \dfrac{\partial^2 V}{\partial i \partial j} = q(3ij - r^2\delta_{ij})r^{-5}$, $(i, j = x, y, z)$ are the nine components of the 3×3 second rank EFG tensor. It is convenient to choose the principal axes such that $|V_{zz}| \geq |V_{xx}| \geq |V_{yy}|$ and specify the EFG by two independent parameters V_{zz} and the asymmetry parameter η which is defined as:

$$\eta = \frac{V_{xx} - V_{yy}}{V_{zz}} \tag{2.29}$$

and hence must satisfy $0 \leq \eta \leq 1$.

2.2.3.2 Quadrupole Splitting

The interaction between the electric quadrupole moment of the nucleus, Q and the EFG maybe expressed by the following Hamiltonian[60]:

$$\hat{H}_Q = \frac{eQV_{ZZ}}{4I(2I-1)}\left[\, 3\hat{I}_Z^2 - \hat{I}^2 + \eta\,(\hat{I}_+^2 + \hat{I}_-^2)/2\right] \tag{2.30}$$

where I is the nuclear spin quantum number, $\hat{I}$ is the nuclear spin operator, and $\hat{I}_\pm$ are the shift operators.

From the first order perturbation matrix, the eigenvalues E_Q corresponding to $\hat{H}_Q$ is given by:

$$E_Q = \frac{eQV_{ZZ}}{4I(2I-1)}\left[\, 3m_I^2 - I(I+1)\right]\,(1+\eta^2/3)^{1/2} \tag{2.31}$$

where $m_I = I,\ I\text{-}1,\ \ldots,\ -I$ is the nuclear magnetic spin quantum number.

Now consider the effect of the electric quadrupole interaction in ^{57}Fe with $I = 3/2$ (14.4 keV excited state) and $I = 1/2$ (ground state) shown below in Figure 2.5. The ground state is not split whereas the excited state splits into two substates $|3/2, \pm 3/2\rangle$ and $|3/2, \pm 1/2\rangle$. For an axially symmetric EFG (η=0), the perturbation energies can be determined from equation (2.31) for the substates as follow:

$$\begin{aligned} E_Q(\pm 3/2) &= 3eQV_{ZZ}/12 \ \text{ for } I = 3/2,\ m_I = \pm 3/2 \\ E_Q(\pm 1/2) &= -3eQV_{ZZ}/12 \ \text{ for } I = 3/2,\ m_I = \pm 1/2 \end{aligned} \tag{2.32}$$

The energy difference between the two substates is given by:

$$\Delta E_Q = eQV_{zz}/2 \tag{2.33}$$

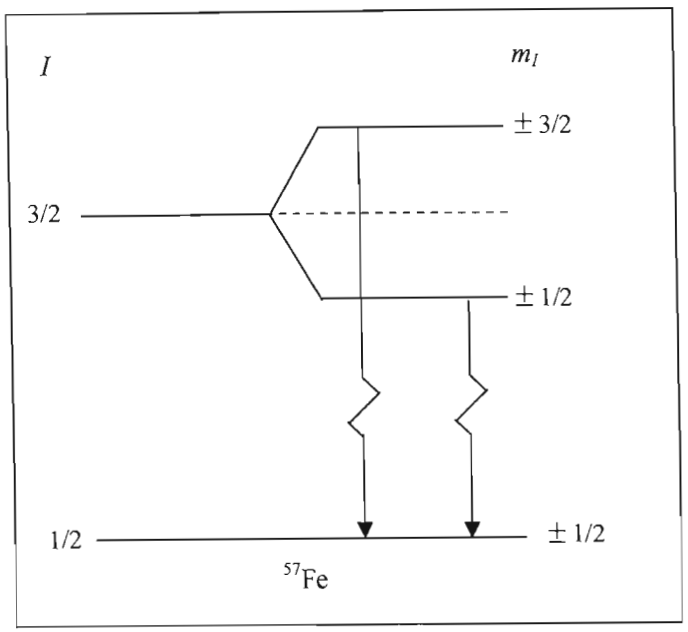

(a)

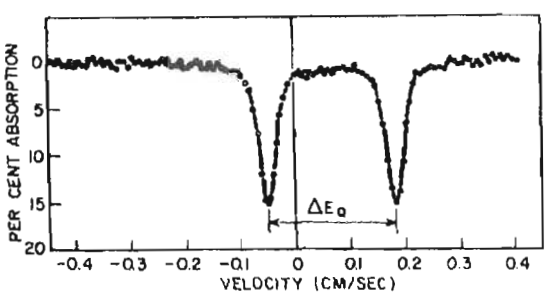

(b)

Figure 2.5: (a) Diagram illustrating the quadrupole splitting in ^{57}Fe.
(b) Schematic diagram of the resultant Mössbauer spectrum of Biferrocenyl[59].

The distance between two resonance lines corresponds to the energy difference ΔE_Q called the quadrupole splitting which is an important Mössbauer parameter for the determining of molecular, bond and electronic properties of the Mössbauer atom.

2.2.4 Magnetic Hyperfine Interaction

Consider a nucleus in an energy state E with spin quantum number ($I > 0$) and magnetic dipole moment ($\vec{\mu} \neq 0$) which interacts with a magnetic field $\vec{H}$ at the nucleus. The resulting interaction is called the magnetic dipole interaction or nuclear Zeeman effect and can be described by the Hamiltonian[61] below:

$$\hat{H}_m = -\hat{\vec{\mu}}.\hat{\vec{H}} = -g_N \beta_N \hat{\vec{I}}.\hat{\vec{H}} \tag{2.34}$$

where g_N is the nuclear Lande' factor and $\beta_N = e\hbar/2Mc$ (M = nuclear mass) is the nuclear magneton.

The eigenvalues E_M to $\hat{H}_M$ can be determined by diagonalising the first–order perturbation matrix and is given by:

$$E_M(m_I) = -\mu H m_I / I = -g_N \beta_N H m_I \tag{2.35}.$$

The Zeeman effect splits the nuclear state (spin I) into $2I+1$ equally spaced substates as shown in Figure 2.6.

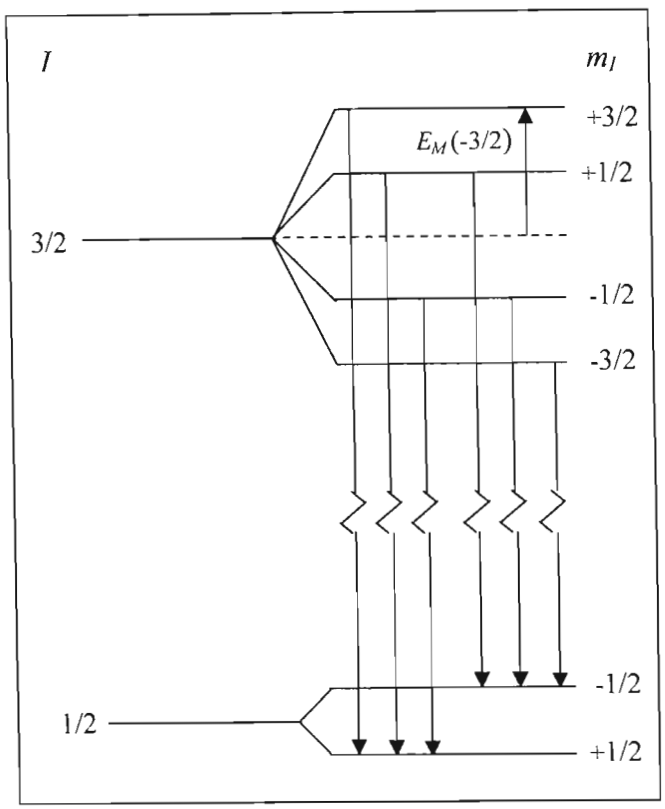

(a)

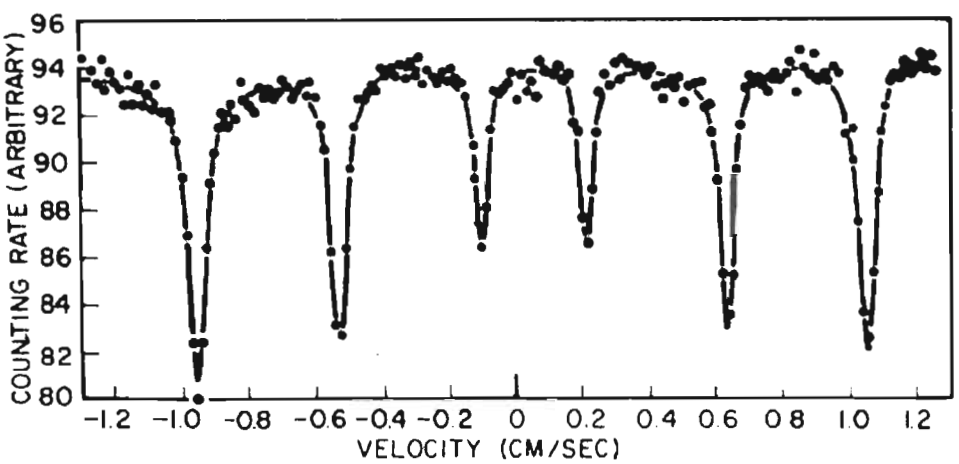

(b)

Figure 2.6: **(a)** **The nuclear Zeeman effect in ^{57}Fe.**

(b) **A typical Mössbauer spectrum of FeF_3 at 4 K showing magnetic hyperfine splitting[59].**

The magnetic dipole interaction in ^{57}Fe where $I = 3/2$ level is split into four substates and the ground state with $I = 1/2$ splits into two substates. The number of allowed states is determined by considering selection rules for quantum numbers. Next, we revisit these rules and apply to the situation above.

Consider an electromagnetic transition between two nuclear levels with initial and final nuclear spins I_i and I_f, respectively and further between substates with initial and final m_z values of m_i and m_f, respectively. Taking into account the law of conservation of angular momentum and the law of conservation of parity, where the quantum number I obeys the following conditions:

$$\left|I_i - I_f\right| \leq L \leq \left|I_i + I_f\right| \text{ and also}$$

$$\pi_i \pi_\gamma = \pi_f \tag{2.36}$$

where π_i and π_f are the parities of the initial and final states and $\pi\gamma$ is the parity of the electromagnetic wave given by $\pi_\gamma = \pm 1$. Further $M = \Delta m = m_i - m_f \leq L$ where L is the multipolarity of the transition. The majority of Mössbauer isotopes decay by dipole or quadrupole transitions and is summarised below in Table 2.1.

Table 2.1: Classification of electromagnetic transitions.

L	$\pi\gamma$	Notation	Transition
1	+1	M1	Magnetic dipole
	-1	E1	Electric dipole
2	+1	E2	Electric quadrupole
	-1	M2	Magnetic quadrupole

By adopting selections rules discussed above, only six transitions are allowed for ^{57}Fe and this is shown in Figure 2.6.

2.2.5 Combined Magnetic and Quadrupole Interactions

A nuclear state can be perturbed simultaneously by the electric monopole, magnetic dipole and electric quadrupole interaction provided $E_M \leq E_Q$ or $E_Q \leq E_M$. For a $\frac{3}{2} \leftrightarrow \frac{1}{2}$, the quadrupole interaction can be treated as a first order perturbation to the magnetic interaction provided the EFG tensor is axially symmetric. The general expression for the eigenvalues of the energy levels is given by[62]:

$$E_{M,Q}(I,m_I) = -g_N \beta_N H m_I + (-1)^{|m_I|+\frac{1}{2}} (eQV_{zz}/8)(3\cos^2\beta - 1) \qquad (2.37)$$

where β is the angle between the magnetic axis and the major axis of the electric field tensor. Figure 2.4 shows the combined magnetic and quadrupole splitting for ^{57}Fe.

2.2.6 Relative Intensities of Resonance Lines

The transition probabilities or line intensities of the hyperfine components in a Mössbauer spectrum are determined by spin and parity of the excited and ground states of the nucleus as well as the multipolarity of the transition and geometric configuration.

Consider now the M1 and the E2 transition in ^{57}Fe ($I = \frac{3}{2} \leftrightarrow I = \frac{1}{2}$) where E2 is fairly negligible. The probability P for this nuclear transition from a state $|I_1, m_1\rangle$ to a state $|I_2, m_2\rangle$ is equal to:

$$P(3/2\, m_{3/2}, 1m \left| 1/2, m_{1/2}, \theta, \phi \right.) = \left| \left\langle 3/2, m_{3/2}, 1m \left| 1/2\, m_{1/2} \right. \right\rangle^2 F_{1m_{1/2}}^{1m_{3/2}}(\theta, \phi) \left\langle \left\langle I_1 \| 1 \| I_2 \right\rangle \right|^2 \qquad (2.38)$$

where θ, ϕ can define the direction of the magnetic field and the direction of the γ-ray emission. $\langle I_1, m_1, Lm | I_2 m_2 \rangle$ are the Clebsch-Gordan coefficients which is a product of the vectors $\vec{I}_1$, $\vec{L}$, $\vec{I}_2$ and $\langle I_1, \| 1 \| I_2 \rangle$ which does not depend on the magnetic numbers. The angular dependent term $F_{1m_{1/2}}^{1m_{3/2}}(\theta, \phi)$ does not depend on the quantum numbers I, m_I. For the above transition, the Clebsch-Gordan coefficients[63] are given below in Table 2.2.

Table 2.2: Values of the Clebsch-Gordan coefficients of a $I_e = 3/2$, $I_g = 1/2$ magnetic dipole and electric quadrupole transition.

$M_{3/2}$	$M_{1/2}$	M	$\langle 3/2\, m_{3/2}, 1m \mid 1/2\, m_{1/2} \rangle$	$\langle 3/2\, m_{3/2}, 2m \mid 1/2\, m_{1/2} \rangle$
$+3/2$	$+1/2$	-1	$+\sqrt{3/6}$	$+\sqrt{1/10}$
$+1/2$	$+1/2$	0	$-\sqrt{2/6}$	$-\sqrt{2/10}$
$-1/2$	$+1/2$	+1	$+\sqrt{1/6}$	$+\sqrt{3/10}$
$-3/2$	$+1/2$	+2	0	$-\sqrt{4/10}$
$+3/2$	$-1/2$	-2	0	$+\sqrt{4/10}$
$+1/2$	$-1/2$	-1	$+\sqrt{1/6}$	$-\sqrt{3/10}$
$-1/2$	$-1/2$	0	$-\sqrt{2/6}$	$+\sqrt{2/10}$
$-3/2$	$-1/2$	-1	$+\sqrt{3/6}$	$-\sqrt{1/10}$

In a magnetic split spectrum as in the case for ^{57}Fe, it was shown in the previous section that after application of the selection rules that only six transitions were allowed corresponding to six components of the γ- line.

The probability of the above nuclear transition is given by:

$$P(\tfrac{3}{2} m_{\frac{3}{2}}, 1m \left| \tfrac{1}{2} m_{\frac{1}{2}} \right.) \propto \left| \left\langle \tfrac{3}{2} m_{\frac{3}{2}}, 1m \left| \tfrac{1}{2} m_{\frac{1}{2}} \right. \right\rangle \right|^2 \qquad (2.39)$$

where the angular dependent term $F_{1m_{\frac{1}{2}}}^{1m_{\frac{3}{2}}}(\theta, \phi)$ averages to unity when all orientations are equally probable.

By considering equation (2.39) and Table 2.2, the relative intensity ratios can be determined as 3 : 2 : 1 : 1 : 2 : 3 for random orientations, i.e. polycrystalline material.

Chapter 3

EXPERIMENTAL DETAILS

Mössbauer Spectroscopy (MS) has been used for many decades, but the method of approach has changed over the last few years. This chapter comprises a description of Mössbauer Spectroscopy in transmission geometry (TMS), Conversion Electron Mössbauer Spectroscopy (CEMS), and finally a novel approach developed by Weyer[45,64] where MS measurements were made after implantation of radioactive ^{57}Mn ions into host samples. The last part of this chapter focuses on software programs used for data analysis.

3.1 Mössbauer Spectroscopy

For ^{57}Fe Mössbauer Spectroscopy, the radioactive source is ^{57}Co which has a half-life of 271.1 days and decays by electron capture to the $I = \frac{5}{2}$ excited state of ^{57}Fe. This decay scheme of the ^{57}Co isotope is shown in Figure 3.1. Also shown in the figure is the $^{57}Mn^{*} \rightarrow {}^{57}Fe^{*}$ nuclear β^{-} decay which also leads to the population of the 14.4 keV Mössbauer level in ^{57}Fe.

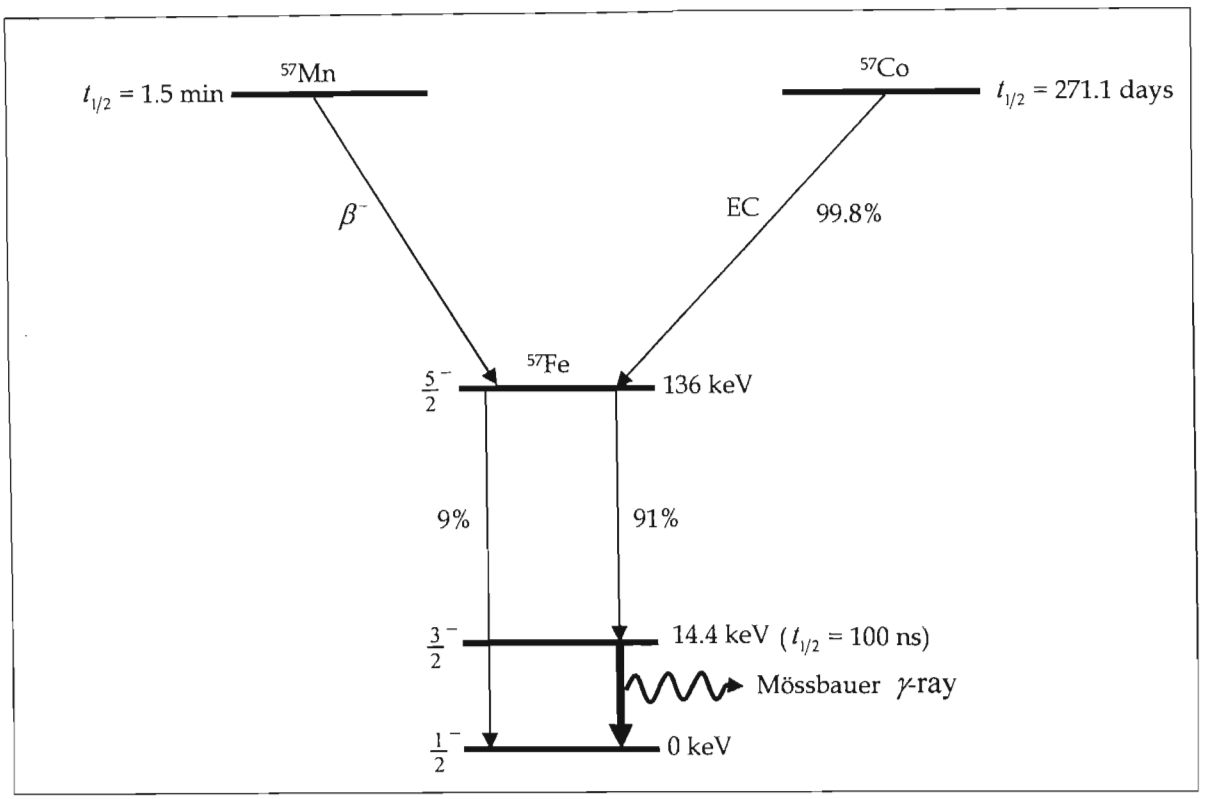

Figure 3.1: Decay schemes of ^{57}Mn and ^{57}Co.

The radioactive source (^{57}Co atoms diffused in a rhodium foil matrix) provides a solid environment for the ^{57}Co atoms with high recoil-free fraction and a cubic, non-magnetic site environment to produce mono-energetic γ-rays.

In a transmission experiment, gamma rays that are emitted by the source pass through the absorber, and then into a detector. For nuclear resonance absorption of γ-rays to be successful, the emission and absorption lines (described in Chapter 2) must coincide or partially overlap. This is achieved by utilizing the Doppler Effect to compensate for the recoil energy loss. In a typical Mössbauer experiment, the source and the absorber are moved relative to each other (either by moving the source and keeping the absorber stationary or vice versa) in a controlled manner and registers transmitted γ-quanta as a function of the Doppler velocity.

3.2 Conversion Electron Mössbauer Spectroscopy

In the previous section, we examined sources in conventional MS which is the usual case of an absorption experiment, involving transmission geometry and the detection of γ-rays. Most measurements are made with transmission geometry, but if the absorber is too thick or an opaque substrate so that the beam cannot pass through or the signal is too small, then scattering techniques have to be employed. Scattering is particularly useful for (i) surface analysis, (ii) very thick samples and (c) small Mössbauer effects due to sample size or low f-factor.

The importance of this geometry is that it makes possible for the study of bulk samples. When detecting electrons, a thinner surface film is observed. Electrons with energy of about 10 keV are stopped within a material when coming from deeper and this technique is called Conversion Electron Mössbauer Spectroscopy (CEMS) and is important for surface studies of implanted systems, corroded products, catalysts etc.

A nucleus that is promoted to an excited state by γ-ray absorption can de-excite by a number of ways and these are:

(a) Radiative: by the emission of a gamma ray with a probability $N(\gamma)$ and

(b) Non-Radiative: by internal conversion and the ejection of an atomic electron with a probability of $N(e)$.

The ratio of these processes is given by the internal conversion coefficient, α, given by:

$$\alpha = \frac{N(e)}{N(\gamma)}$$

which is 8.21 for ^{57}Fe, i.e. the internal conversion is 8.21 times more probable than the photon emission.

The conversion electron is ejected from an atom with an energy given by:

$$E_c = E_\gamma - E_b$$

where E_γ is the energy of transition and E_b is the binding energy of the electron. In ^{57}Fe, the internal conversion can occur from the K, L and M shells, in order of probability. The ejection leaves a hole which is filled by an electron from an outer shell and this releases energy in the form of an X-ray or an Auger electron, with the process continuing in this manner until all the energy has been dissipated. The principal decay scheme is shown in Figure 3.2.

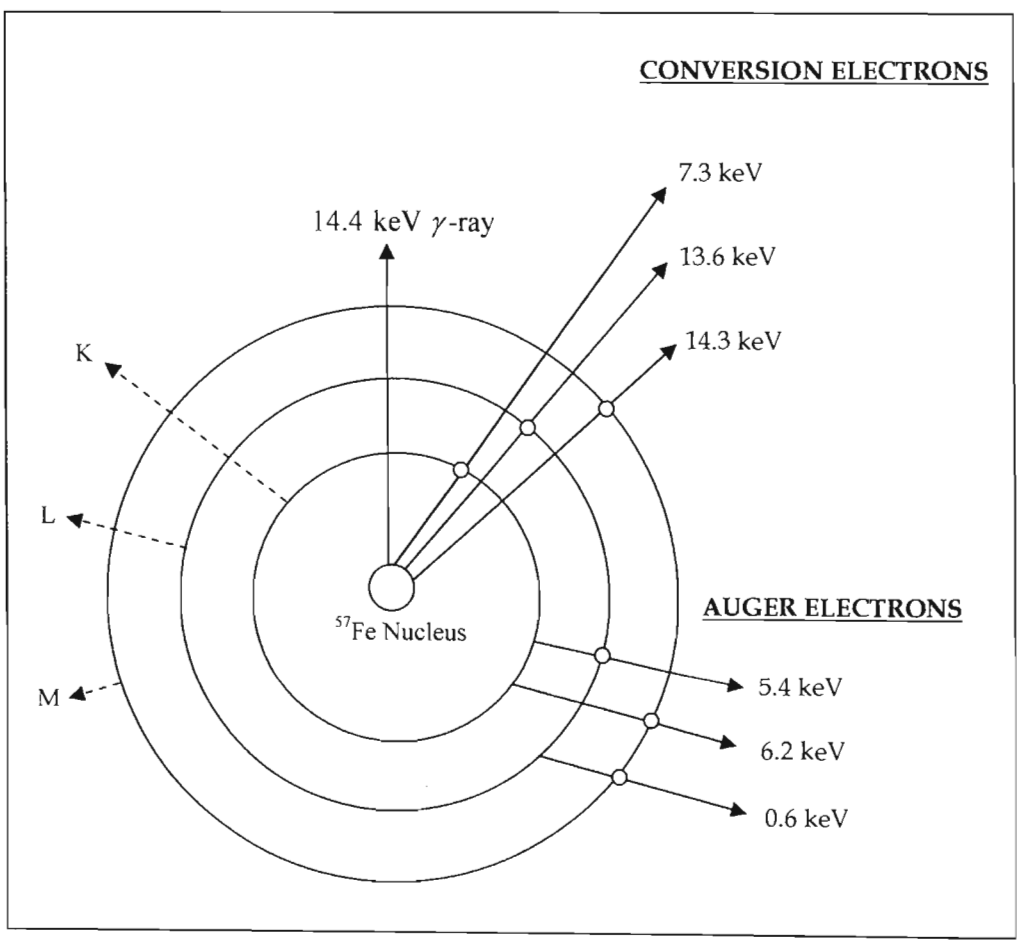

Figure 3.2: Decay scheme of ^{57}Fe following excitation of the 14.4 keV state.

To utilize the decay of the resonantly excited nucleus, the conversion and Auger electrons need to be detected. In our measurements, this is achieved by placing a sample inside a gas-flow proportional counter as shown in Figure 3.3.

3.2.1 CEMS Detector

CEMS uses the emission of conversion electrons from the decay of the 14.4 keV state (see Figure 3.2) in the absorber to record a spectrum. This technique is useful for samples with thick substrates which would block transmission of γ-rays or for the studies of the surfaces of samples rather than bulk. As the ratio of conversion electrons to γ-rays emitted by the 14.4 keV Mössbauer event in ^{57}Fe is 8.21, the counting efficiency of CEMS is much greater than that of the transmitted γ-photons.

A schematic diagram of the CEMS detector used during the measurements is shown in Figure 3.3. The design of the detector is based on the principles of the parallel plate avalanche counter (PPAC) developed by Weyer[65].

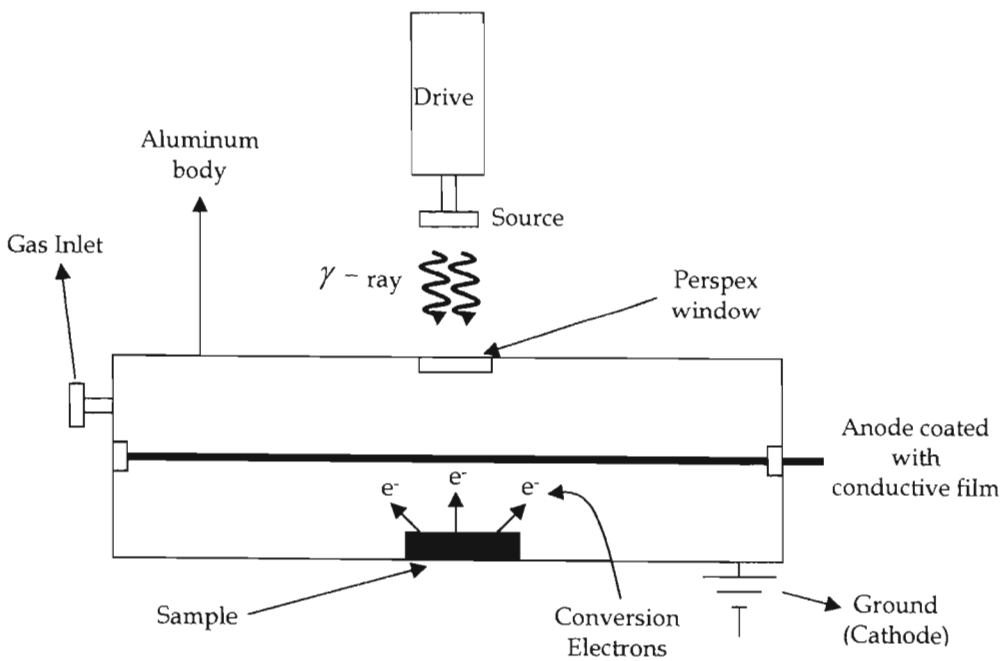

Figure 3.3: A schematic diagram of the CEMS detector showing all components.

The body of the detector was made out of aluminium (low atomic mass) which is commonly used in detector design as it is fairly lightweight, cost effective and easy to engineer for a specific design. Further, it has good shielding properties preventing external signals from reaching the inside of the detector. The inside of the detector consists of two perspex plates mounted in parallel with a plate space of about 1.5 mm. The inner surfaces of these plates were coated with a conducting layer which is applied using a graphite aerosol spray. One disk acts as an anode and the other as the cathode which is connected to the body of the detector. The samples used during the experiment were mounted on the cathode. The anode is maintained at a voltage of approximately 450 V directly in front of the sample. The source irradiates the sample through the window. Electrons emitted from the sample are accelerated towards the anode, ionizing atoms in the counting gas, producing an avalanche effect which amplifies the signal from the original emitted electron. This electronic pulse is detected and recorded similar to TMS.

The counting gas used consists of a mixture of 90% helium and 10% methane and was constantly refilled from a gas reservoir. During measurements, the detector gas pressure was maintained at 50 mbar. The mixture of gas removes any contaminants such as oxygen from the atmosphere which would reduce the counting efficiency. The methane acts as a quenching gas, preventing the helium ions reaching the cathode. The helium/methane gas has negligible reaction with the incident 14.4 keV γ-rays making it transparent to the incident radiation.

The perspex window attenuates 6.3 keV X-rays from the source which would otherwise produce a large background signal to noise from non-resonantly emitted electrons, but only attenuates the 14.4 keV γ-ray by a small amount.

3.2.2 CEMS Measurements

The main aim of the experiment was to investigate the annealing characteristics of Fe implanted in diamond using source based CEMS with the parallel plate detector system

as described in section 3.2.1. CEMS measurements were carried out using a 30 mCi ^{57}Co(Rh) source. The samples used were two synthetic diamonds that were fabricated by High-Temperature High-Pressure (HTHP) and Chemical Vapour Deposition (CVD) processes. The CVD diamond was produced by high power microwave deposition on a silicon substrate and after growth, the substrate was removed. The nitrogen concentration in the CVD diamond was < 5 ppm. The HTHP sample was single crystal whereas the CVD sample was polycrystalline with and average crystallite size of $100\,\mu m$. This is several orders of magnitude larger than the estimated mean implantation range (310 $\mathring{A}$) and straggle (90 $\mathring{A}$) of the Fe probe atoms. The majority Fe probe atoms were implanted in single crystal environment with the remainder at the grain boundaries.

The HTHP and CVD diamond samples were implanted with 70 keV ^{57}Fe ions to a dose of 5×10^{14} cm^{-2} and followed by the first set of CEMS measurements on the as-implanted samples. The samples were then annealed for 10 minutes in vacuum at an annealing temperature of 600 K after which the second set CEMS measurements were performed. This process was repeated with the samples annealed at 950 and 1400 K.

3.3 Mössbauer Spectroscopy following implantation of ^{57}Mn ions

This experimental approach was utilized at the Isotope Separator On Line (ISOLDE) at CERN, the European Organization for Nuclear Research[66]. We start this section by first looking at the CERN accelerators, followed by a description of the ISOLDE facility and finally the experimental setup and measurements performed using the Weyer approach.

3.3.1 The ISOLDE Facility at CERN

A layout of the CERN complex is shown in Figure 3.4. At CERN, proton beams are produced for a variety of experiments at the Proton Synchrotron (PS), the Super Proton Synchrotron (SPS) and the future LHC[60]. The accelerators are fed with protons by the Proton Booster Accelerator (PSB) with energies of 1.0 or 1.4 GeV and an intensity of 2 μA is suitable for the production of radioactive ion beams[67,68].

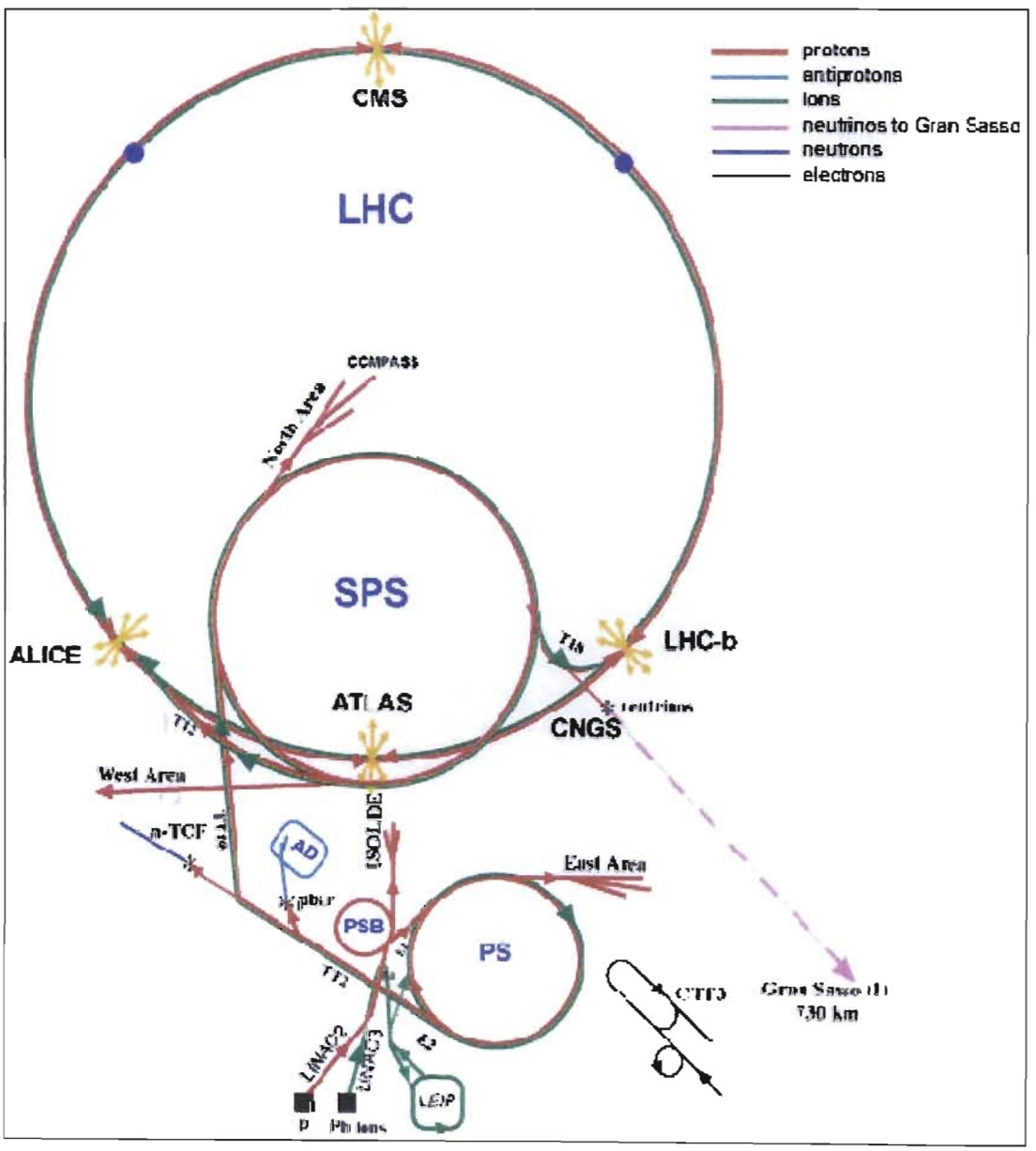

Figure 3.4: A layout of the CERN complex[68].

The protons from the PSB are delivered to the ISOLDE target area via underground transfer line. Radioactive isotopes are produced in a thick target by fission, spallation or fragmentation which then diffuses out and are finally ionized via a plasma, laser or surface ionization source. The singly charged ions, which are accelerated to energy of 60 keV and mass separated, are then accessible for experiments at different beam lines.

The ISOLDE PSB facility has two isotope separators, the General Purpose Separator (GPS) and the High Resolution Separator (HRS). Figure 3.5 shows a schematic view of the ISOLDE laboratory.

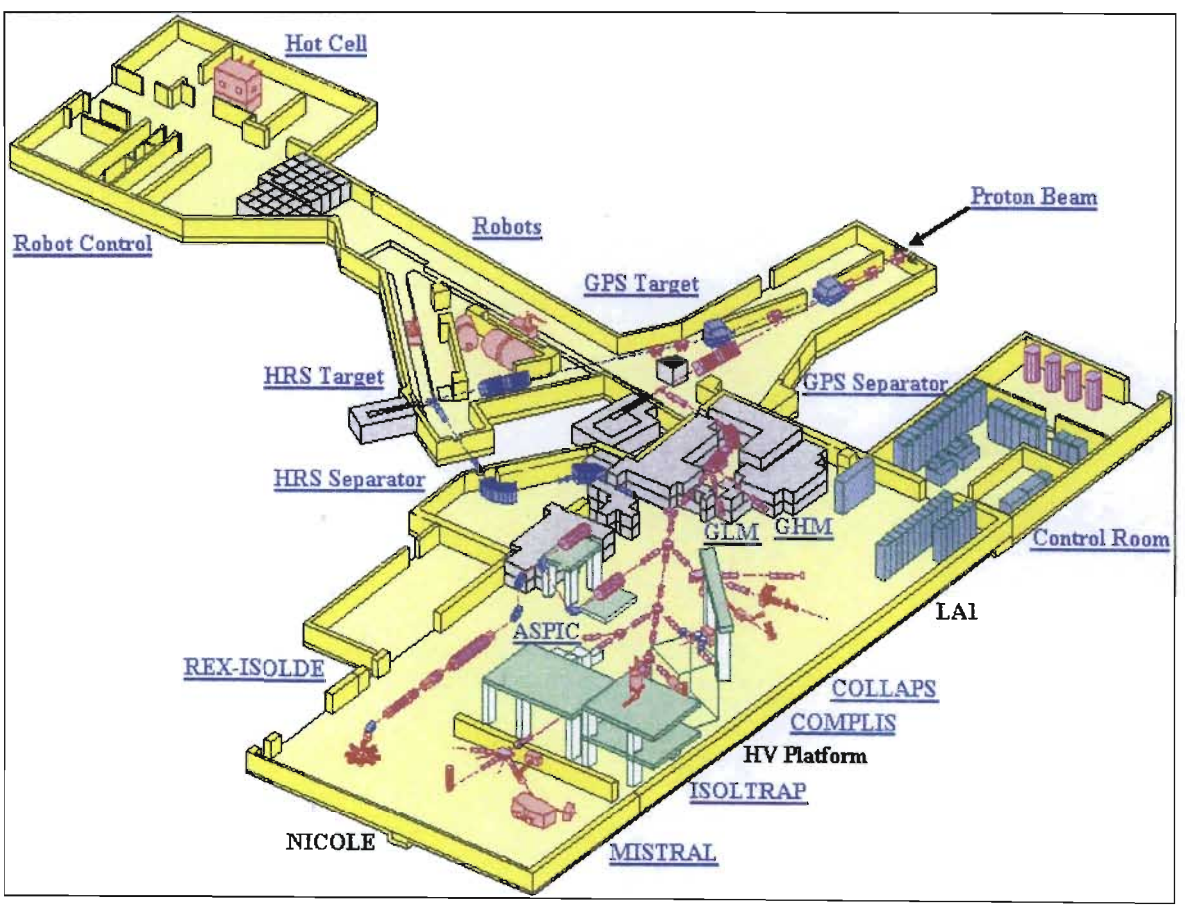

Figure 3.5: A schematic view of the ISOLDE laboratory[67].

The GPS is designed to allow three beams (central mass, low mass and high mass) to be selected and transported into the experimental hall as shown in Figure 3.5.

3.3.2 The ISOLDE Targets and Ion Sources

The target used at the on-line isotope separator is a fast liberator of radioactive nuclei. The combination of the target and ion source produces an ion beam that contains only isotopes from one element. Over the last few years, the ISOLDE group have developed many different target-ion combinations which permit ISOLDE users to investigate radioisotopes from more than 60 different elements. These combinations were achieved with the use of techniques from the fields of radiochemistry (involves metallurgy), high temperature chemistry and surface physics. The targets used at ISOLDE consists of moltens maintained at temperatures between 700 °C and 1400 °C. Target materials made of metal powder, metal and carbides are used at 2000 °C. The targets used at ISOLDE are characterised by long release time of the produced isotopes. There are three different types of ion sources that are currently being used at ISOLDE namely, surface ionization sources, plasma ion sources and laser ion sources. The current experiment used the laser ion source and a description of this is given below.

The laser ion source has been developed to ionize isotopes of elements which were not ionized efficiently by other types of ion sources and clean beams. The laser system is effective in this regard because the laser ion source works on only atoms of the element and the laser wavelengths are tuned for chemical selectivity; the isobaric contamination is therefore reduced to small amounts, which result due to surface ionization inside the tube where laser ionization takes place. The GPS, laser system and target ion source unit is shown in Figure 3.6.

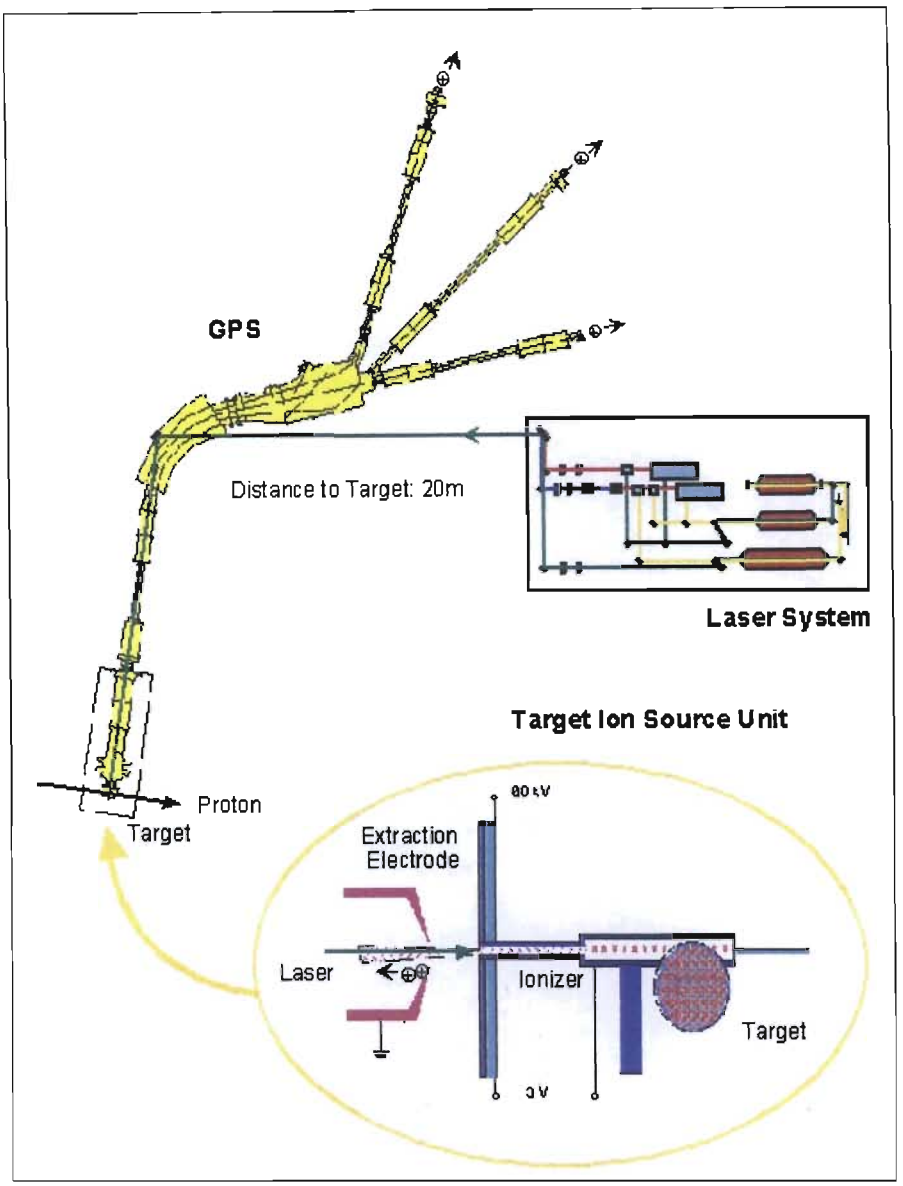

Figure 3.6: The GPS, laser system and target ion source unit[67].

A detailed illustration of the laser system is shown in Figure 3.7. The system consists of copper vapours, tuneable dye lasers and non linear crystals for frequency magnification (factor of 2 or 3) presenting the possibility for very two or three step ionization.

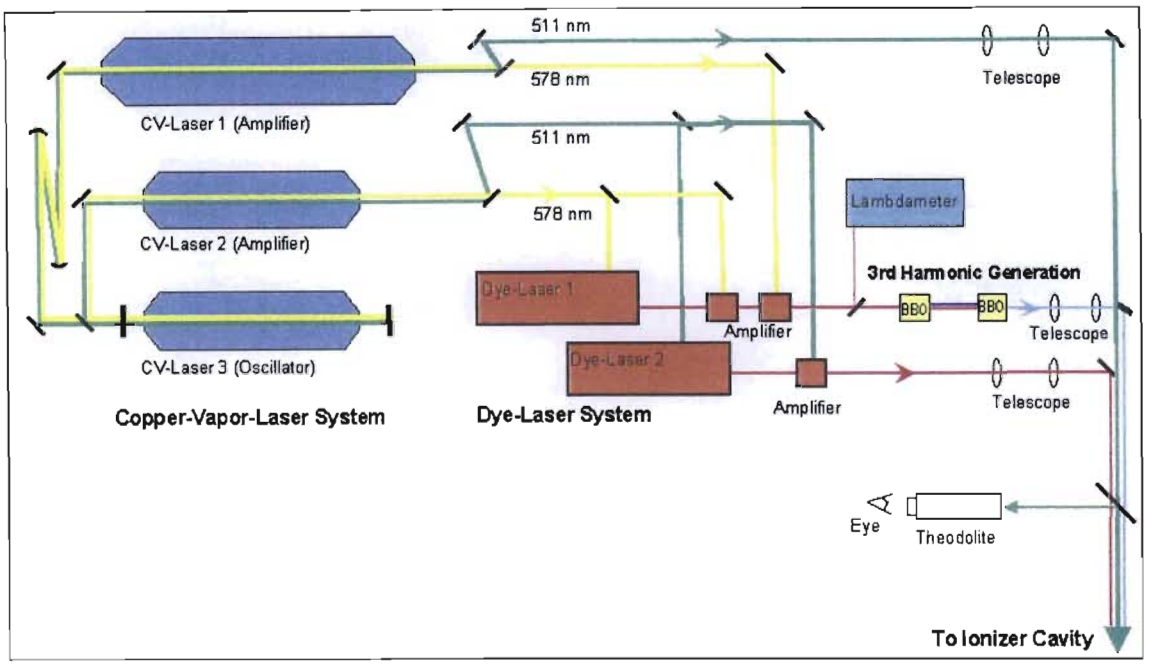

Figure 3.7: The laser system at ISOLDE[67].

The handling of targets is carried out by two industrial robots, similar to those used in automobile industry. The combination of the target and the ion-source serves as a small chemical factory for converting nuclear reaction products into a radioactive beam. An electric field accelerates the ions which are then mass separated and directed to the experiments.

3.3.3 ^{57}Mn Experimental Setup

The main components of our setup consist of an implantation chamber, Mössbauer drive unit, resonance detector, sample holder and the necessary electronics. The layout of experiment is shown in Figure 3.8. The detector was found to operate efficiently with acetone (99.99% pure) as counter gas at a pressure of 40 mbar.

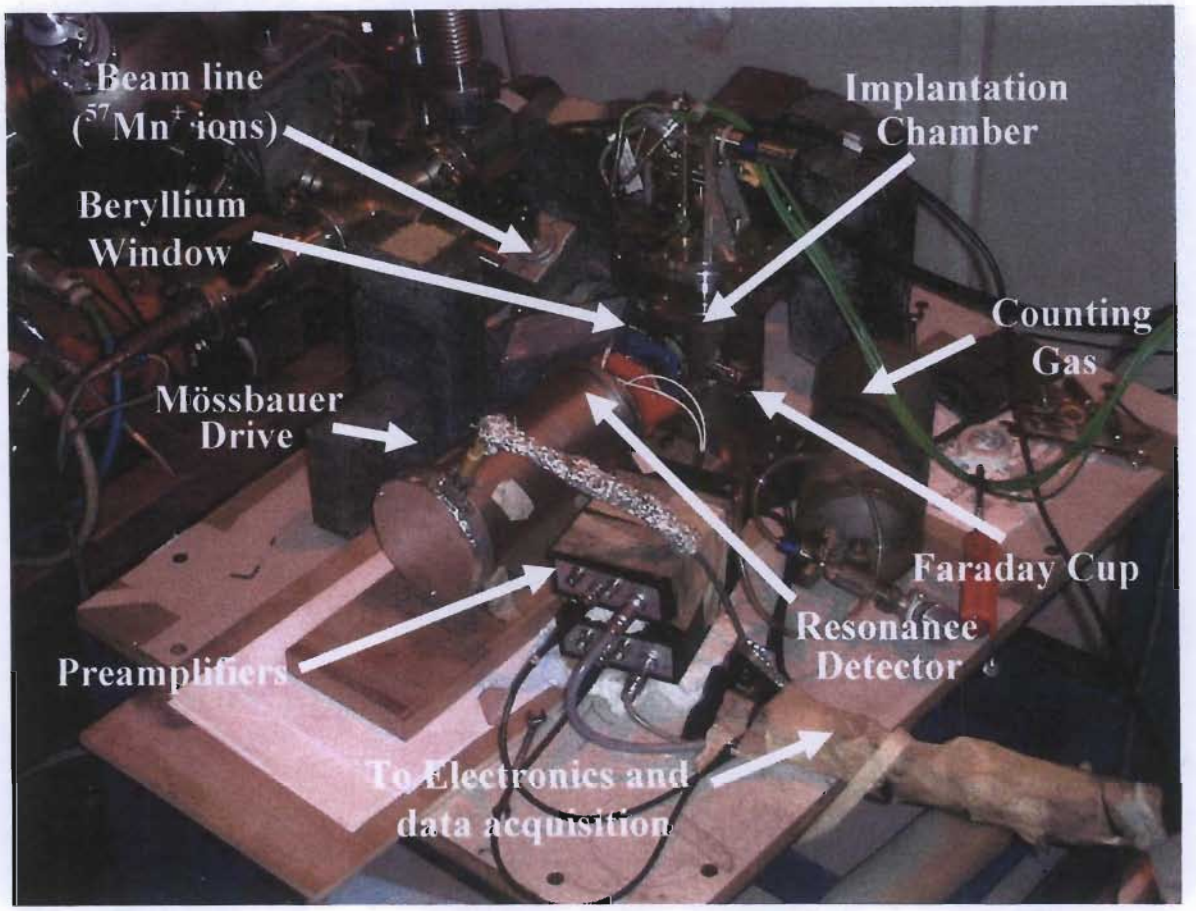

Figure 3.8: Experimental setup for Mössbauer Spectroscopy studies.

The usual procedures of beam spot alignment and background reduction were performed prior to the commencement of measurements. The host samples were mounted in an implantation chamber, on a holder which was designed to hold a maximum of four samples as shown in Figure 3.9. The sample holder was oriented at an angle of 45° with respect to the beamline. The design of the sample holder allowed a number of samples to be measured across the temperature range in a given series. Sample temperatures were monitored with the aid of thermocouples attached on the sample holder close to the different sample positions. Samples were held at temperatures between 300 and 1100 K with use of an Osram photo-optic lamp (150 W, 15 V). The implantation chamber was kept under constant vacuum of 10^{-6} mbar. The 14.4 keV gamma rays passed from the implanted target to the detector through Be windows.

Mössbauer spectra were collected using light-weight resonance detectors which were mounted on a velocity drive unit outside the implantation chamber as shown in Figure 3.8. The detectors were equipped with enriched stainless absorbers or with four 150 nm thick α-^{57}Fe layers on beryllium disks which acts as electrodes.

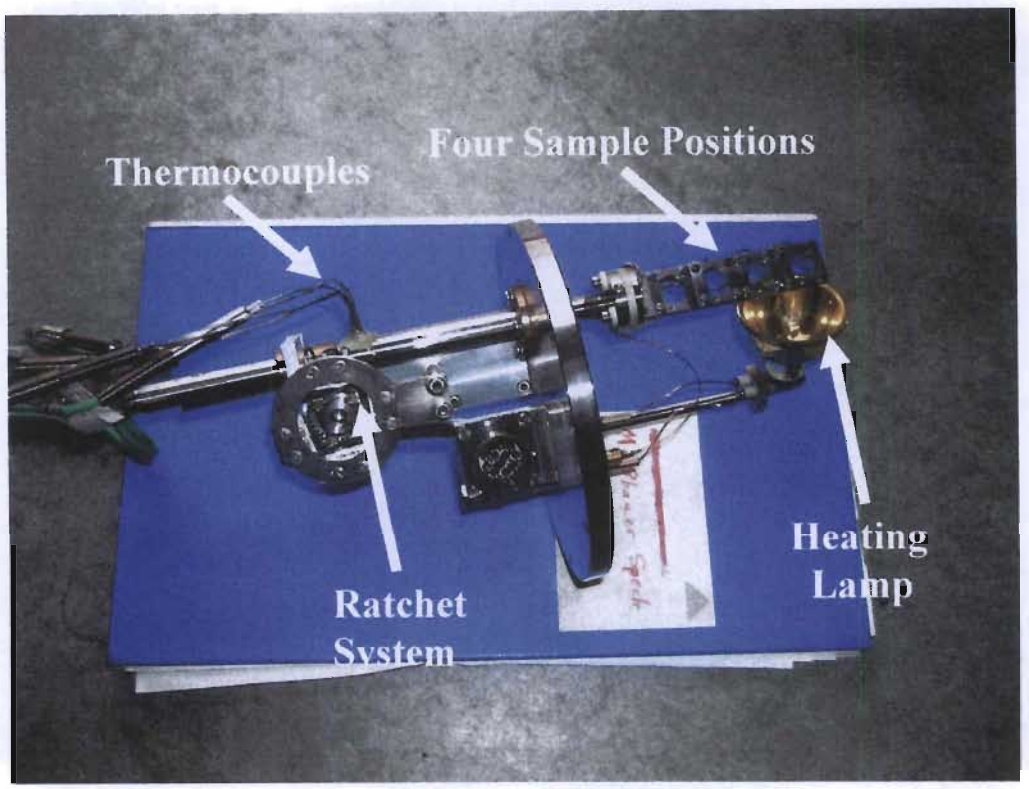

Figure 3.9: The sample holder used in the implantation chamber.

3.3.4 The ^{57}Mn Method and Measurements

The experimental method adopted in this experiment is based on the novel approach recently developed by Weyer[45,64] of incorporating ^{57}Fe Mössbauer probe nuclei in host nuclei. In this technique, a beam of radioactive $^{57}Mn^{+}$ ions ($t_{1/2}$ = 1.5 min) with intensities $\geq 10^{8}$ s^{-1} are produced at ISOLDE, using the 1.4 GeV proton-induced nuclear fission in a UC_2 target. The ^{57}Mn atoms were selected via multiphonon resonant laser ionization, and following mass separation. Clean beams of $^{57}Mn^{+}$ were accelerated to 60 keV and implanted into the samples under investigation placed in the implantation

chamber (See Figure 3.8). The low-fluence implantations ($<10^{12}$ cm^{-2}) of $^{57}Mn^{+}$ ions were employed which effectively rules out graphitization effects and/or the overlap of defect cascades from individual ions.

The lifetime of $^{57}Mn^{*}$ (1.5 min) is long enough to allow for the annealing of radiation damage to occur at increasing temperatures, before the Mn decay and the measurement of ^{57}Fe Mössbauer spectra. The implantation and annealing processes results in the majority of the implanted Mn ions occupying substitutional lattice sites[48]. In the subsequent ^{57}Mn nuclear β^{-}-decay to the 14.4 keV Mössbauer state of ^{57}Fe ($t_{1/2}$ = 100 ns), an average recoil energy of 40 eV is imparted to the ^{57}Fe daughter atoms which results in a large fraction being expelled into tetrahedral interstitial sites and the creation of a vacancy. The remainder occupy substitutional sites. This method of recoil production of $^{57m}Fe_i$ suggests an insignificant possibility for their association with other impurities in heavily doped material.

For the SiGe alloys and Ge samples, the ^{57}Fe detector was used which resulted in a complicated six-fold emission spectrum due to the internal magnetic field in Fe. This detection method is much superior to the stainless steel based resonance detectors due to the narrow absorber line width resulting in excellent detection efficiency and resolution. A further advantage of this detection method is that the spectra are internally calibrated whereas in the case of the stainless steel detection system, calibration needs to be performed prior to fitting. The stainless steel absorbers were used when the diamond samples were measured due to the range of isomer shifts $\approx 2.0(5)$ mm/s. The benefit of the Weyer approach coupled with the efficient detection systems produced exceptionally high counting rates which is much superior compared to TMS and CEMS. The average count rate during the experimental run was in the region of 3500 counts/s which allowed us to measure a spectrum in an average time of 10 minutes. The annealing behaviour (12 to 15 temperature steps) of a sample is thus measured within 3 hours. In a period of approximately 72 hours, 350 odd spectra were collected on a variety of samples which includes time utilized for sample exchanges.

3.4 Fitting and Plotting Routines

The Mössbauer spectra for the various measurements were initially read into an analysis code called VINDA[69], and calibrated with the spectrum for $\alpha-$Fe at room temperature. The data was then transformed into free-form, ready for fitting in a Mössbauer analysis code called RECOIL[70]. RECOIL was used in combination with Microsoft Excel based on the macros from Microsoft Visual Basic Applications (MVBA), and the Solver to ensure that the spectral line positions followed the temperature dependent second order Doppler shift and that the quadrupole split components adhered to the $T^{3/2}$ temperature dependence.

In RECOIL, the extended Voigt-based fitting (xVBF) routine[70] was used. This method provides a means to achieve multidimensional distributions of hyperfine parameters for paramagnetic and magnetic generalized sites. Non-magnetic generalized sites have simultaneous distributions of centre shifts and quadrupole splittings whereas magnetic generalized sites have distributions of magnetic hyperfine fields. Each hyperfine parameter distribution is characterized by a sum of Gaussian components, permitting a flexible lineshape. The model parameters consist of the global parameters, Lorenztian (HWHM) and background. The non-magnetic sites were analysed using the following parameters: total spectral area, ratio of spectral areas, isomer shift, Gaussian width and the average quadrupole shift (when required) whilst the magnetic sites used the hyperfine magnetic field parameter. A χ^2 fit to the data gives hyperfine parameters and site fractions.

Chapter 4

RESULTS AND DISCUSSION

This chapter focuses on the analysis and interpretation of data obtained from: (i) Conversion Electron Mössbauer Spectroscopy (CEMS) measurements on as-implanted HTHP Type Ib and CVD synthesized diamond samples (see Chapter 3, section 3.2.2) and (ii) Mössbauer Spectroscopy (MS) following ^{57}Mn implantation into Type IIa natural and CVD diamond samples, and SiGe alloys of varying concentrations of Ge and Ge samples (see Chapter 3, section 3.3.3). The first section of this chapter presents results from the CEMS measurements with special attention given to the structural changes observed in the spectra. The Mössbauer hyperfine parameters determined from analysis procedures were the isomer shift, population of sites, linewidths and quadrupole splittings. These were determined using a Mössbauer analysis code called RECOIL in combination with the solver optimization routine in Microsoft Excel. The various procedures of the fitting process are discussed in detail in the APPENDIX.

This is followed by a presentation of the spectra and results obtained from MS ^{57}Mn implantation measurements on Type IIa natural and CVD diamonds implanted with radioactive ^{57}Mn*, with importance placed on the extracted hyperfine parameters and some derived physical quantities. The results of measurements on ^{57}Mn* implanted SiGe alloys and Ge are presented and discussed in Section 4.3. The final section includes a comparison of the results obtained for the diamond, SiGe and Ge data.

4.1 CEMS Measurements on HTHP and CVD diamonds implanted with ^{57}Fe

The spectra obtained from the CEMS measurements on HTHP and CVD synthesized diamonds implanted with 5×10^{4} cm^{-2} of ^{57}Fe are shown in Figures 4.1 and 4.2. The spectra were collected on the as-implanted samples and after annealing at the temperatures of 600, 950 and 1470 K. The CEMS spectra for the HTHP diamond over the entire temperature range were very similar to each other and are dominated by broad doublet indicative of the presence of several unresolved components due to a distribution of electric field gradients which is a feature associated with highly defective or amorphous regions in implanted samples. For CVD diamond, the spectra exhibit similar features to that of the HTHP sample up to 950 K but after annealing at 1470 K, a dramatic change in the spectra was observed.

Both sets of data were fitted with two doublets (D1 and D2) and two singlets (S1 and S2) which have been observed in earlier results for natural diamond samples[23,28,30,71]. The two single lines (S1 and S2) have been previously ascribed to interstitial and substitutional Fe, respectively. The decomposition of spectra into the above components gave a consistent description of the results in the temperature range. A weak third doublet, D3 with quadrupole splitting of 3.23(3) mm/s was included in the analysis to fit the wings of the resonance spectra for the HTHP data. For the CVD diamond, no third doublet was required but an additional single line (S3) was required at 1470 K. This is discussed again in chapter five. For the CVD diamond, the intensity of both doublets (D1 and D2) decreased sharply indicating to the annealing of implantation damage. Annealing at 1470 K resulted in the appearance of a strong single line (S1) with isomer shift of -0.94(5) mm/s, together with a second line (S2) with isomer shift of +0.03(5) mm/s. A third line (S3) with isomer shift of -0.02(5) mm/s also became evident. For the HTHP diamond, annealing of the damage site was very gradual as compared to CVD diamond and two singlets, S1 and S2 were present in the spectra with isomer shifts of -0.84(4) and 0.11(5) mm/s, respectively. The isomer shifts obtained for the S2 component for both the CVD and HTHP diamonds are in good agreement with the value of 0.16(4) mm/s obtained from the IBMS measurement[31].

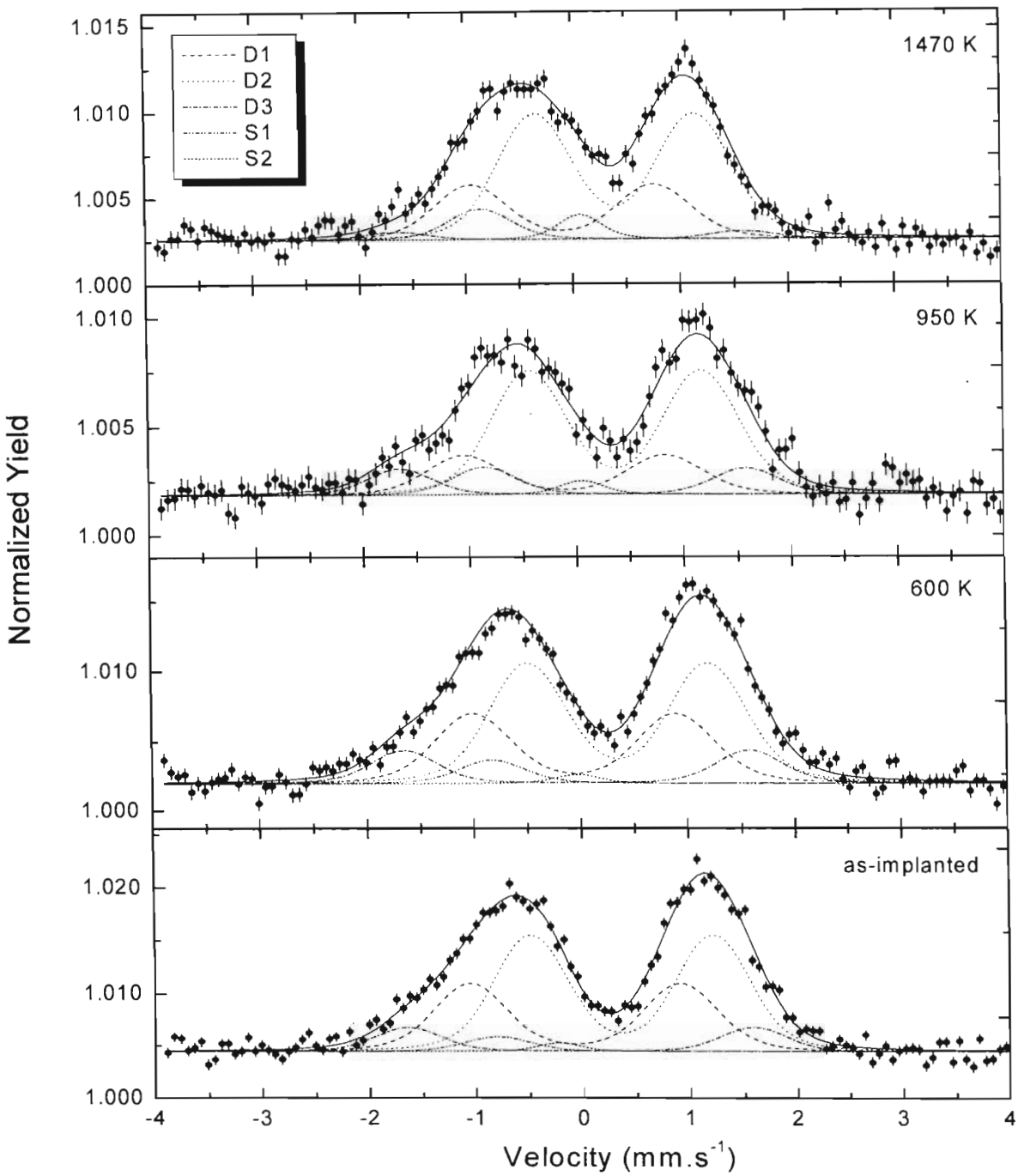

Figure 4.1: CEMS spectra of ^{57}Fe implanted in HTHP synthesized diamond observed at the annealing temperatures indicated.

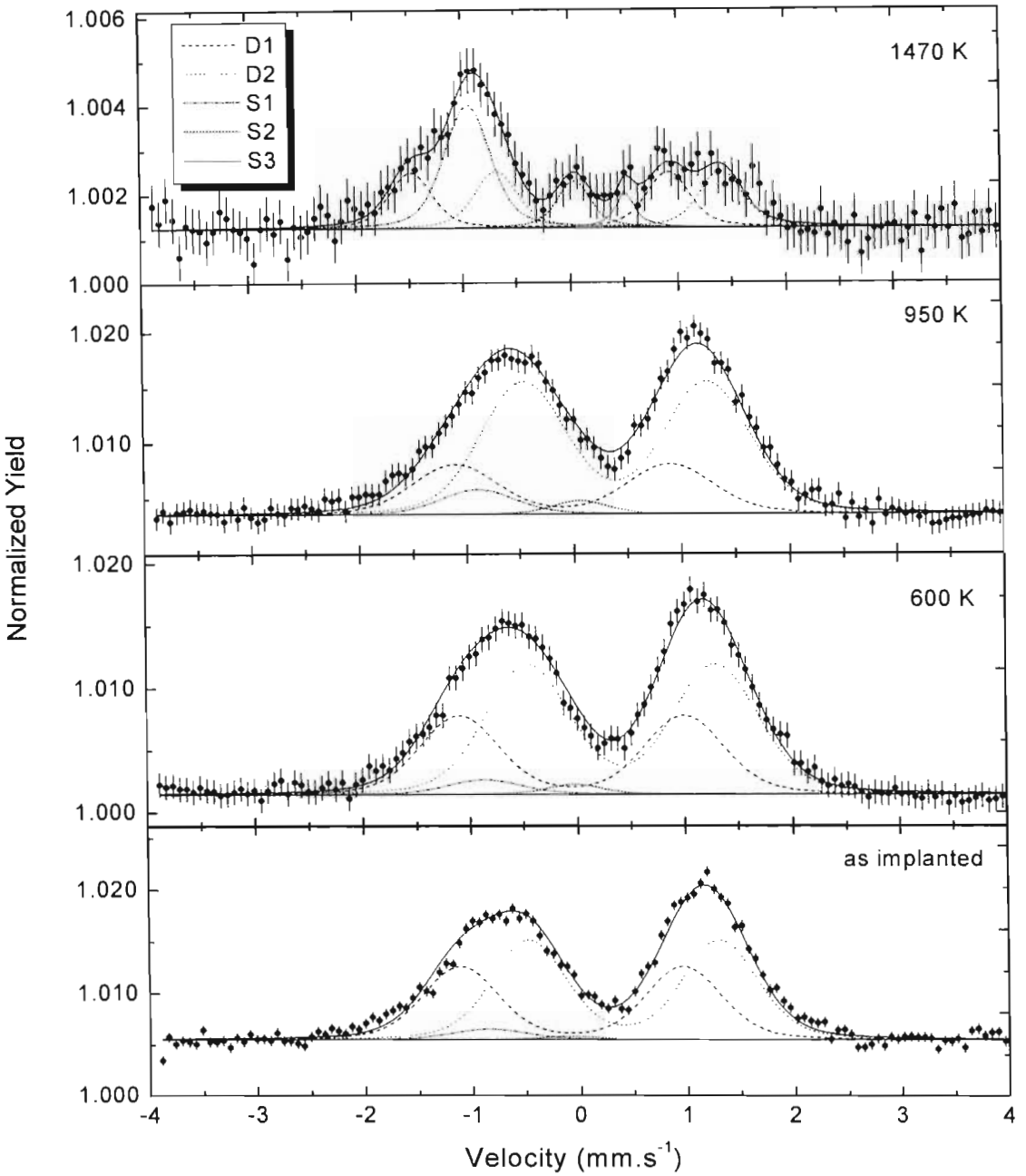

Figure 4.2: CEMS spectra of ^{57}Fe implanted in CVD synthesized diamond observed at the annealing temperatures indicated.

The single line component S1 with isomer shifts of -0.94(5) mm/s obtained in the HTHP and CVD CEMS measurements, respectively compares well with the value of -0.95(3) mm/s observed previously[25,26,30,71,72]. The large negative isomer shift of S1 is indicative of the large *s*-electron density at the sites of Fe nuclei responsible for this component and is one of the highest values obtained compared to those of other elemental hosts studied either by ion implantation or doping techniques[72,73]. This is accounted for by the very small volume (atomic radius of carbon atom ≈ 0.77 Å) available for sites in the diamond matrix, resulting in large compression of the *s*-electron shells of the Fe atom volume (atomic radius of Fe atom ≈ 1.26 Å).

Ingalls[73] has performed Mössbauer spectroscopy measurements at external pressures up to 300 kbar to investigate the influence of the volume compression on the isomer shift of ^{57}Fe in various metals. The value of the pressure coefficient $(\partial\delta/\partial p)$ in metals was determined to be in the region of 6×10^{-4} mm/s kbar thus the value of the isomer shift for a single line of Fe in $\alpha-C$, -0.95 mm/s, corresponds to an internal pressure of ≈ 1500 kbar. Ingalls concluded that this large pressure for a HS site of Fe in diamond is due to extremely strong bonds between carbon atoms in the diamond resulting in its extreme hardness and due to the vast difference in the atomic volumes of host and impurity.

For the HTHP measurements, the isomer shifts of D1, δ = -0.09(5) mm/s and D2, δ =0.39(5) mm/s and that for CVD diamond D1, δ = -0.08(5) mm/s, D2, δ =0.42(5) mm/s are in very good agreement with each other and also with values obtained by Bharuth-Ram *et al.*[74]. The quadrupole splitting of these sites were determined as 1.97(5) and 1.71(5) mm/s for HTHP diamond and 2.08(5) and 1.78(5) mm/s for CVD diamond, respectively. The quadrupole splitting showed a slight reduction with increasing temperature. The Mössbauer parameters of the different components obtained using least-square analysis for the HTHP and CVD diamond are presented in Table 4.1 together with

the IBMS results obtained by Bharuth-Ram *et al.* The isomer shifts are expressed as absorbers shifts relative to α -Fe.

Table 4:1: Hyperfine parameters obtained from the CEMS measurements on synthetic HTHP and CVD diamond together with the results from the IBMS experiment.

Comp.	IBMS		CEMS:HTHP		CEMS: CVD		Linewidths
	δ (mm/s)	ΔE_Q (mm/s)	δ (mm/s)	ΔE_Q (mm/s)	δ (mm/s)	ΔE_Q (mm/s)	Γ (HWHM) mm/s
S1	-	-	-0.84(5)	-	-0.94(5)	-	0.50
S2	+0.16 (4)	-	+0.11(5)	-	+0.03(5)	-	0.30
S3	-	-	-	-	-0.02(5)	-	0.20
D1	+0.04 (4)	2.10 (5)	-0.09(5)	1.97(5)	-0.08(5)	2.08(5)	0.60
D2	-0.51	2.33 (5)	+0.39(5)	1.71(5)	+0.42(5)	1.78(5)	0.60
D3	-	-	-0.03(5)	3.23(5)	-	-	0.50

The intensities of these components for the HTHP and CVD diamond are plotted in Figures 4.3 and 4.4, respectively as a function of annealing temperature. For both diamond samples, the intensities of the total defect (D1+D2) was similar to the IBMS results, where over 90% of the resonance strength was in the two doublets and they show no observable temperature dependence. For the HTHP diamond, the annealing of the damage sites was very gradual, decreasing from 95% to 87%. The spectral intensity of doublet D1 decreased from 33% to 30% whilst doublet D2 decreased from 62% to 57%. The two singlets contribute approximately only 7% of the intensity and showed very little change in the spectral intensity over the measured temperature range. The CVD results showed that the spectral intensity of doublet D1 decreased from 42% to 30% whilst doublet D2 decreased from 56% to 34% with a corresponding increase in the intensity of S1 from 3% to 34%. The intensity of S2 remained fairly constant over the temperature interval.

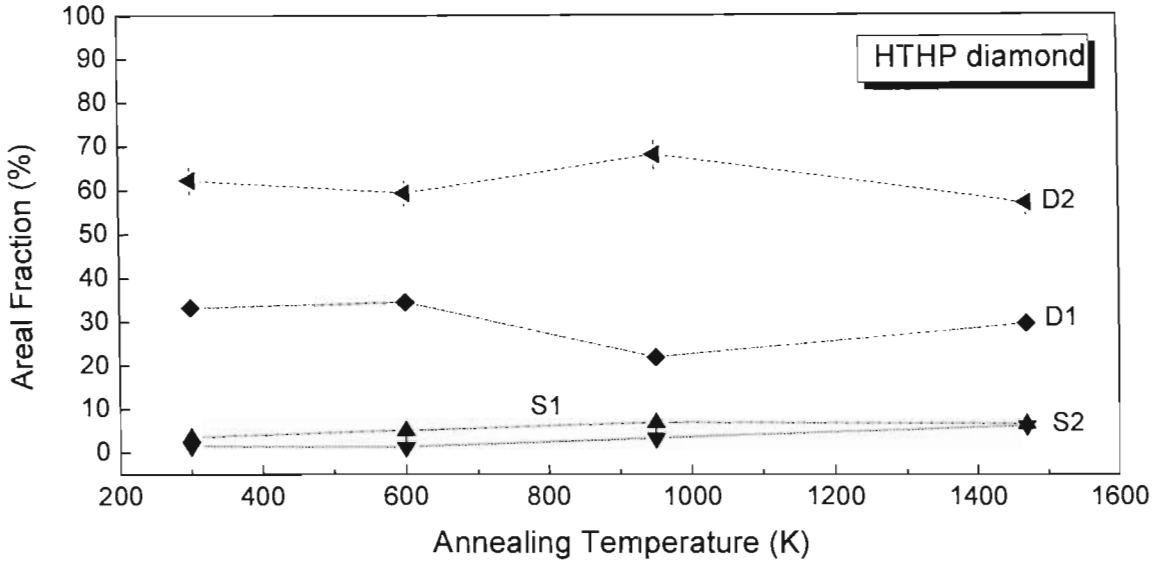

Figure 4.3: **Areal fraction of components as a function of annealing temperature observed in CEMS measurements on HTHP diamond.**

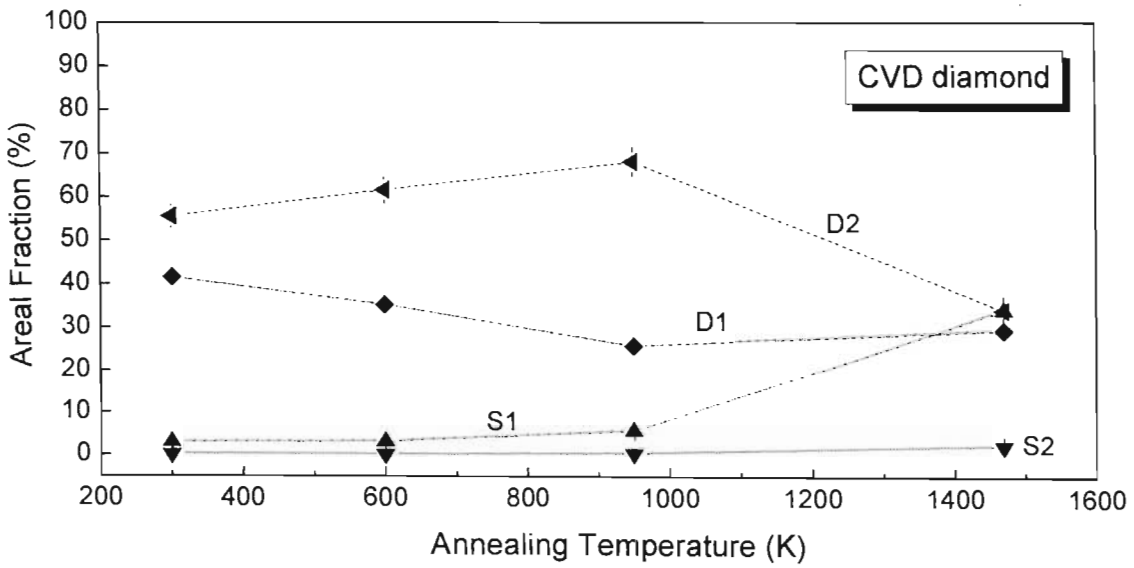

Figure 4.4: **Areal fraction of components as a function of annealing temperature observed in CEMS measurements on CVD diamond.**

4.2 Mössbauer Spectroscopy measurements following ^{57}Mn implantation in Type IIa and CVD diamond

Figure 4.5 shows an X-ray diffraction (XRD) spectrum for CVD diamond determined from a scan (2° per 2θ per minute) with the goniometer of the diffractometer set at a start angle of 30° and a stop angle of 100° using Cu radiation of wavelength, 1.541 Å.

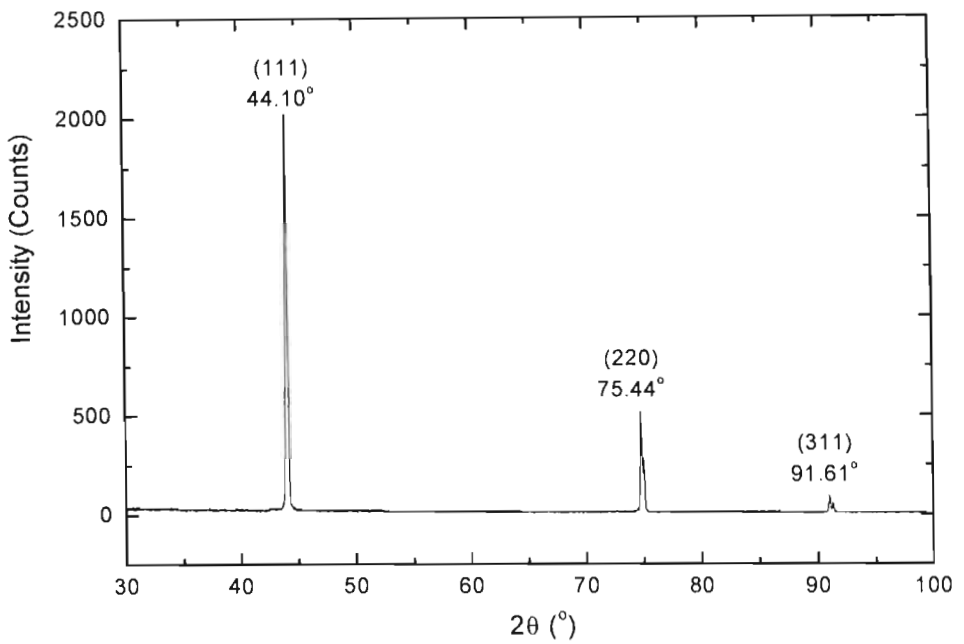

Figure 4.5: X-ray diffraction pattern for CVD diamond.

Three diffraction peaks were observed at 2θ equals 44.10±0.05°, 75.44±0.05° and 91.61±0.05° corresponding to (111), (220) and (311) planes of cubic diamond, respectively. The lattice constant, a_o was determined as ≈3.559 Å which compares well with the value of 0.35668 nm obtained at 300 K (See Table 1.1, Chapter 1). Further, the XRD spectrum for CVD diamond shows little existence of the tail expected from amorphous or graphitized regions which usually has a broad distribution centred at 2θ=26°.

Figures 4.6 and 4.7 shows the ^{57}Fe Mössbauer spectra collected after ^{57}Mn implantation into Type IIa and CVD diamonds held at temperatures between 300-1050 K. The spectral features for both diamond samples at room temperature are very similar exhibiting a symmetric broad structure. At temperatures below 500 K, the spectra are dominated by broad doublets (D1 and D2) and as the implantation temperatures increased above 500 K, the spectra changes markedly with clear evidence of the HS component (S1). The intensity of this line increased quite substantially with increasing implantation temperatures and a second line (S2) became evident.

The spectra were fitted consistently through the temperature range with three asymmetric quadrupole doublets (D1, D2 and D3), and two single lines (S1 and S2) using the high temperature data as a starting point of the analysis (See APPENDIX for analysis procedures). Previous diamond measurements[28,74] also revealed that the spectra consisted of considerable broad structure and were fitted with two doublets. Similar asymmetric doublets have been found for implantations into group IV elements and were attributed to the formation of amorphous pockets[75]; their small size explaining the correlated distribution in the isomer shifts and quadrupole splittings[44,75]. The doublets are assigned to implantation related damage sites, S1 to substitutional Fe and S2 to interstitial Fe.

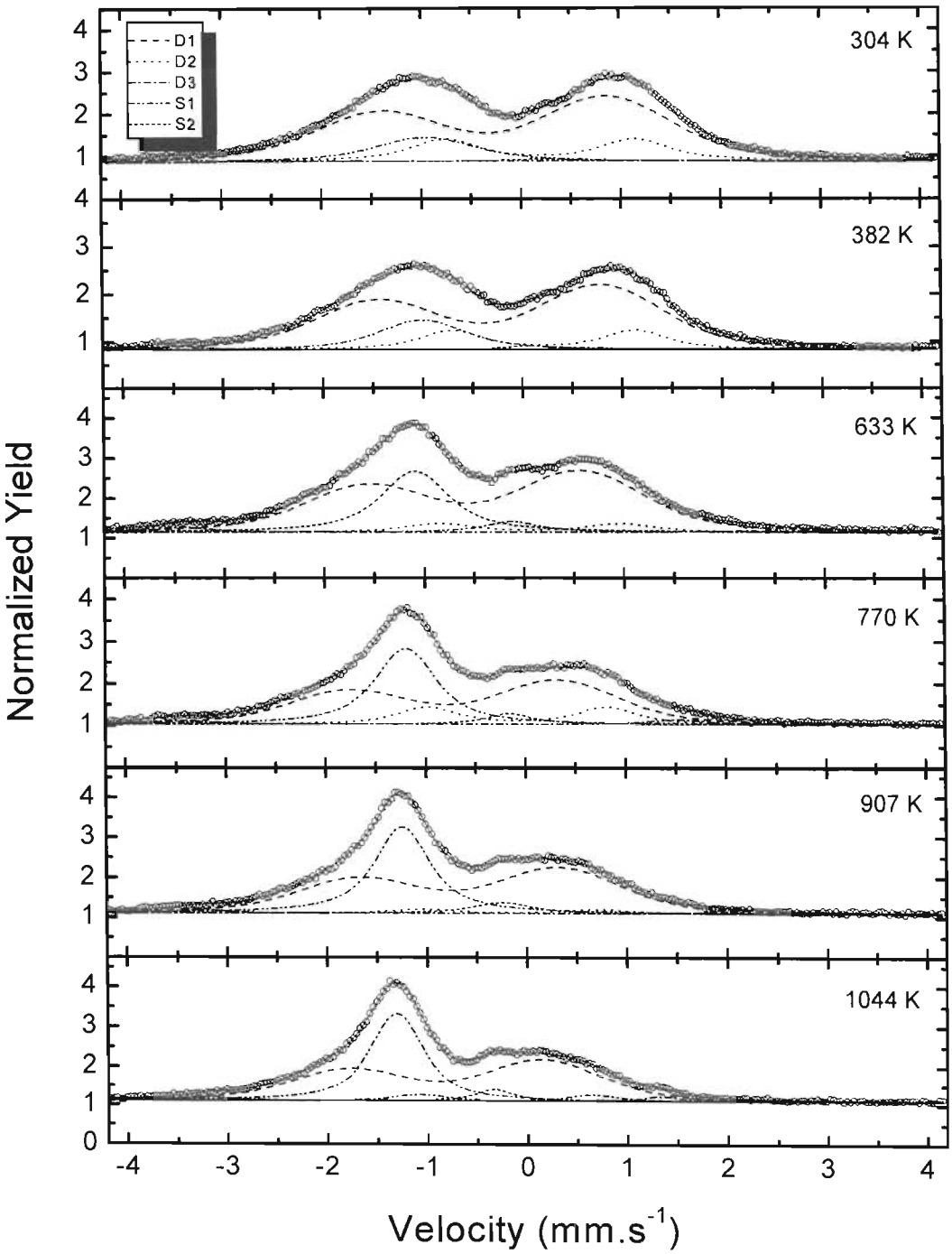

Figure 4.6: **^{57}Fe Mössbauer spectra obtained after ^{57}Mn implantation into Type IIa diamond.**

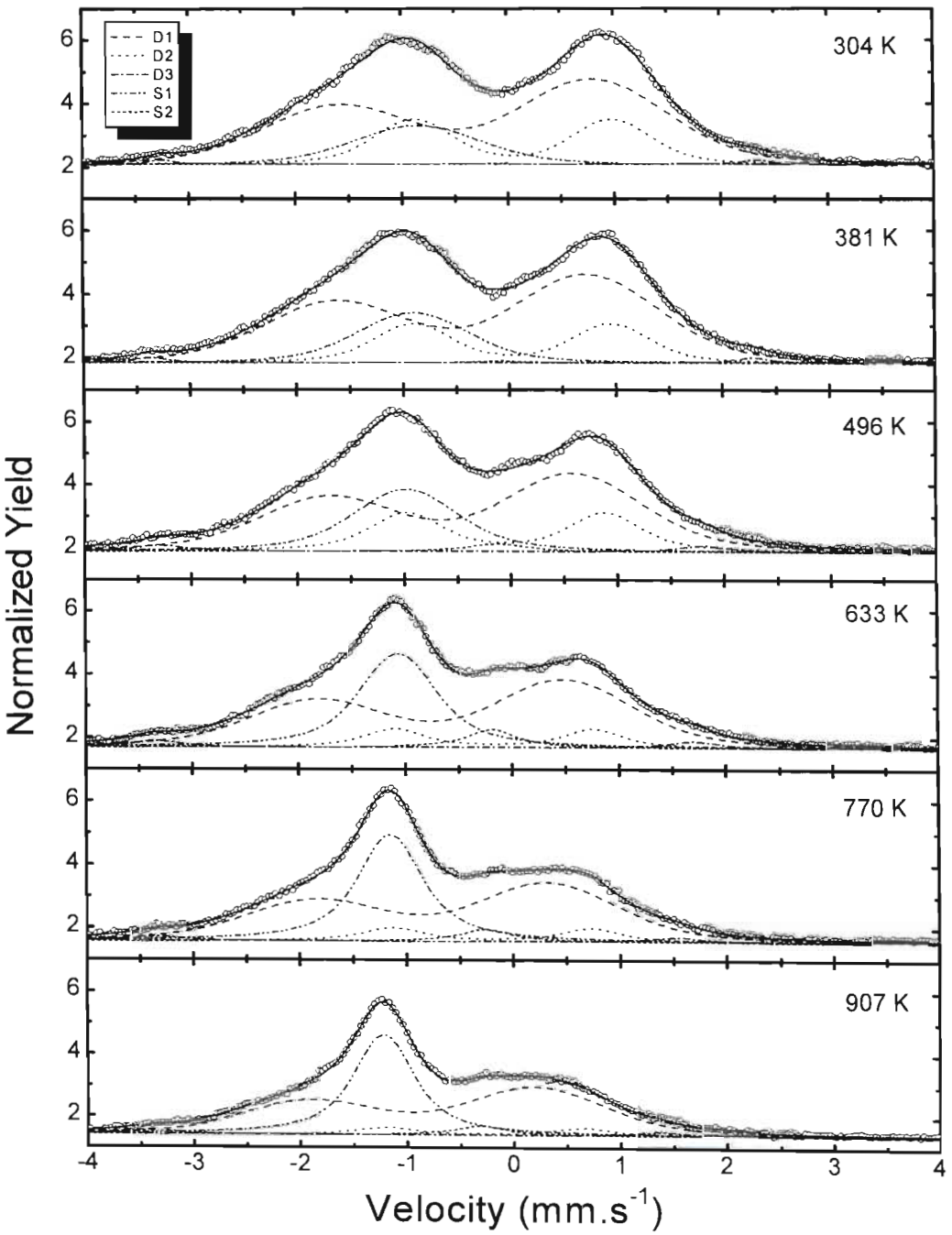

Figure 4.7: **^{57}Fe Mössbauer spectra obtained after ^{57}Mn implantation into CVD diamond.**

The isomer shift of the S1 component for Type IIa and CVD diamond samples were determined as -0.95 and -0.85 mm/s, respectively which is consistent with the values obtained in the CEMS measurements for CVD and HTHP diamond. These values are also in agreement with those obtained in the IBMS measurements[65] and with the experimental values obtained by de Waard and co-workers [25,26-30,71]. The corresponding isomer shifts of S2 for the present measurements were extracted as 0.17 and -0.02 mm/s which is in reasonable agreement with the current CEMS data and previous measurements[25,28-30,71,74]. The inclusion of doublet D3 in the analysis produced consistent and better fits throughout the temperature range and was fitted to the wings of the resonance spectra. The isomer shifts of D1 were determined as -0.34 mm/s and -0.46 mm/s, for Type IIa and CVD diamond, respectively and their corresponding quadrupole splittings were determined as 5.98(5) and 5.59(5) mm/s. The quadrupole splitting of these components decreases with increasing implantation temperature. A similar feature has been observed in the IBMS experiments with directly implanted ^{57}Fe[74]. Table 4.2 gives a summary of the results for all spectral components.

Table 4:2: Hyperfine parameters obtained after ^{57}Mn implantation into Type IIa and CVD diamond.

Comp.	Type IIa		CVD		Linewidths
	δ (mm/s)	ΔE_Q (mm/s)	δ (mm/s)	ΔE_Q (mm/s)	Γ (HWHM) mm/s
S1	-0.95(5)	-	-0.85(5)	-	0.32
S2	+0.17(5)	-	-0.02(5)	-	0.24
D1	-0.27(5)	2.26(5)	+0.05(5)	1.87(5)	0.48
D2	+0.23(5)	1.87(5)	+0.39(5)	2.39(5)	0.16
D3	-0.34(5)	5.98(5)	-0.46(5)	5.59(5)	0.10

Figure 4.8 shows the isomer shifts of D1, D2, S1 and S2 as a function of implantation temperature for Type IIa and CVD diamond samples. The isomer shifts of these spectral components all follow the usual second order Doppler shift variation versus temperature. Table 4.3 shows a summary of the thermal shift values $\left(\frac{\partial \delta}{\partial T}\right)$ for both Type IIa and CVD diamond. Previously Sawicka *et al.*[25] determined the values for $\frac{\partial \delta}{\partial T}$ for a single line in HS sites, same as S1 in this experiment and a quadrupole-split doublet in LS sites as $-(5.2 \pm 0.3)\times 10^{-4}$ and $-(7.0 \pm 0.5)\times 10^{-4}$ mm s^{-1} K^{-1}, respectively in the temperature range 300 to 1100 K. These values are in good agreement with the values presented in this thesis and are shown in Table 4.3.

Table 4:3: Temperature dependence of isomer shift of spectral components for Type IIa and CVD diamond.

Comp.	Type IIa	CVD
	$\frac{\partial \delta}{\partial T}$ (mm s^{-1} K^{-1})	$\frac{\partial \delta}{\partial T}$ (mm s^{-1} K^{-1})
D1	$-7.5(5)\times 10^{-4}$	$-9.9(2)\times 10^{-4}$
D2	$-6.4(4)\times 10^{-4}$	$-5.6(5)\times 10^{-4}$
S1	$-4.9(3)\times 10^{-4}$	$-5.2(2)\times 10^{-4}$
S2	$-6.4(5)\times 10^{-4}$	$-4.8(2)\times 10^{-4}$

The effective Debye temperatures extrapolated from the above results for the HS and LS sites are of the order of 780(50) K and 690(80) K, respectively.

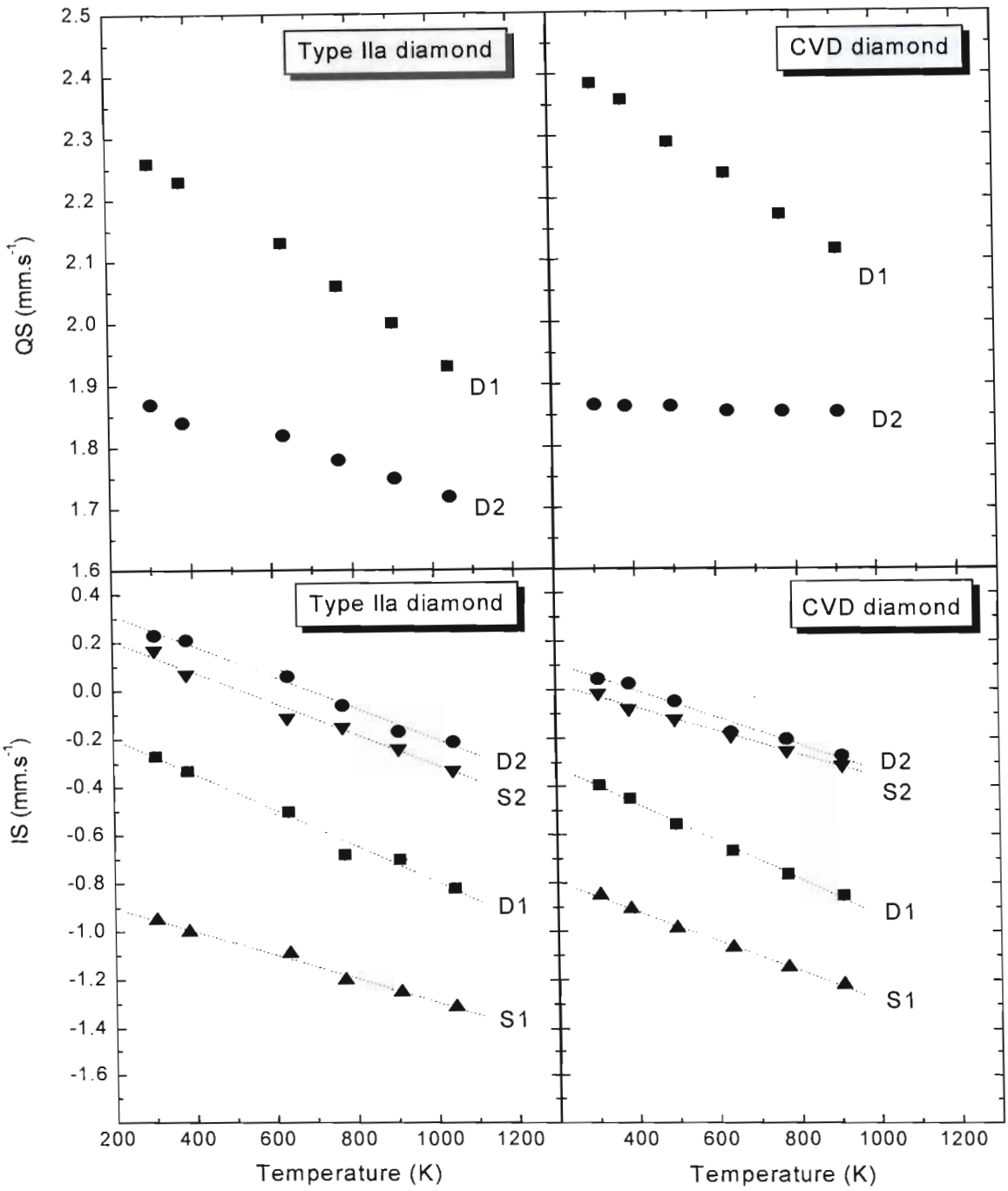

Figure 4.8: **Temperature dependence of isomer shifts and quadrupole splittings, observed in the Mössbauer spectra for Type IIa and CVD diamond amples after ^{57}Mn implantation.**

The theoretical Debye temperature value for diamond is calculated using the mass-corrected value of the Debye temperature $\theta_D^{'}$ for an impurity atom; in this case ^{57}Fe located in a diamond matrix characterized by the Debye temperature θ_D and is given by:

$$\theta_D^{'} = \theta_D \sqrt{\frac{m_C \gamma_{Fe}}{m_{Fe} \gamma_C}}$$

where m_C and m_{Fe} are the masses of the atoms in diamond matrix and mass of impurity atoms, respectively and γ_{Fe} and γ_C are the force constants which are the interaction between C atoms and the interaction between the Fe and C atoms in the diamond matrix, respectively. If we assume that the Fe-C and C-C force constants are approximately equal then the Debye temperature for the substitutional Fe is given by:

$$\theta_D^{'} \approx \theta_D \sqrt{\frac{m_C}{m_{Fe}}}$$

If we consider the Debye temperature for diamond, θ_D to be 1900 K and substitute in the above equation, we find that $\theta_D^{'} \approx 872$ K for the high symmetry site (S1- substitutional site) which is in good agreement with the value obtained from our experimental temperature dependence. Further, these the values compare favourably with the effective Debye temperatures of 800(50) and 450(5) K obtained by Sawicka *et al.*[25] for HS and LS sites, respectively. The strong covalent bonds between carbon atoms in diamond enable them to vibrate with extremely small amplitudes and very high frequencies that result in large Debye temperature values.

The spectral area of the D3 component, not shown in Figure 4.9, is fairly small < 2.5% throughout the implantation temperature range and is discussed again in chapter five. The quadrupole splittings of D1 and D2 for Type IIa and CVD diamond samples illustrated in

Figure 4.8 demonstrates a small change over the temperature range studied. The quadrupole splittings for D1 decreases by 8% and 11% between 300 K and 1044 K for the Type IIa and CVD diamond samples, respectively and the corresponding quadrupole splittings for D2 changes by only 8% and 2%, respectively. These small changes in quadrupole splitting with temperature are indicative that the electric field gradient at the Fe nuclei at LS sites remains practically unchanged. For Type IIa diamond, the electric field gradients at low symmetry sites were determined as $V_{ZZ} = 1.03 \times 10^{18}$ V/cm^2 and 0.86×10^{18} V/cm^2 for doublets D1 and D2, respectively and their corresponding values for CVD diamond were extracted as 0.86×10^{18} V/cm^2 and 1.08×10^{18} V/cm^2. These values are in good agreement with the value of 1.2×10^{18} V/cm^2 obtained by Sawicki *et al.*[28] and are very large in comparison with those for Fe impurities in other solid materials and indicates that the EFG at LS sites in diamond results from the distribution of nearest carbon neighbours.

The intensities of the spectral components for Type IIa and CVD diamond samples plotted against implantation temperature are shown in Figure 4.9. The intensities of the doublets are presented as a combined defect component (D1+D2). The intensity of all spectral components shows similar behaviour for both Type IIa and CVD diamond. The total damage site shows clear annealing, its intensity decreases from 86(5)% at room temperature to 58(4)% at the highest temperature of 1044 K. The intensity of the spectral line S1 increases from 12(3)% at room temperature to approximately 31(3)% at 1044 K. The increased contribution of this line with increasing temperature indicates a transition of a fraction of Fe atoms from LS sites to HS sites due to the gradual healing of disordered bonds between C atoms and thus the recovery of the regular lattice structure in the neighbourhood of Fe atoms. The intensity of line S2, shows negligible increase from 1(1)% to 5(1)% between the lowest and highest temperatures.

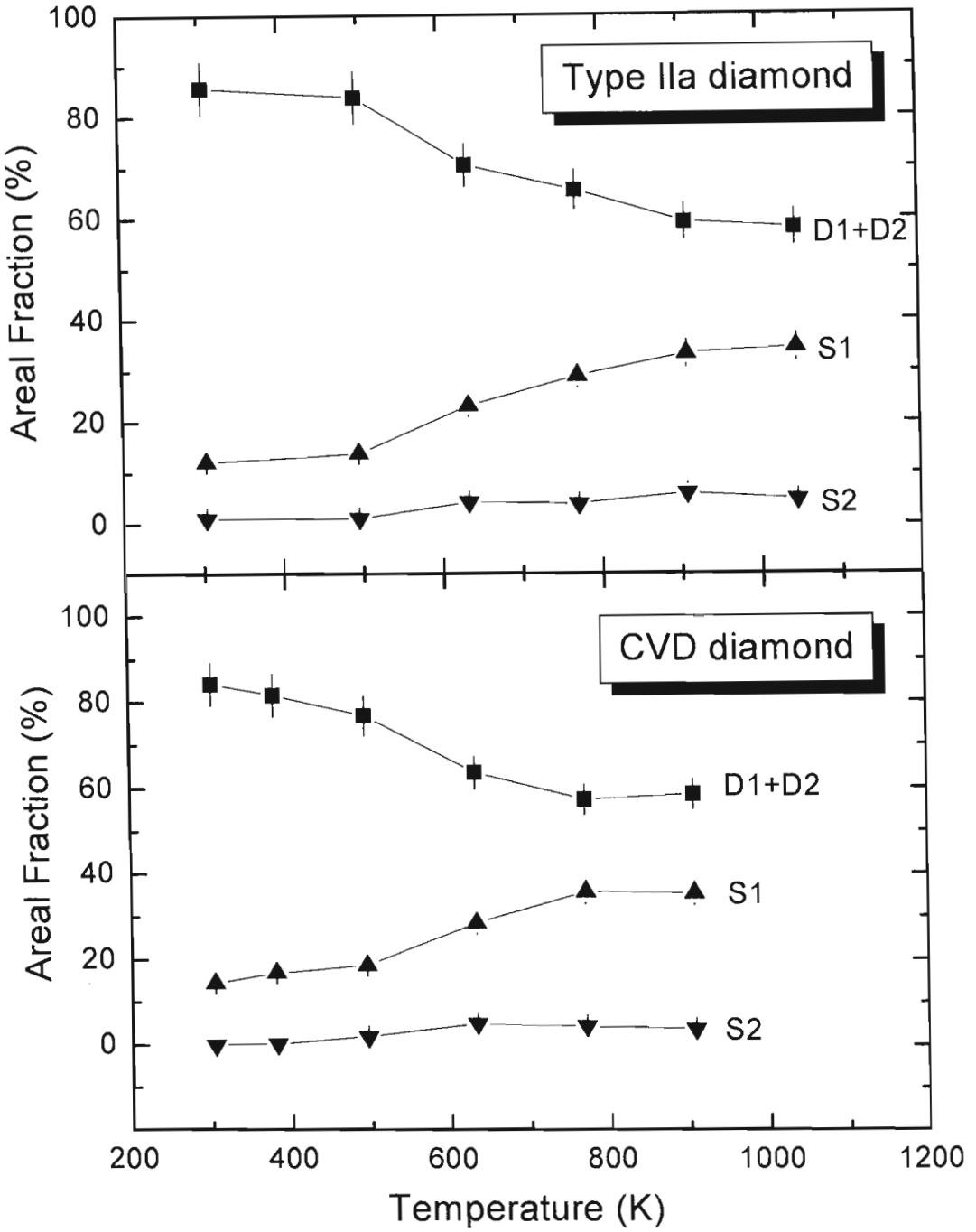

Figure 4.9: **Areal fraction of components as a function of implantation temperature, observed in the Mössbauer spectra for Type IIa and CVD diamond samples after ^{57}Mn implantation.**

4.3 Mössbauer Spectroscopy measurements following ^{57}Mn implantation in Si_{1-x} Ge_x and Ge single crystals

Figures 4.10-4.18 show a series of Mössbauer spectra displayed as sextets (see Chapter 3, Section 3.3.4 for more details) recorded after ^{57}Mn implantation into n-type $Si_{1-x}Ge_x$ (x = 0.017, 0.05 and 0.10), p-type $Si_{1-x}Ge_x$ (x =0.024, 0.083, 0.20 and 0.50) and intrinsic $Si_{1-x}Ge_x$ (x = 0.80 and 1.0) single crystals held at 300-850 K in the implantation chamber described in Section 3.3.3. All components were best analysed using Gaussian broadened Lorentzian lines. The solid line overlapping the experimental data points in Figures 4.10-4.18 indicates the sum of the individual fitting components. In order to show more clearly the evolution of the spectral components with temperature the subspectra of the spectral components and sum at selected temperatures are shown on the right-hand side in these Figures. These subspectra were constructed from the line positions, area fractions, linewidths and quadrupole splittings as determined from the analysis of the corresponding six-fold emission spectra.

At temperatures below 475 K, Gunnlaugsson *et al.*[44,47] fitted the spectra for Si and Si-based materials with three lines corresponding to a quadrupole split doublet assigned to the damage site, an interstitial line and a substitutional line using simultaneous fitting. The spectra presented in this thesis were fitted with four single lines assigned to damage sites (sum of left and right legs), an interstitial line and a substitutional line for temperatures below 475 K. At temperatures above 475 K, our spectra were fitted with three lines corresponding to an interstitial line, a substitutional line and a new line attributed to Fe_i-V complexes similar to their analysis. The linewidth of the interstitial line was set as a free parameter whilst the linewidths assigned to the damage site, substitutional site and Fe_i-V pair were fixed to be the same for the different sample compositions in a temperature series as they were observed not to vary in any systematic way (See Appendix for a detailed explanation of the analysis procedures).

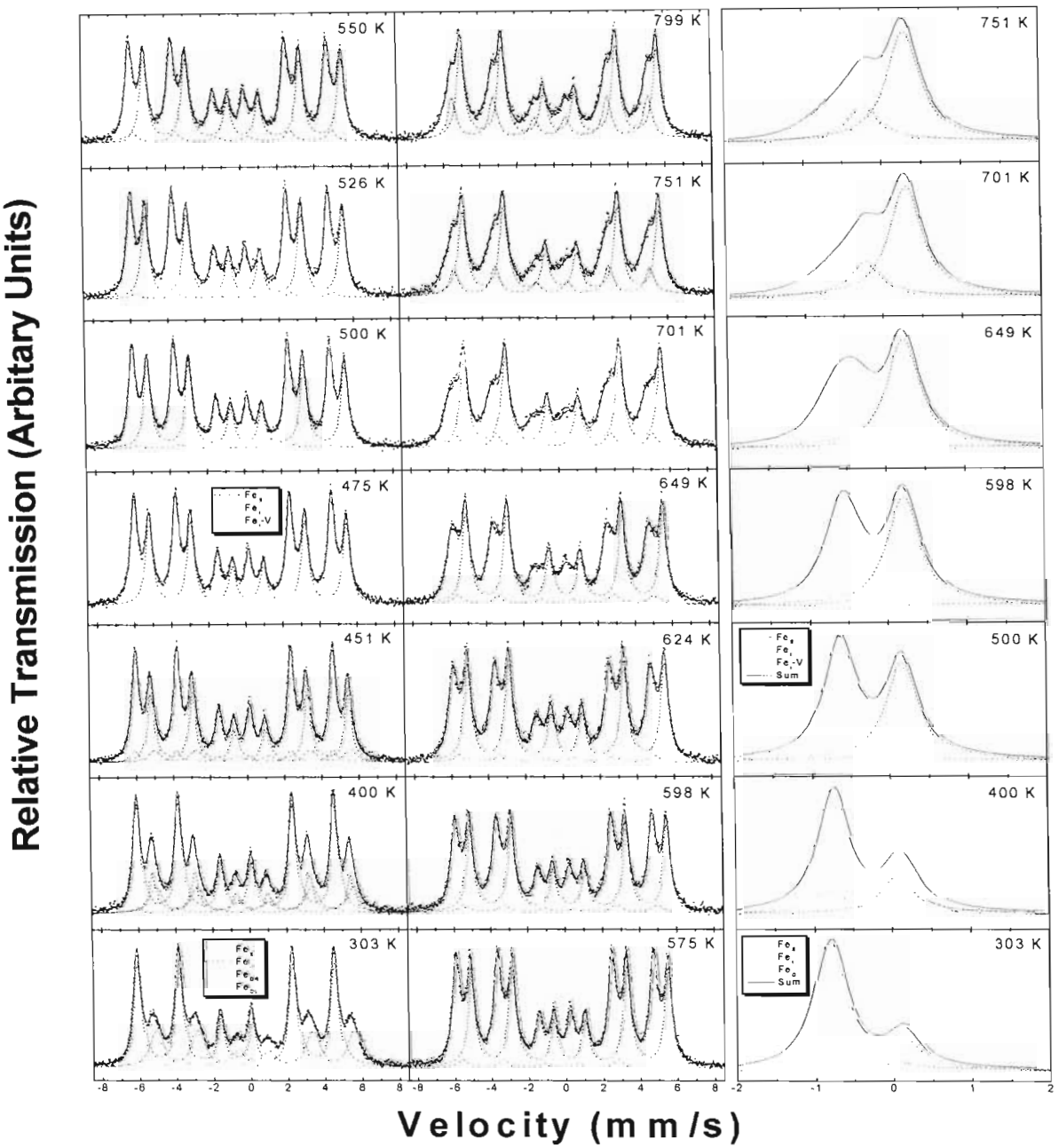

Figure 4.10: **^{57}Fe Mössbauer Spectroscopy spectra measured after implantation of ^{57}Mn into n-type $Si_{0.983}Ge_{0.017}$ single crystal held at the temperatures indicated (shown on left-hand side and middle part). The spectral components required to fit the data, and their sums are shown on the right-hand side at the temperatures indicated.**

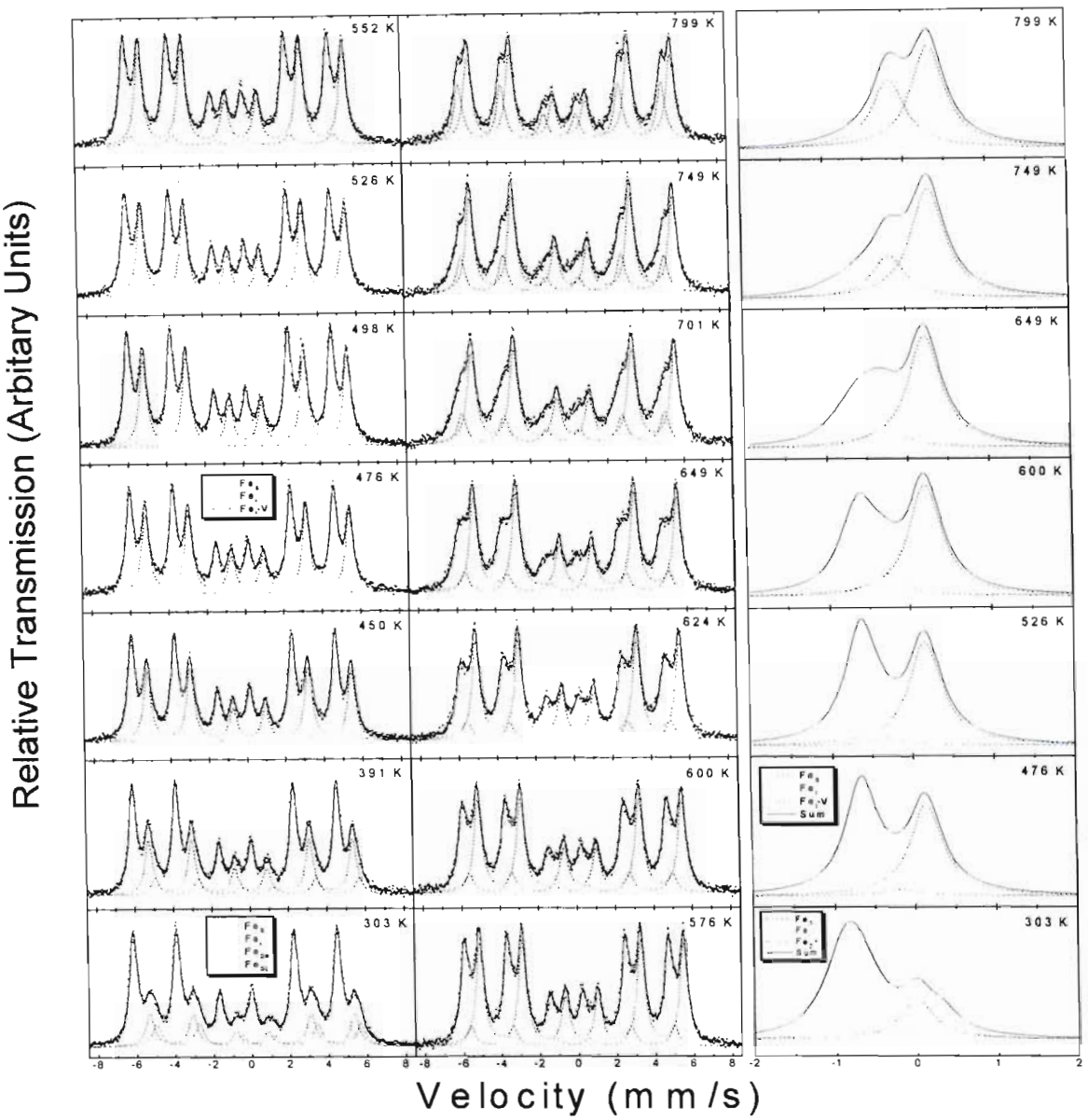

Figure 4.11: **^{57}Fe Mössbauer Spectroscopy spectra measured after implantation of ^{57}Mn into n-type $Si_{0.95}Ge_{0.05}$ single crystal held at the temperatures indicated (shown on left-hand side and middle part). The spectral components required to fit the data, and their sums are shown on the right-hand side at the temperatures indicated.**

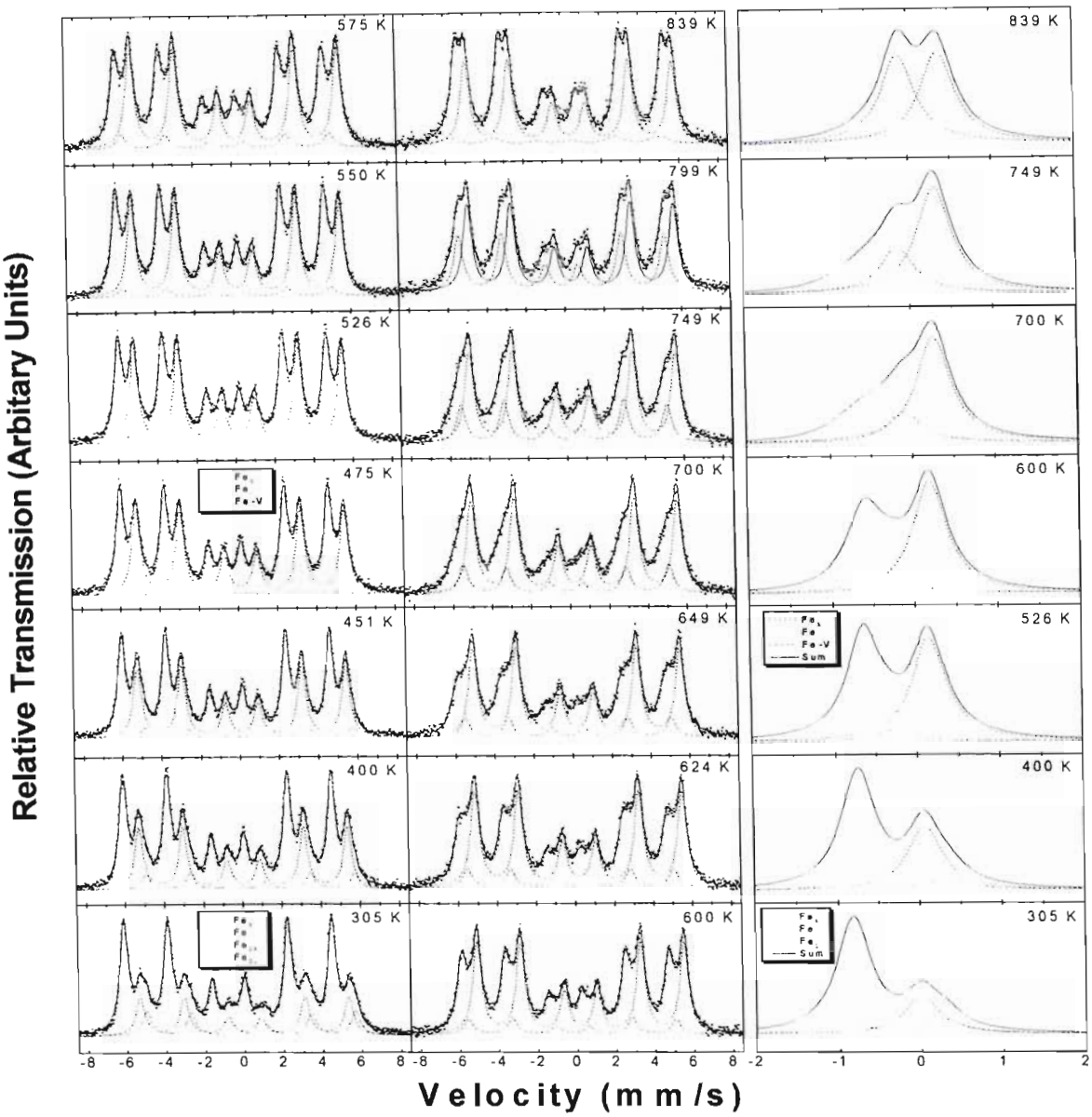

Figure 4.12: **^{57}Fe Mössbauer Spectroscopy spectra measured after implantation of ^{57}Mn into n-type $Si_{0.90}Ge_{0.10}$ single crystal held at the temperatures indicated (shown on left-hand side and middle part). The spectral components required to fit the data, and their sums are shown on the right-hand side at the temperatures indicated.**

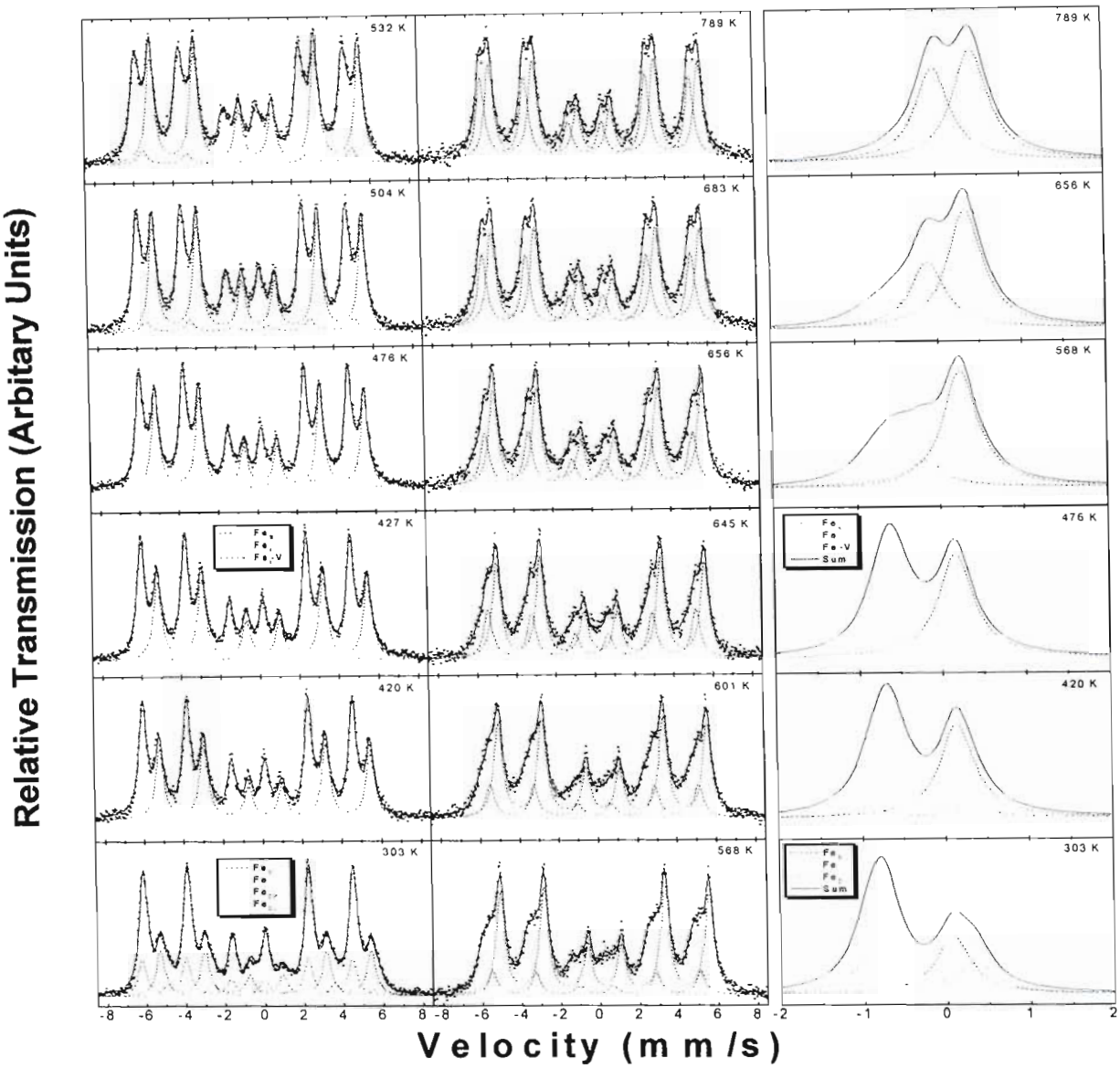

Figure 4.13: **^{57}Fe Mössbauer Spectroscopy spectra measured after implantation of ^{57}Mn into p-type $Si_{0.976}Ge_{0.024}$ single crystal held at the temperatures indicated (shown on left-hand side and middle part). The spectral components required to fit the data, and their sums are shown on the right-hand side at the temperatures indicated.**

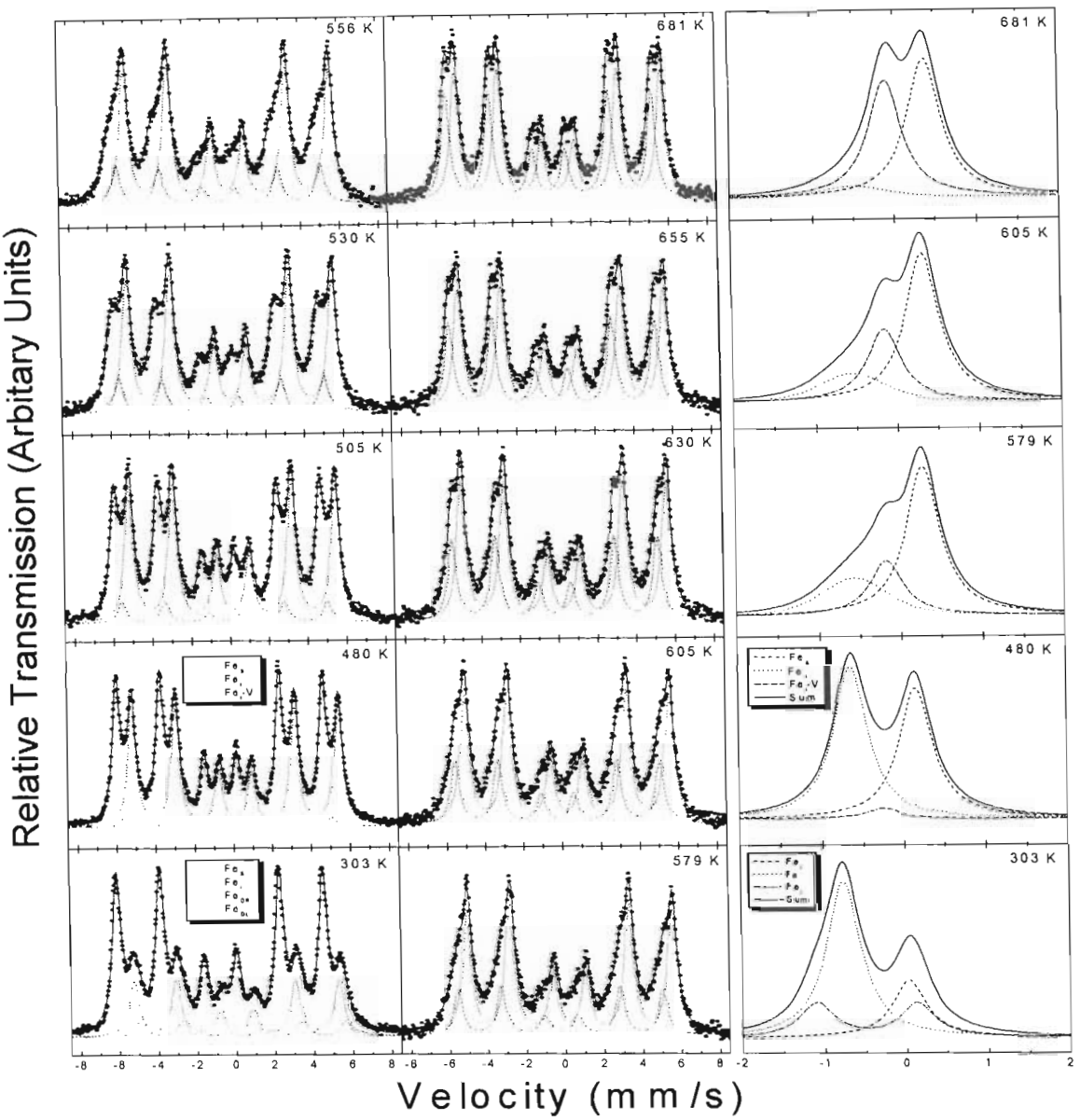

Figure 4.14: **^{57}Fe Mössbauer Spectroscopy spectra measured after implantation of ^{57}Mn into p-type $Si_{0.917}Ge_{0.083}$ single crystal held at the temperatures indicated (shown on left-hand side and middle part). The spectral components required to fit the data, and their sums are shown on the right-hand side at the temperatures indicated.**

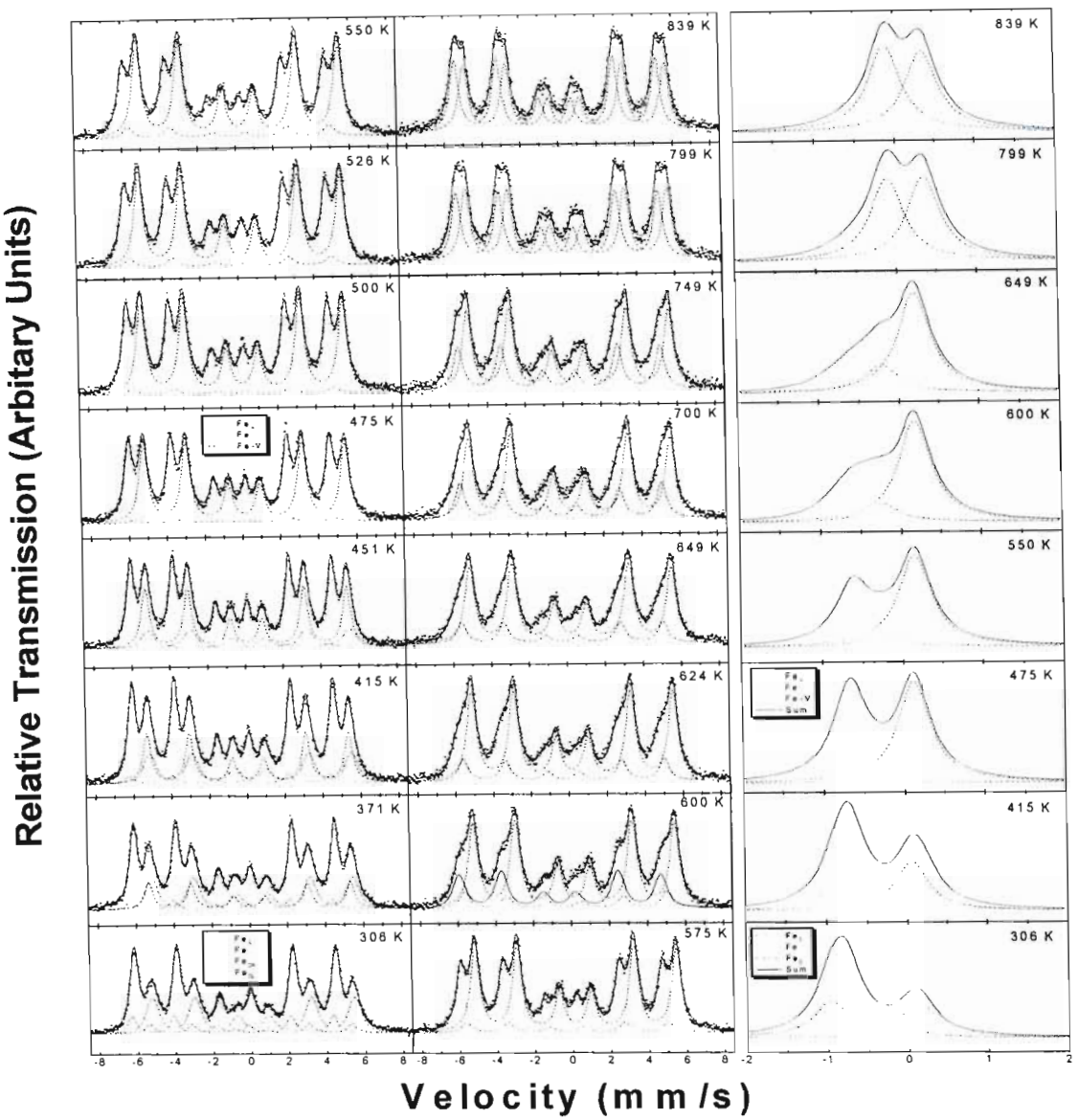

Figure 4.15: **^{57}Fe Mössbauer Spectroscopy spectra measured after implantation of ^{57}Mn into p-type $Si_{0.80}Ge_{0.20}$ single crystal held the temperatures indicated (shown on left-hand side and middle part). The spectral components required to fit the data, and their sums are shown on the right-hand side at the temperatures indicated.**

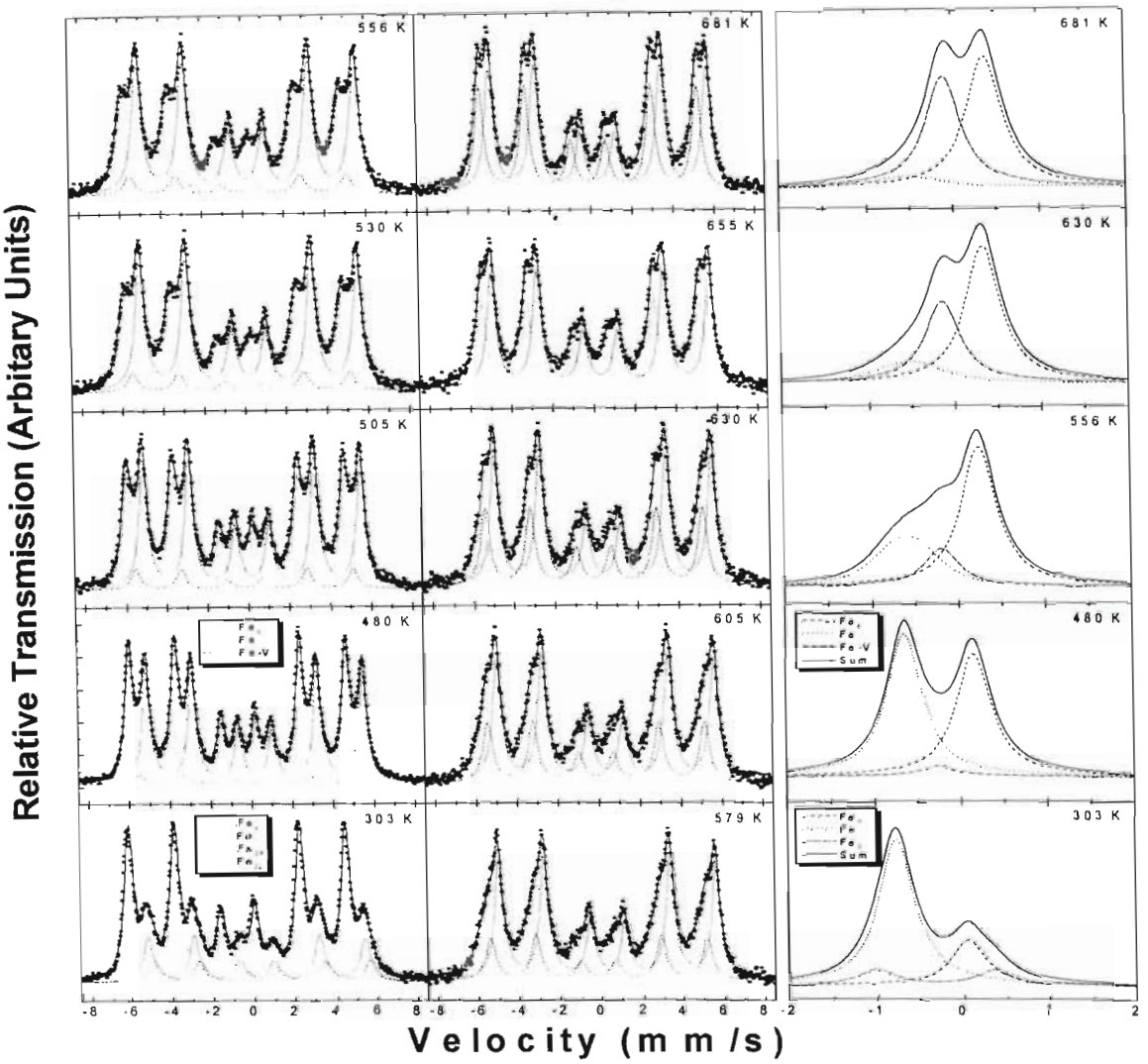

Figure 4.16: **^{57}Fe Mössbauer Spectroscopy spectra measured after implantation of ^{57}Mn into p-type $Si_{0.50}Ge_{0.50}$ single crystal held at the temperatures indicated (shown on left-hand side and middle part). The spectral components required to fit the data, and their sums are shown on the right-hand side at the temperatures indicated.**

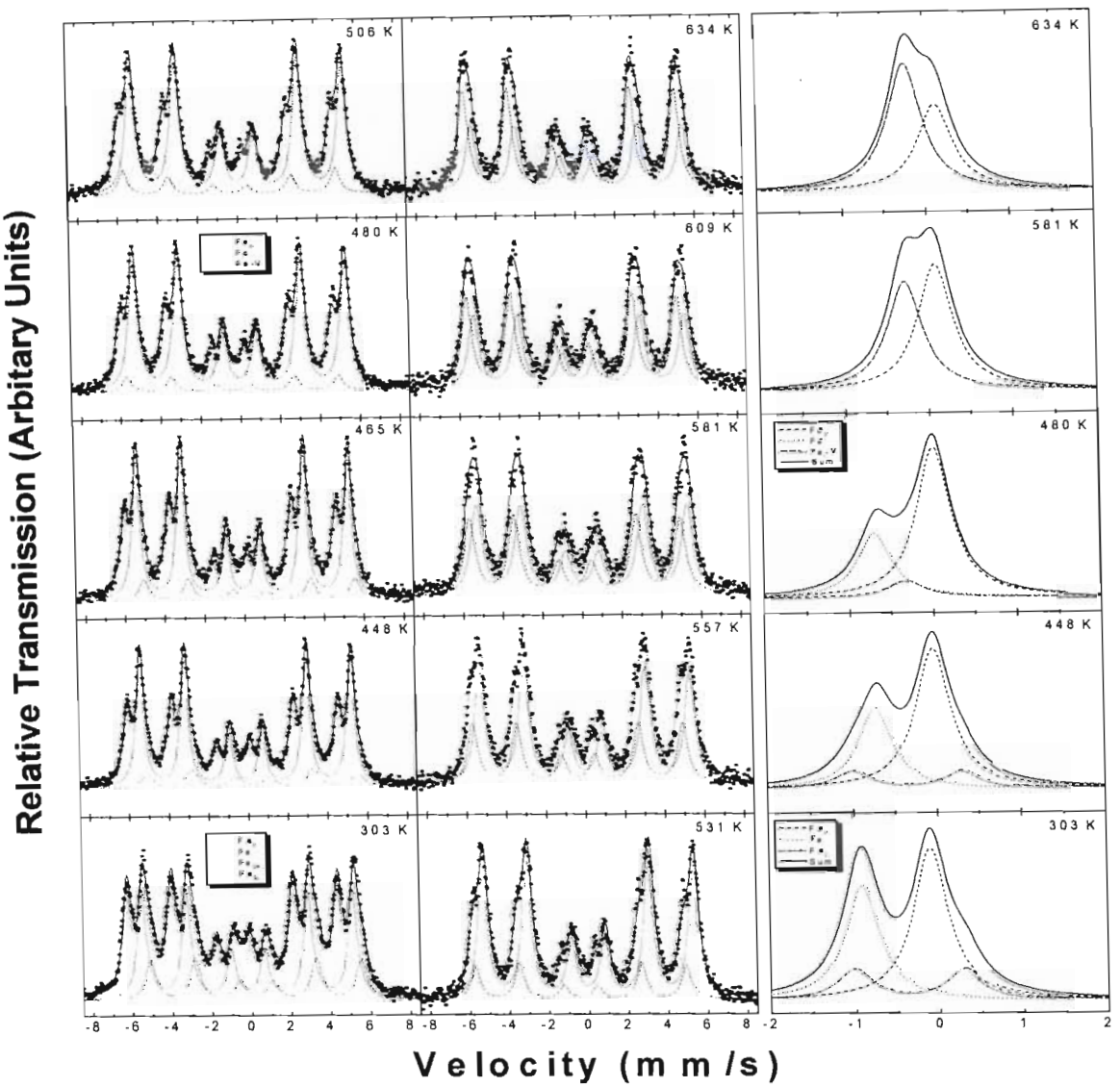

Figure 4.17: **^{57}Fe Mössbauer Spectroscopy spectra measured after implantation of ^{57}Mn into intrinsic $Si_{0.20}Ge_{0.80}$ single crystal held at the temperatures indicated (shown on left-hand side and middle part). The spectral components required to fit the data, and their sums are shown on the right-hand side at the temperatures indicated.**

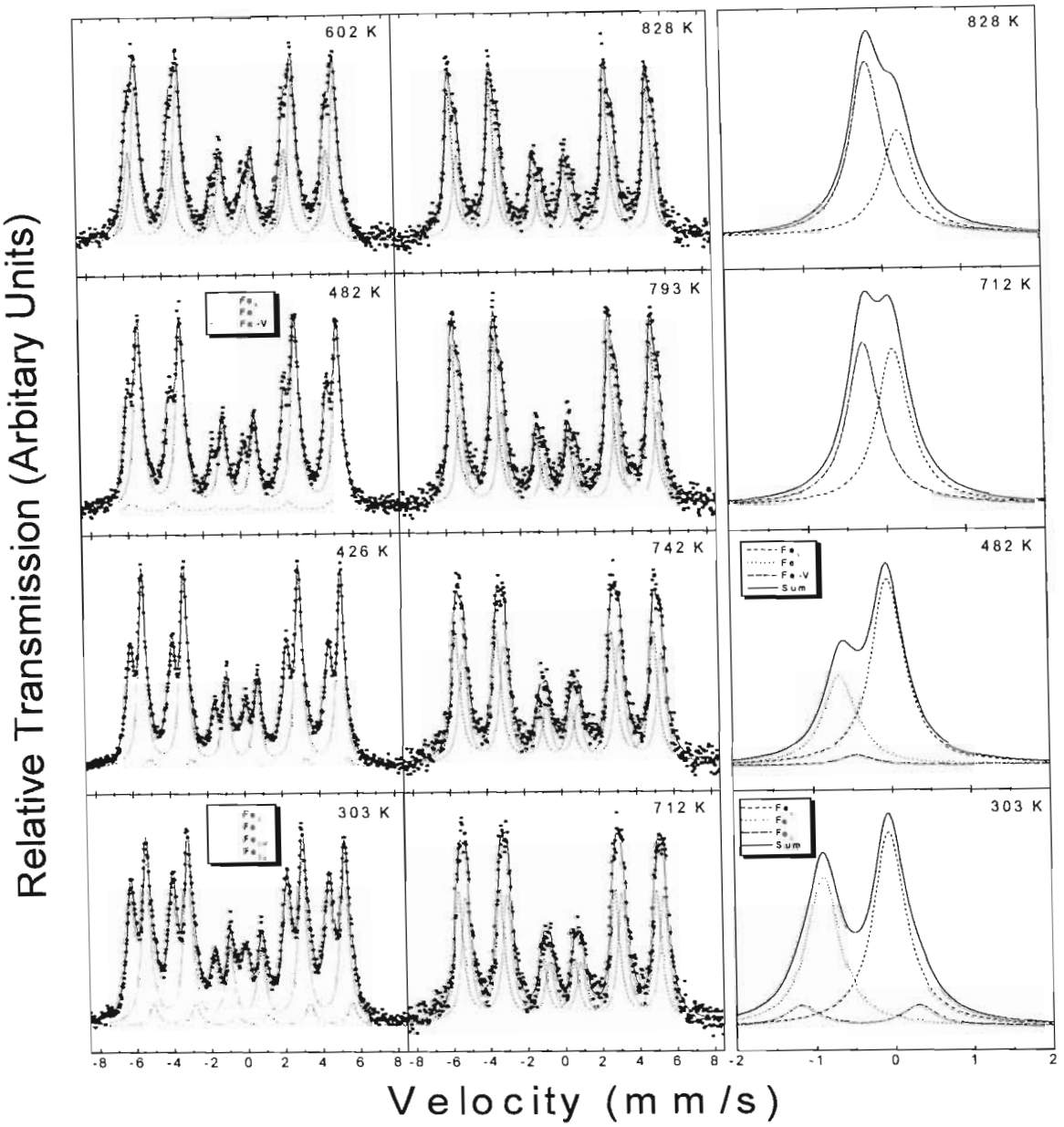

Figure 4.18: **^{57}Fe Mössbauer Spectroscopy spectra measured after implantation of ^{57}Mn into intrinsic Ge (x =1) single crystal held at the temperatures indicated (shown on left-hand side and middle part). The spectral components required to fit the data, and their sums are shown on the right-hand side at the temperatures indicated.**

Several striking features can be seen from these spectra. At room temperature, all spectra are dominated by an asymmetric quadrupole doublet (sum of Fe_{DL} and Fe_{DR}) which is assigned to Fe in implantation related damage sites and lines assigned to the interstitial sites and to a smaller extent the substitutional sites. At closer inspection, the spectra for $0.017 \leq x \leq 0.50$ are very similar at room temperature but for $x \geq 0.80$, the spectral structure changes quite considerably at this temperature. The quadrupole splitting of the doublets for the different material types were determined to be in the region of 1.20(3) mm/s and showed a slight reduction with increasing temperature.

For $0.017 \leq x \leq 0.50$, the spectra are very similar, with the interstitial line present at the highest temperatures of 840 K but is absent for $x = 0.80$ and 1.0 at this temperature. The spectra show clearly that the substitutional line is present at all measured temperatures in all spectra but of varying fractions. The Fe_i-V line, even though in small fractions is consistently visible in all material types at approximately 475 K and becomes pronounced with increasing temperature but shows different effects with increasing higher Ge concentrations ($x \geq 0.80$). For $x = 0.80$, at temperatures > 581 K, and for $x = 1.0$, at temperatures > 482 K, the Fe_i-V line practically disappears from the spectra.

Some of the above observations is based on the following interpretations and whilst other explanations will be given later in terms of diffusion effects. As the temperature is increased, total annealing of the radiation damage from the implantation process is accomplished during the lifetime of the ^{57}Mn (1.5 min) at 475 K prior to the decay and measurement of the ^{57}Fe Mössbauer spectra at this temperature. This annealing process leads to the Mn probe atoms occupying substitutional lattice sites[45] . In the subsequent decay of ^{57}Mn to the Mössbauer state (100 ns) of ^{57}Fe, an average recoil energy of 40 eV is imparted on the daughter nucleus which results to a replacement into tetrahedral interstitial sites[45,47] for the majority of the Fe atoms and balance remains on substitutional sites.

Figure 4.19 shows the selected data for x = 0.017 at the three critical temperatures of 303 K, 476 K and 789 K illustrating the annealing of the damage sites, the evolution of the Fe_i-V pair and the diffusion of the interstitial site. At room temperature, the isomer shift of the interstitial lines for $0.017 \leq x \leq 0.50$ were determined to be in the region of 0.77(5) to 0.81(5) mm/s whilst for $x \geq 0.80$, the isomer value of this line was found to be around 0.90(5) mm/s. The substitutional lines has an isomer shift in the range 0.098(4) to -0.08(4) mm/s whilst the isomer shift of the Fe_i-vacancy pairs at 475 K was measured to be in the vicinity of 0.25(2) to 0.44(2) mm/s. Table 4.4 shows a comparison of the isomer shifts for the substitutional, interstitial and Fe_i-V lines extracted for different material types and sample compositions. The isomer shifts are given relative to an α-Fe absorber.

Table 4.4: Isomer Shifts for substitutional, interstitial and Fe_i-V lines for different material types and sample compositions.

Material Type	Ge Concentration ($Si_{1-x}Ge_x$)	Isomer Shifts (mm/s)		
		Substitutional Line[a]	Interstitial Line[a]	Fe_i-V Line[b]
n-type	x = 0.017	-0.003(4)	0.79(5)	0.44(2)
	x = 0.05	-0.001(4)	0.80(5)	0.39(2)
	x = 0.10	-0.008(4)	0.81(5)	0.37(2)
p-type	x = 0.024	-0.080(4)	0.78(5)	0.24(2)
	x = 0.083	-0.033(4)	0.77(5)	0.25(2)
	x = 0.20	+0.006(4)	0.79(5)	0.34(2)
	x = 0.50	-0.067(4)	0.77(5)	0.25(2)
Intrinsic	x = 0.80	+0.098(4)	0.90(5)	0.33(2)
	x = 1.0	+0.060(4)	0.90(5)	0.44(2)

[a]Obtained at room temperature.

[b]Obtained at $\approx$475 K.

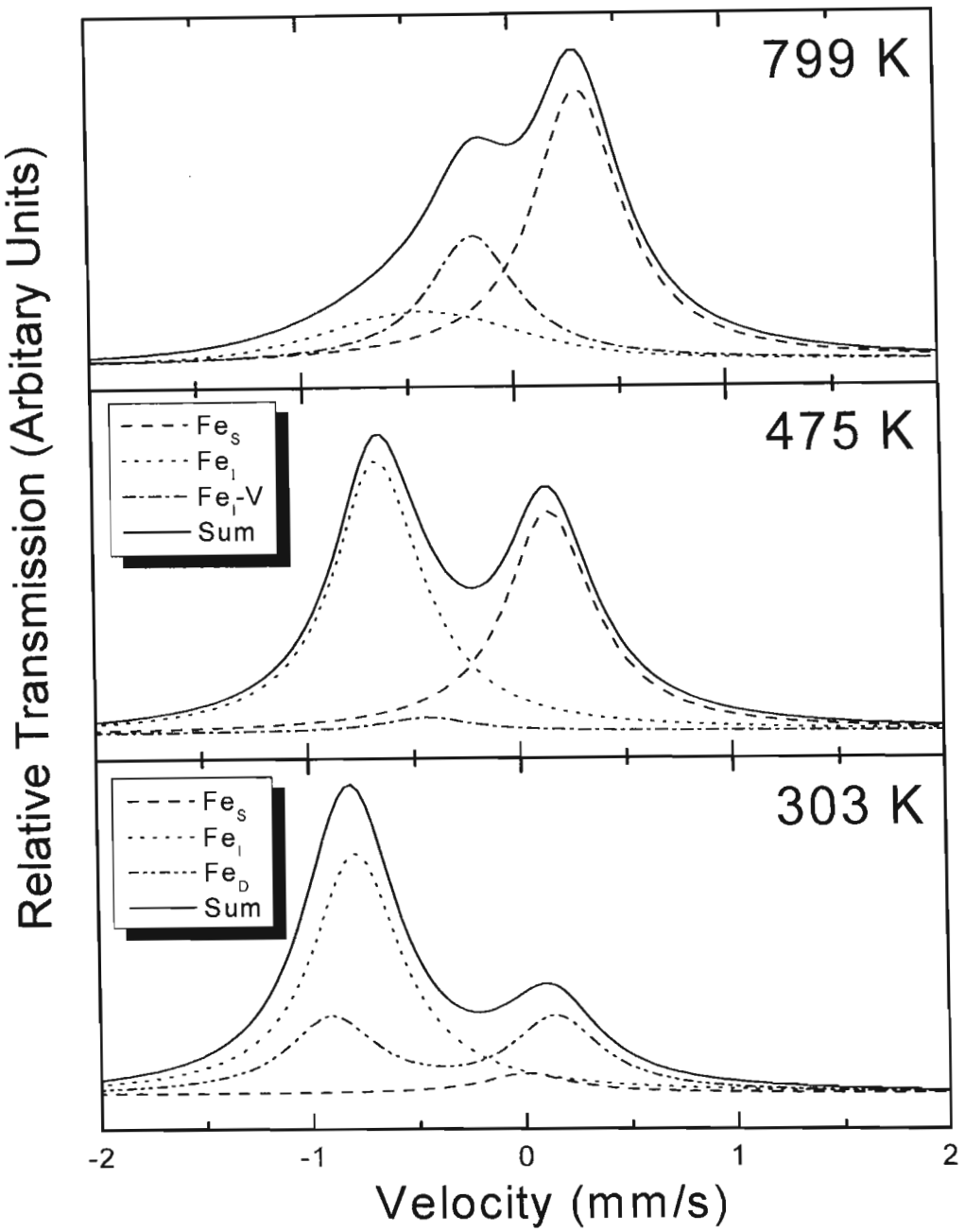

Figure 4.19: Selected ^{57}Fe Mössbauer Spectroscopy spectra measured after implantation of ^{57}Mn into n-type $Si_{0.983}Ge_{0.017}$ single crystal held at the temperatures indicated. The annealing of defects, diffusion of interstitial sites and evolution of Fe_i-V line are clearly visible.

All spectral components show the general movement to the right as expected from the second order Doppler shift and this is illustrated in Figure 4.20 for $Si_{0.983}Ge_{0.017}$ which serves as a representative example due to the large amount of data.

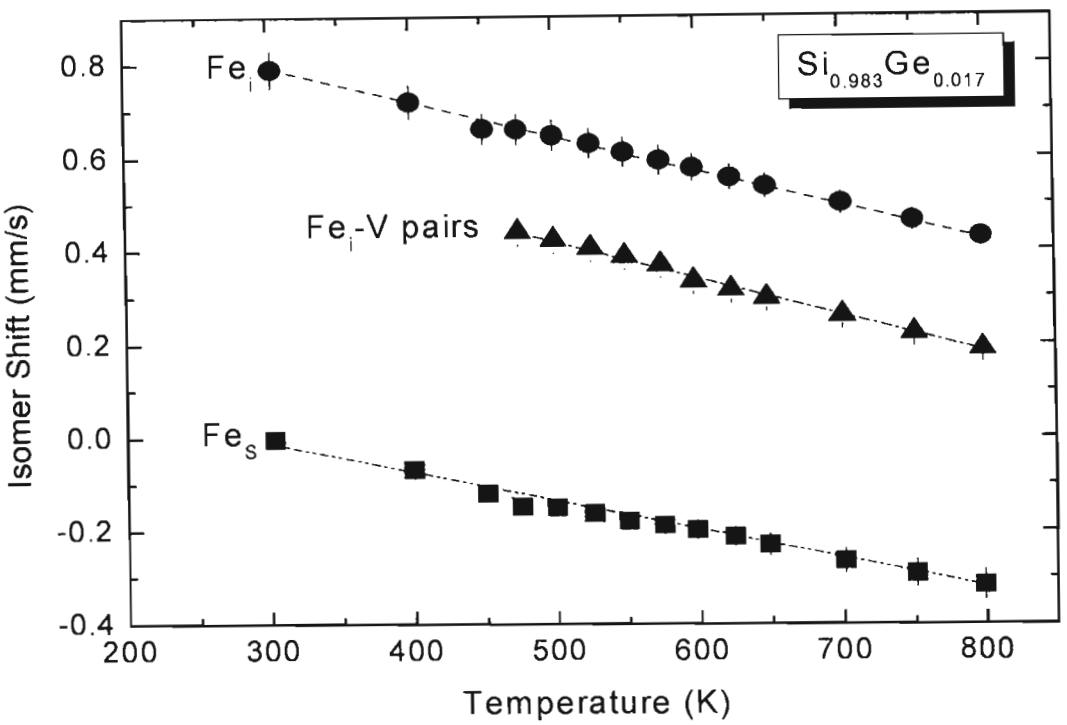

Figure 4.20: Isomer Shift (mm/s) as a function of temperature (K) for $Si_{0.983}Ge_{0.017}$ sample.

The isomer shift of the interstitial line is found to depend on doping which is predicted by theory[76,77] and is associated with the well-known $Fe^{0/+}$ donor level at $E_V + 0.38\,eV$[31]. This is evident if one compares the isomer shift values for n-type ($x = 0.017$), p-type ($x = 0.024$) and intrinsic ($x = 0.80$) samples. As the Ge concentration increases from x = 0.017 to x = 0.50, the isomer shift value changes from 0.79(5) to 0.77(5) mm/s. In the intrinsic material ($x \geq 0.80$), the isomer shift of the interstitial line was found to be in the region of 0.90 mm/s and showed a dramatic variation from the values obtained for the n-type and p-type materials. The isomer shift of the substitutional lines for the n-, p- and

intrinsic type materials were found to be fairly similar. The isomer shift values of the Fe_i-V line for the n-type material (x = 0.017, 0.05 and 0.10) were found to be in the region of 0.37(2) – 0.44 (2) mm/s whilst the isomer shift values for the p-type material (x = 0.024, 0.083, 0.20 and 0.50) were determined in the range 0.25(2) – 0.34(2) mm/s. The isomer shift values for the intrinsic samples were determined to be in the region of 0.33(2) – 0.44 mm/s.

The spectral intensity of the interstitial line for x = 0.017 is approximately 73% at room temperature and is reduced to 44% at the highest temperature of 839 K whilst for x = 0.024 to 0.50, the decrease is much more dramatic from 76% to 14%. The population of this site is completely different for x = 0.8 and 1.0 since at room temperature, the spectral intensity of the interstitial line is only 56% and is reduced to 0% between temperatures of 581 and 650 K. The site population of the spectral components as a function of implantation temperature are shown in Figures 4.21-4.23.

At temperatures above 475 K, the total annealing of the damage related defects leads predominantly to an increase in the substitutional fraction and a new line attributed to Fe_i-V pairs became evident similar to the results obtained for Si by Gunnlaugsson *et al.*[44,47]. The substitutional fraction remains fairly constant for each composition but varied from sample to sample in region of 21-32% at temperatures less than 700 K and then decreased gradually with increasing temperature indicating a decreasing probability of Mn/Fe to remain on or to be incorporated at substitutional sites with increasing temperature. For x = 0.017, the vacancy pair contributes 3% at 475 K but increases to 44% at 799 K as compared to $0.024 \leq x \leq 0.50$ where there is much more significant increase from 1% to 66%. For x = 0.80 and 1.0, these trends are significantly different since at 475 K, the vacancy-pair fraction is approximately 5% and then increases to 85% at the highest temperature of 828 K. For $0.024 \leq x \leq 0.50$, our results clearly show that at higher temperatures, the interstitial fraction decreases quite dramatically due to diffusion and all spectra are dominated by the line assigned to Fe_i-V and the substitutional line.

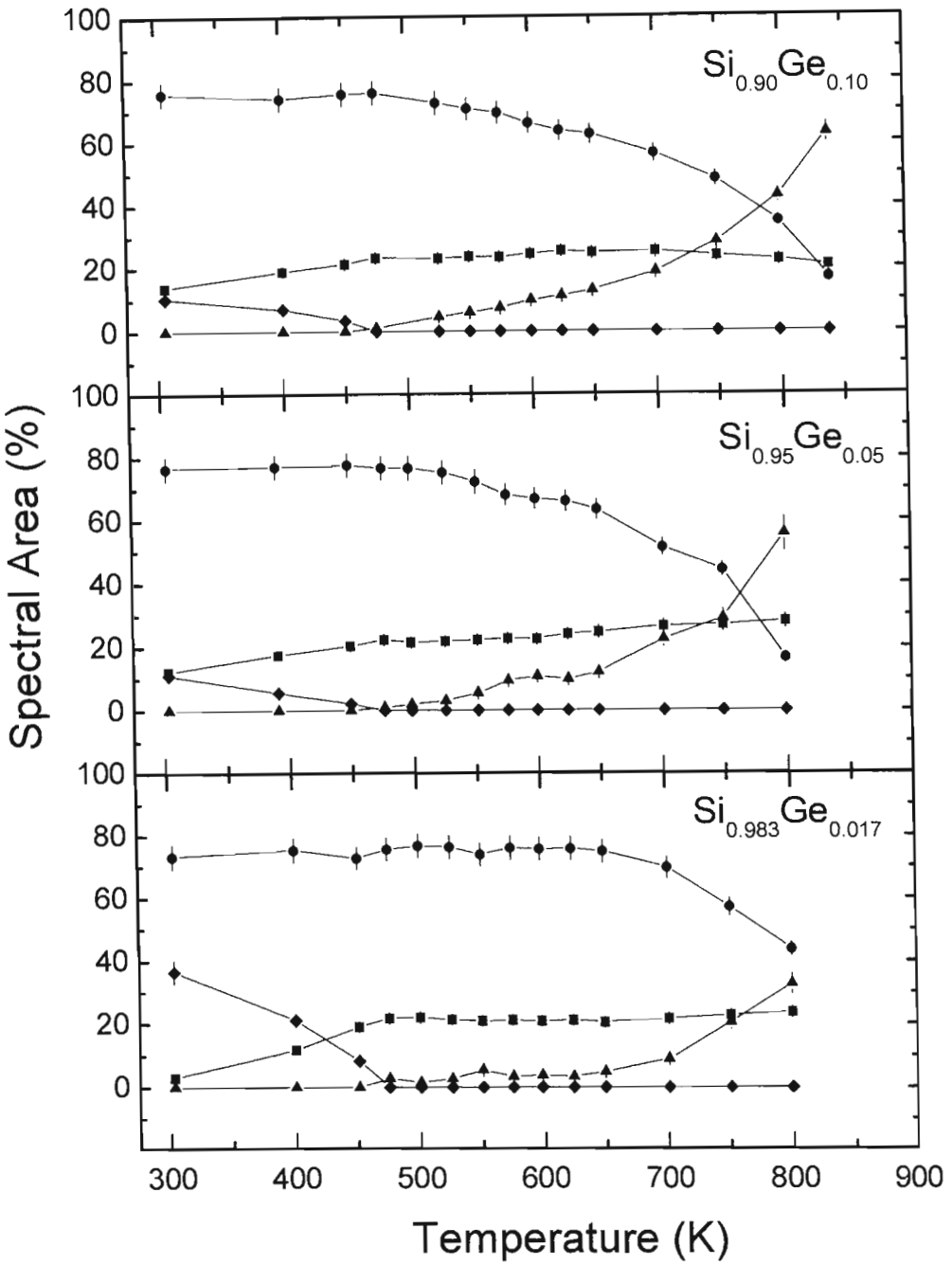

Figure 4.21: Site populations as a function of temperature after ^{57}Mn implantation into n-type $Si_{1-x}Ge_x$ (x = 0.017, 0.05 and 0.10) single crystals where ■ = Fe_s, ● = Fe_i, ▲ = Fe_i-V and ◆ = Total Damage.

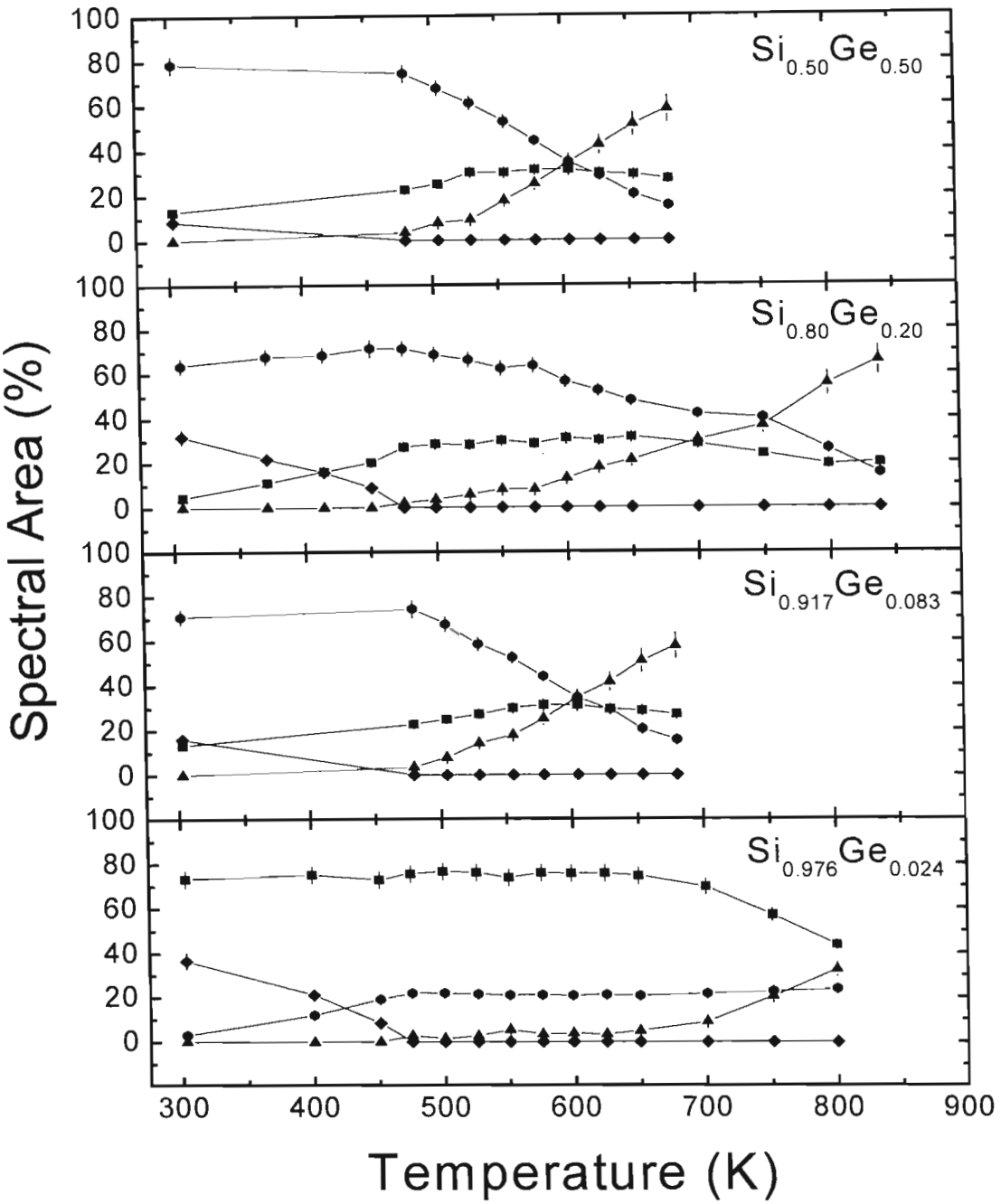

Figure 4.22: Site populations as a function of temperature after ^{57}Mn implantation into p-type Si_{1-x} Ge_x (x = 0.024, 0.083, 0.20 and 0.50) single crystals where ■ = Fe_s, ● = Fe_i, ▲ = Fe_i-V and ◆ = Total Damage.

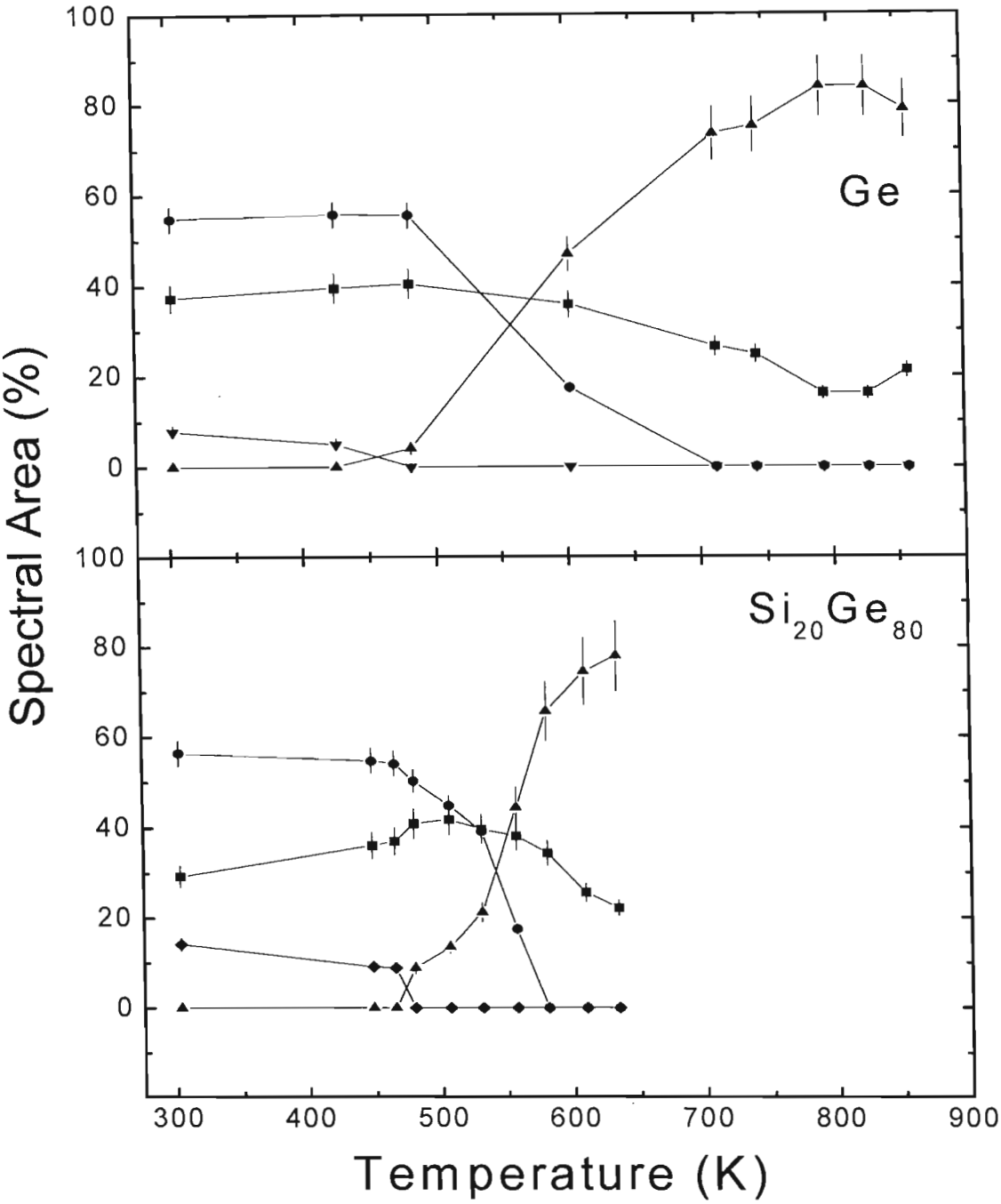

Figure 4.23: Site populations as a function of temperature after ^{57}Mn implantation into intrinsic $Si_{1-x}Ge_x$ (x = 0.80 and 1.0) single crystals ■ = Fe_s, ● = Fe_i, ▲ = Fe_i-V and ◆ = Total Damage.

The Fe_i-V pairs by comparison for x = 0.80 and 1.0 is strongly populated at temperatures ≥ 530 K due to the lower intensity of the interstitial line which allows for the more accurate study of the temperature behaviour of the Fe_i-V complexes as compared to silicon[44,47]. The Fe_i-V pairs are created in the recoil event within the lifetime of the ^{57}Fe Mössbauer (100 ns) and are stable upto ≈ 830 K. For $x = 0.80$, the Fe_i component has completely disappeared at 581 K whereas for $x = 1.0$, this component was not evident at 712 K due to diffusion effects. At 602 K, the Fe_i component was still present, 14% spectral intensity but could have disappeared completely in the vicinity of 602 to 712 K.

From the results presented thus far, one can conclude that the spectral features for $0.017 \leq x \leq 0.50$ $Si_{1-x}Ge_x$ shows very similar resemblance to silicon[44,47] whilst the spectral features for $x = 0.80$ is comparable to Ge[48]. The Debye temperatures for the lines assigned to substitutional Fe (Fe_S), interstitial Fe (Fe_i), the damage site (Fe_D) and the Fe-vacany pair (Fe_i-V) are given in Table 4.5 for different sample compositions. The Debye temperatures were extracted from the line areas of the different spectral components and were obtained for $0.017 \leq x \leq 0.50$ and $x \geq 0.80$. For $0.017 \leq x \leq 0.50$, the measured Debye temperature value of 400(60) K for substitutional site compares well with the theoretical value of 460 K for Si determined by the mass defect approximation[45]. For $x \geq 0.80$, the Debye temperature for substitutional site was found to be 350(50) K and is accordance with the value of 407 K determined by this model. The results show that as the Ge concentration (x) increases, the Debye temperatures for the different spectral components become significantly smaller. Unfortunately, due to the errors associated with determining line areas, it is difficult to establish a relationship between the Debye temperatures and varying Ge concentrations ranging from x = 0.017 to 1.0 in a systematic way with precise accuracy but the results are presented in categories i.e. $0 < x \leq 0.50$ and $x \geq 0.80$ which resembles elemental Si and Ge, respectively. The high Debye temperature (380-400 K) of the damage site is not compatible with an interstitial location[45] due to its lower Debye temperature (180-200 K) but is similar to that of the substitutional Fe in crystalline Si which is approximately 460 K based on a simple mass defect model. The higher isomer shift (lower

electron density) as compared to the substitutional site and large quadrupole splitting for the damage site implies that the damage site location is a highly distorted (or amorphous) zone with four nearest neighbour Si atoms.

Table 4.5: Debye temperatures of spectral components for different sample compositions.

Spectral component	Debye Temperature (K)	
	$0 < x \leq 0.50$	$x \geq 0.80$
Fe_S	400(60)	350(50)
Fe_i	200(60)	180(50)
Fe_D	400(60)	380(50)
Fe_i-V	200(60)	190(50)

Figure 4.24 shows a comparison of ^{57}Fe Mössbauer Spectroscopy spectra measured after implantation of ^{57}Mn into n-type $Si_{0.983}Ge_{0.017}$, p-type $Si_{0.976}Ge_{0.024}$ and intrinsic Ge single crystals at the three critical temperatures where significant spectral changes occur. The interstitial line is visible at $\approx$598 K in x = 0.017 to x = 0.024 and is still present at the highest measured temperature of 789 K as seen earlier whereas for x = 1.0 at $\approx$602 K, the interstitial line has disappeared completely from the spectra. Therefore, one can conclude that diffusion of the interstitial Fe occurs much faster for $x \geq 0.80$ as compared to $0.017 \leq x \leq 0.50$. As temperature increases beyond 475 K, the interstitial line broadens which is consistent with the properties associated with the diffusion of interstitial Fe[47]. At this stage, it is difficult to make any immediate conclusions regarding the line broadening of the interstitial lines for the n- and p-type material from the spectra due to the low intensity of the line assigned to Fe_i-V pairs. Further, this line restricts an accurate determination of the line broadening of the interstitial line; however application of consistent fitting methods, reasonably accurate values can be obtained in the temperature range 450-650 K.

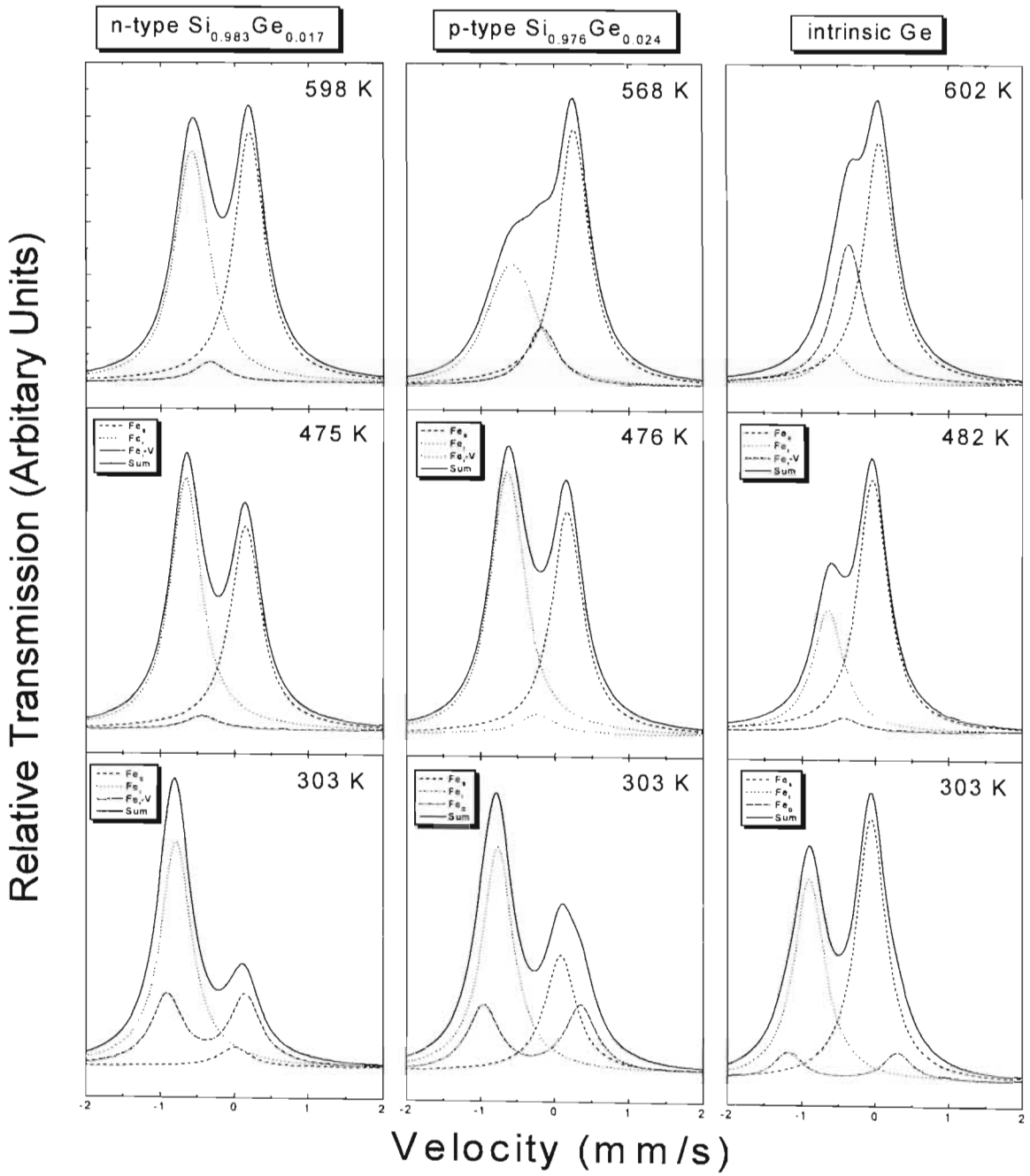

Figure 4.24: **Comparison of ^{57}Fe Mössbauer Spectroscopy spectra measured after implantation of ^{57}Mn into n-type $Si_{0.983}Ge_{0.017}$, p-type $Si_{0.976}Ge_{0.024}$ and intrinsic Ge single crystals held at the temperatures indicated.**

4.3.1 Line Broadening and Activation Energies

The relationship between the linewidth of the interstitial line, Γ, and the interstitial diffusion coefficient, D, is given by[78]:

$$\Gamma = \Gamma_o + \frac{12\hbar cD}{E_o l^2} \tag{4.1}$$

where

Γ_o is the experimental linewidth given in the units of the Doppler velocity,

$\hbar = h/2\pi$, h is Planck's constant,

c is the speed of light,

E_o is the energy of the Mössbauer transition (14.4 keV), and l is the elementary jump length, 0.235 nm, assuming a direct interstitial mechanism i.e. jumps between tetrahedral interstitial sites.

The diffusion coefficient is given by:

$$D = D_o \exp\left(-E_a/kT\right) \tag{4.2}$$

where D_o is the pre-exponential factor,

k is the Boltzmann's constant

E_a is the activation energy measured in eV and

T is the temperature given in K.

The line broadening, $\Delta\Gamma = \Gamma - \Gamma_o$ of the interstitial site is proportional to the diffusion coefficient D as observed from equation (4.1). Rewriting (4.1) and substituting (4.2) gives:

$$\Delta\Gamma = \Gamma - \Gamma_o = \alpha \exp(-E_a/kT) \tag{4.3}$$

where $\alpha = \frac{12\hbar c D_o}{E_o l^2}$.

A plot of $\ln\Delta\Gamma$ versus 1/T yields a straight line from which the activation energy (E_a) can be determined from slope and the pre-exponential factor (D_o) from the y-intercept.

Figure 4.25 shows a plot of $\ln\Delta\Gamma$ versus 1/T for n- and p-type $Si_{1-x}Ge_x$ samples.

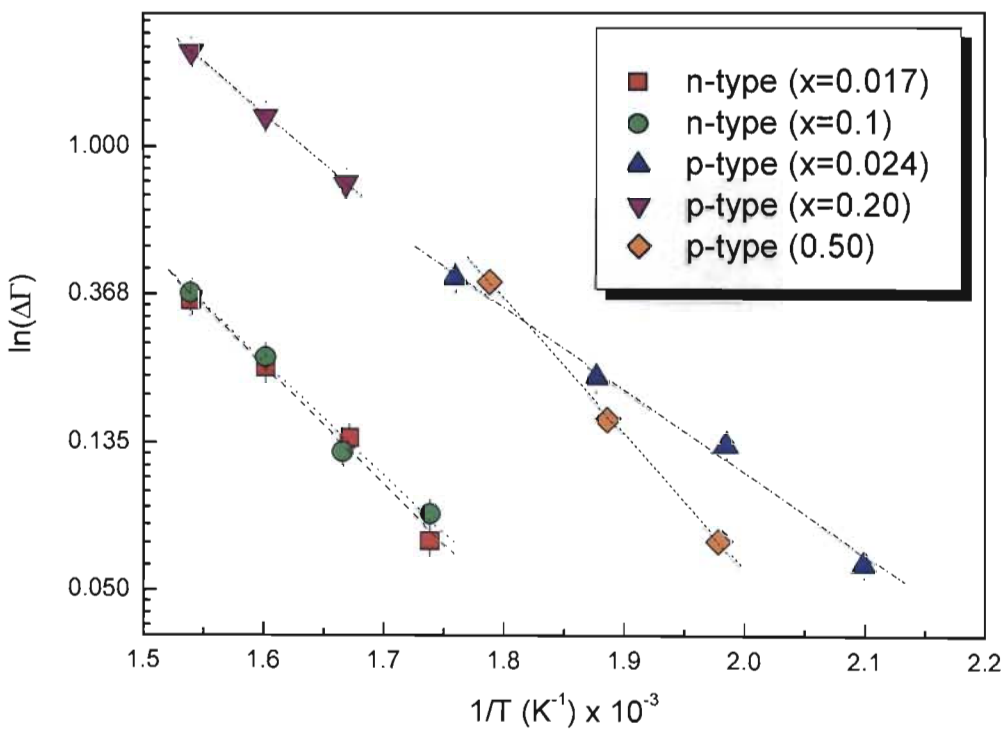

Figure 4.25: **Line broadening as a function of the inverse of temperature for n- and p-type $Si_{1-x}Ge_x$ samples.**

The extracted values for E_a and D_o are compiled in Table 4.6 for different sample types and increasing Ge concentration.

Table 4.6: Diffusion parameters of $Si_{1-x}Ge_x$ for various Ge concentrations.

n-type (P-doped)			p-type (B-doped)		
x	E_a (eV)	D_o (cm^2/s)	x	E_a (eV)	D_o (cm^2/s)
0.017	0.69(7)	0.20	0.024	0.48(7)	0.27
0.05	0.67(7)	0.20	0.083	0.37(7)	0.37
0.1	0.73(7)	0.54	0.20	0.60(7)	0.20
			0.50	0.78(7)	0.11

For the p-type $Si_{1-x}Ge_x$, as the Ge content increases, the E_a values increases quite significantly. In a recent study, Mesli and Nylandsted Larsen[79] performed isothermal annealing measurements in $Si_{1-x}Ge_x$ and determined the activation energies for x = 0.05 and 0.015 as 0.76(3) and 0.75(3) eV, respectively, which are in good agreement with our values for *n*-type SiGe.

Our results are also consistent with the diffusion behaviour of B and P in $Si_{1-x}Ge_x$[80] grown by molecular beam epitaxy. The activation energies and pre-exponential factors of B and P as a function of Ge concentration are shown in Table 4.7. A comparison with our results in Table 4.6 shows that the activation energy for Fe diffusion in SiGe is much lower, attesting that it is a fast diffuser in SiGe (and in Si). In P diffusion, the diffusivity increased with Ge content upto x = 0.24, and then remained relatively constant for higher Ge content. The increase in activation energy with increasing Ge content was explained in terms of the decrease in formation enthalpy of point defects with increasing x and by the elastic properties of SiGe. Christensen[81] showed that B diffusion in relaxed $Si_{1-x}Ge_x$ (x = 0, 0.11 and 0.19) decreases with increasing Ge content whereas Zangenberg *et al.*[80] found a small Ge concentration dependence on individual diffusivities.

Table 4.7: Activation energies (E_a) and pre-exponential factors (D_o) of B and P as a function of Ge concentrations[80].

P			B		
x	E_a (eV)	D_o (cm^2/s)	x	E_a (eV)	D_o (cm^2/s)
0	2.80	2.0×10^{-3}	0	2.68	3.4×10^{-4}
0.07	3.24	1.8×10^{-1}	0.01	3.13	3.4×10^{-2}
0.12	3.11	1.1×10^{-1}	0.12	3.30	2.4×10^{-1}
0.24	4.01	1.7×10^{3}	0.24	3.18	5.7×10^{-2}
0.40	3.83	1.7×10^{2}			

In the diffusion studies performed by Laitinen *et al.*[82], the results obtained for As in relaxed SiGe are compared with the Sb[83] and Sn[84] data. The diffusion parameters for these measurements are summarized in Table 4.8.

Table 4.8: Comparison of activation energies (E_a) and pre-exponential factors (D_o) of Sn, Sb and As in $Si_{1-x}Ge_x$ for various Ge concentrations.

Sn[84]			Sb[83]			As[82]		
x	E_a (eV)	D_o (cm^2/s)	x	E_a (eV)	D_o (cm^2/s)	x	E_a (eV)	D_o (cm^2/s)
0	4.91	5.0×10^{3}	0	4.08	20	0	3.81	4.3
0.21	4.61	8.0×10^{3}	0.1	4.07	40	0.20	3.83	30
0.53	3.88	8.0×10^{2}	0.2	4.07	130	0.35	3.68	23
1	3.05	1.5×10^{2}	0.3	3.89	80	0.5	3.47	18
			0.5	3.63	420	0.65	3.16	16
						0.80	2.97	11
						1	2.42	6

The behaviour of As diffusion parameters resembles that of Sb, where both the E_a and D_o values decreases as the x increases. The diffusion parameters for Sb are slightly lower as a result of different experimental techniques. Although these parameters for Sn show similar trends to Sb and As, the D_o value is 2 to 3 orders of magnitude higher.

Previous self-diffusion[85-87] studies have shown that for x>0.35, diffusion in $Si_{1-x}Ge_x$ is vacancy dominated and diffusion of As in Ge was also due to vacancy mechanisms[88]. The activation energies determined by Laitinen *et al.*[82] as compared to Ge self-diffusion values in $Si_{1-x}Ge_x$ for $0.35 < x \leq 1$, shows that the SiGe composition is very similar but approximately 0.5 eV lower. Therefore, it was suggested that the vacancy mechanism dominates for As diffusion in SiGe for $0.35 < x \leq 1$. The decrease observed in the activation energies as x increases was then explained in terms of the decrease in vacancy formation energy and theoretical calculations[89]. In a previous study, Laitinen *et al.*[90] conducted self-diffusion studies of ^{31}Si and ^{71}Ge in relaxed $Si_{0.20}Ge_{0.80}$ layers and found that there was a transition of the diffusion mechanism of ^{71}Ge from interstitial-type ($x < 0.25$) to vacancy type ($x > 0.25$).

Figure 4.26 shows the line broadening of the interstitial line as a function of temperature in n-type $Si_{1-x}Ge_x$ (x = 0.017, 0.05, and 0.10) and p-type $Si_{1-x}Ge_x$ (x = 0.024, 0.083, 0.20 and 0.50) samples. The broadening in the p^+-type material is greater than the n^+-type material which is consistent with the results obtained in Si[44] for n^+ and p^{++} materials. The line broadening of the n-type samples are similar and the same trends were found as for the p-type materials.

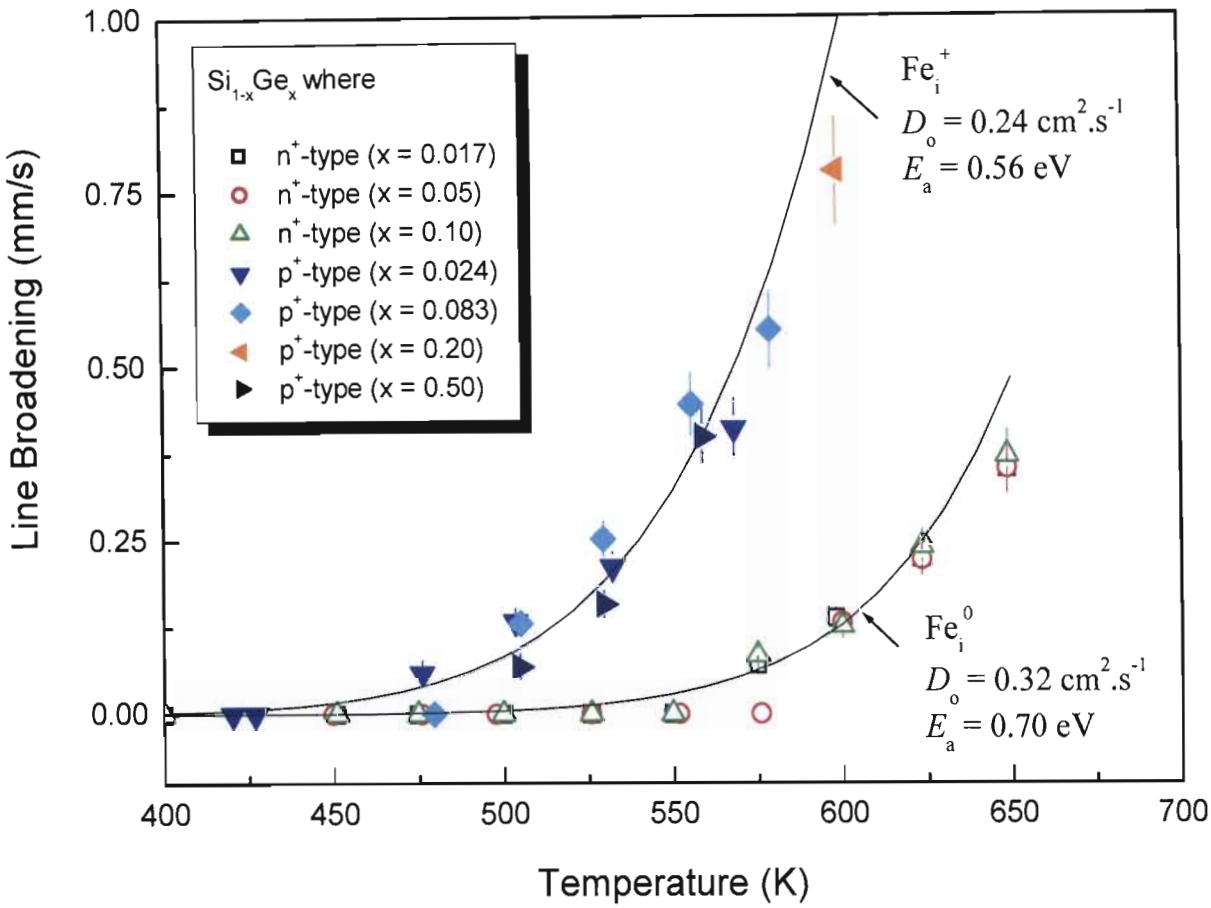

Figure 4.26: **Line broadening as a function of temperature for n-type and p- type $Si_{1-x}Ge_x$ samples of varying Ge composition, x. The solid line is the expected broadening for pure Fe_i^+ and Fe_i^0 for $Si_{1-x}Ge_x$ constructed from was** $D(Fe_i^+) = 0.24\ \exp(-0.50\ \text{eV}/kT)\ \text{cm}^2/\text{s}$ and $D(Fe_i^0) = 0.32\ \exp(-0.70\ \text{eV}/kT)\ \text{cm}^2/\text{s}$.

The average values for D_o ($\bar{D}_o$) and E_a was obtained with fairly reasonable accuracy in a rather limited temperature range 450-650 K. The values for $\bar{D}_o$ that best fitted our data were 0.24 and 0.32 cm^2/s for the Fe_i^+ (ionized charged state) and Fe_i^0 (neutral charge state),

respectively. The corresponding average activation energies for these two states were determined as 0.56(7) and 0.70(7) eV. The solid line shown in Figure 4.26 represents the line broadening for pure Fe_i^+ and Fe_i^0 for $Si_{1-x}Ge_x$ and was constructed from $D(Fe_i^+) = 0.24\ \exp(-0.50\ \text{eV}/kT)\ \text{cm}^2/\text{s}$ and $D(Fe_i^0) = 0.32\ \exp(-0.70\ \text{eV}/kT)\ \text{cm}^2/\text{s}$. The activation energy value obtained for Fe_i^+ is in reasonable agreement with the values determined for Si by Heiser and Mesli[40], 0.69 eV and Takahashni *et al.*[91], 0.68 eV and the value obtained for Fe_i^0 from the present data is also compatible with their values of 0.84 and 0.80 eV which were determined from high temperature data. Our results show conclusively that the diffusivity of Fe_i^+ is larger than that of Fe_i^0 for $Si_{1-x}\ Ge_x$ ($x \leq 0.10$) samples even though diffusion analysis was restricted to a limited temperature range of 450-650 K. In this temperature range, the intensity of the Fe_i-V line was small to affect this conclusion.

4.4 Comparison of Diamond, Si, Ge and SiGe results

Figure 4.27 shows a comparison of the isomer shifts and quadrupole splittings as a function of the bond length, i.e. the nearest neighbours (nn) distance for diamond, Si, $Si_{0.50}Ge_{0.50}$, α-Sn and Ge. The diamond, Ge and $Si_{0.50}Ge_{0.50}$ data were obtained from this work, the Si data[44,45,47] from ^{57}Mn implantations and the α-Sn[92] data from ^{57}Co implantations. Due to large amount of data obtained from our experiment, only the diamond, $Si_{0.50}Ge_{0.50}$ and Ge results are shown in Figure 4.27. The slight variation in results is due to the different dosages of Fe impurities in the different experiments and also the different ways in which temperature dependent measurements were conducted.

The Ge-Ge, Ge-Si and Si-Si bond lengths are close to the Pauling limit[93], but show a small composition dependence hence there is no need to include the isomer shift and quadrupole splitting values for other Ge concentrations. According to the radial force model (RFM)[94,95], at x = 1.0, the Ge-Ge bond length is equal to the natural Ge-Ge bond length

(2.4498 Å) and at x = 0, the Si-Si bond length is equal to the natural Si-Si bond length (2.3516 Å) and these values are consistent with the result obtained by the tight-binding bond orbital model (BOM)[96]. Therefore, for x = 0.5, the Ge-Si bond length is taken as the average of the Si-Si and Ge-Ge bond lengths which is 2.4007 Å.

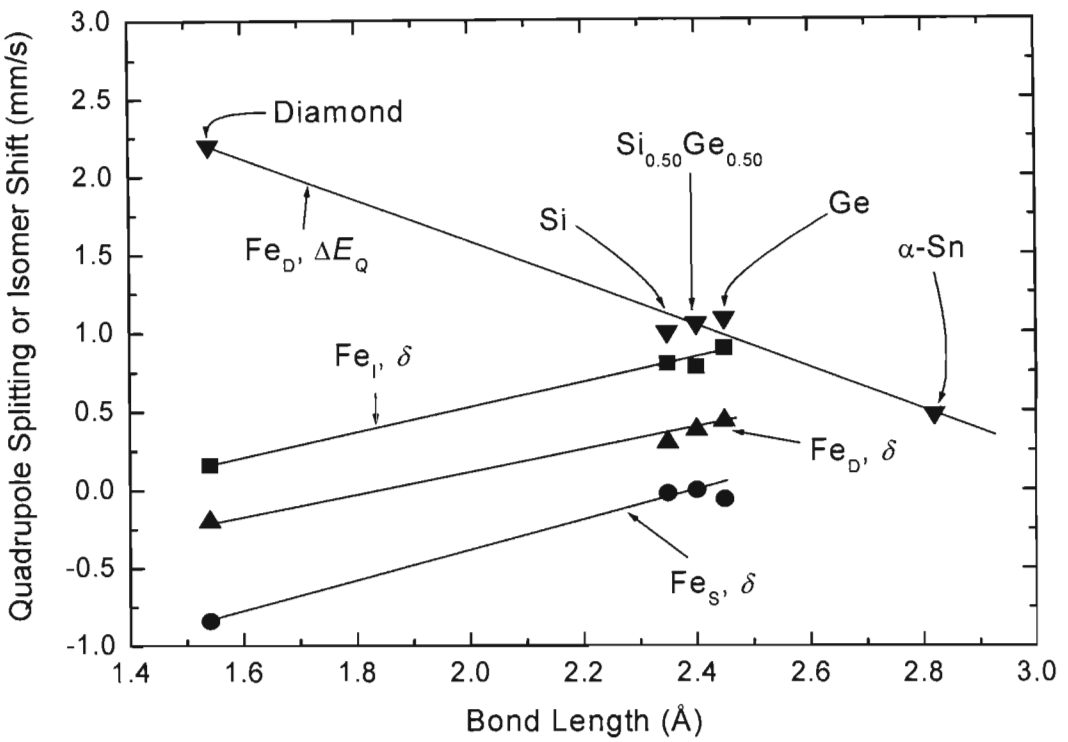

Figure 4.27: Quadrupole splittings and isomer of shifts of Fe_D, Fe_I and Fe_S at room temperature as a function of bond length in group IV semiconductors.

The graph shows two striking features: Firstly, a linear dependence between the bond lengths of the different materials and their isomer shifts and quadrupole splittings which implies that these materials have similar local structures and secondly, the isomer shift of all spectral components show a similar increase i.e. a decreasing *s*-electron density with increasing nearest neighbourhood distance. Further, the *s*-electron density at the substitutional sites in diamond, Si and Ge is larger than the electron density at low

symmetry interstitial sites which can be explained by the compression of the electron shell volume of the Fe atoms in the above matrices. The compression is greater for Fe in non-damaged regions and is greatly reduced in defective regions (higher *s*-electron densities at HS in comparison to LS sites).

Gunnlaugsson *et al.*[44] suggested that the Fe_D in the defect site to be 4-fold coordinated and that the Fe Debye temperature was determined to be comparable to that of a substitutional location in crystalline-silicon. Therefore, one can conclude that the local atomic surrounding is alike to that in amorphous-silicon with locally distorted bonds of four nearest neighbours which is consistent with the recently proposed model of 4-fold coordinated point defects put forward by Cargnoni *et al.*[97] and Goedecker *et al.*[98]. Therefore, it can be envisaged that such defects of similar nature can be formed in all group IV elements and its alloys upon implantation.

Chapter 5

CONCLUSIONS

The spectra for all diamond samples at temperatures < 500 K were dominated by two broad doublets (D1 and D2) associated with Fe atoms resting at low-symmetry sites. The doublets were fitted consistently through the temperature range and their isomer shift values compared favourably with those obtained by Bharuth-Ram *et al.*[74]. An additional doublet (D3) was included at the wings of the resonance spectra for the Conversion Electron Mössbauer Spectroscopy (CEMS) measurements on High-Temperature High-Pressure (HTHP) synthesized diamond which could be due to Fe-N complexes. The sudden collapse of the resonance spectra obtained from the CEMS Chemical Vapour Deposition (CVD) synthesized diamond measurements is indicative that a large fraction of the implanted Fe, presumably in graphitized complexes close to the grain surface, had diffused out of the sample. The type Ia HTHP sample used consisted of appreciable (ppm) nitrogen atoms at single substitutional sites which presumably serve as trapping centres for the Fe atoms which results in these complexes.

In both the Conversion Electron Mössbauer Spectroscopy and Mössbauer Spectroscopy following implantation of ^{57}Mn measurements on the diamond samples, the isomer shifts of the substitutional line (S1) and the interstitial line (S2) were determined to be in the range -0.84 to -0.95 mm/s and -0.02 to 0.17 mm/s, respectively. The isomer shift value of S2 is compatible with the value of 0.16 mm/s obtained by Bharuth-Ram *et al.*[74] and the corresponding value for S1 is in very good agreement with the value of -0.95(3) mm/s

observed by de Waard and co-workers[25,28,30,71,72]. The high-symmetry component (S1) observed in the CEMS CVD diamond and the ^{57}Mn measurements after implantation into Type IIa and CVD diamond were pronounced due to the annealing of implantation damage. This component was also clearly evident in the data obtained by de Waard and co-workers and showed appreciable strength at temperatures greater than 800 K.

Theoretical calculations have been performed to identify the implantation sites of the Fe nuclei in diamond within the local density approximation of spin-density functional theory (LSDA)[74]. These calculations give rise to an isomer shift value of 0.22 mm/s for interstitial Fe on tetrahedral sites and values of 0.09 (unrelaxed lattice) and -0.19 mm/s (slightly relaxed lattice) for the substitutional Fe. The isomer shift of S2 (-0.02 to 0.17 mm/s) obtained in the current measurements compares well with the theoretical calculations for the interstitial Fe, however, the isomer shift of single line, S1 (-0.84 to -0.95 mm/s) differs from the theoretical values of substitutional Fe since the approximations have limitations to take into account the high compressional forces acting on the *s*-electron shell of the substitutional Fe.

The Mössbauer spectra recorded after implantation of ^{57}Mn into n-type $Si_{1-x}Ge_x$ (x = 0.017, 0.05 and 0.10), p-type $Si_{1-x}Ge_x$ (x = 0.024, 0.083, 0.20 and 0.50) and intrinsic $Si_{1-x}Ge_x$ (x = 0.80 and 1.0) single crystals held at 300-850 K in the implantation chamber were generally characterized by sites assigned to damage, tetrahedral interstitial Fe, substitutional Fe and Fe_i-V pairs. The efficiency, resolution and superior counting capabilities of the detection system coupled with the accuracy of the ^{57}Mn experiment and the fact that the implantation damage annealed at 475 K during the lifetime of the ^{57}Mn (1.5 min) prior to the decay and measurement of the ^{57}Fe Mössbauer spectra at this temperature and the diffusion of the interstitial sites enabled us to detect the Fe_i-V line which was was not evident in the experimental data obtained with implanted Coulomb excited ^{57m}Fe nuclei[46,88]. This novel approach developed by Weyer[45,64] serve as a mechanism to create radioactive, interstitial ^{57}Fe atoms in the host samples at diffusion

temperatures and allows for the detection of interstitial diffusional jumps by the resulting line broadening in the Mössbauer spectra of the emitted 14.4 keV γ – radiation. For the p-type $Si_{1-x}Ge_x$, as the Ge content increases, the E_a values increased quite significantly. Our results are also consistent with the diffusion behaviour of B and P in $Si_{1-x}Ge_x$[80] grown by molecular beam epitaxy. A comparison with our results shows that the activation energy for Fe diffusion in SiGe is much lower, attesting that it is a fast diffuser in SiGe (and in Si). The activation energies, E_a = 0.70 eV obtained in this work for the *n*-type $Si_{1-x}Ge_x$ is in good agreement with the values of 0.76(3) and 0.75(3) eV for x = 0.05 and 0.015, respectively determined by Nylandsted Larsen[79]. The comparison of diffusion data[82-87] in $Si_{1-x}Ge_x$ either shows good or partial correlation due to possible point defects in different concentrations which are a result of different experimental methods. The diffusion coefficients for neutral and ionized interstitial Fe have been determined from temperature dependent line broadening and we can confidently report that the diffusivity of Fe_i^+ is larger than that of Fe_i^0 for Si_{1-x} Ge_x ($x \leq 0.50$) as in the case of Si[44] .

At room temperature, the isomer shift of the interstitial lines for $Si_{1-x}Ge_x$ ($0.017 \leq x \leq 0.50$) was determined to in the region of 0.77(5) to 0.81(5) mm/s whilst for $x > 0.80$, the isomer value of this line was found to be around 0.90(5) mm/s and these values compare qualitatively well with theoretical calculations of 0.81-0.89 mm/s for tetrahedral interstitial site[76]. The isomer shift of the substitutional lines were determined in the range 0.098(4) to -0.08(4) mm/s and are in good agreement with the values of 0.13 and -0.064 mm/s obtained by theoretical calculations[76,77]. The isomer shift of the interstitial line is found to depend on doping which is predicted by theory[76,77] and the isomer shift of the substitutional lines for the n-, p- and intrinsic type materials were found to be similar. The isomer shift values of the Fe_i-V line for the n-type material (x = 0.017, 0.05 and 0.10) were found to be in the region of 0.37(2) – 0.44 (2) mm/s whilst the isomer shift values for the p-type material (x = 0.024, 0.083, 0.20 and 0.50) were determined in the range 0.25(2) – 0.34(2) mm/s. The isomer shift values for the intrinsic samples were determined to be in the region of 0.33(2) – 0.44 mm/s.

The Debye temperatures were extracted from the line areas of the different spectral components and were obtained for $0.017 \leq x \leq 0.50$ and $x \geq 0.80$. For $0.017 \leq x \leq 0.50$, the measured Debye temperature value of 400(60) K for substitutional site compares well with the theoretical value of 460 K for Si determined by the mass defect approximation[45]. For $x \geq 0.80$, the Debye temperature for substitutional site was found to be 350(50) K and is accordance with the value of 407 K determined by this model. Our results show that as the Ge concentration (x) increases, the Debye temperatures for the different spectral components become significantly smaller.

Our diamond results show that only partial annealing of the implantation damage is achieved as first observed by Braunstein and Kalish[99] in the 1980s. Emission channelling and Peturbed Angular Correlation measurements on In, Cd and Hf implanted diamonds[38] also showed that considerable damage was still present in the vicinity of implanted probe atoms after annealing at high temperatures of 1600 K. However, total annealing has been achieved in the ^{57}Mn measurements in SiGe alloys and Ge single crystals at 475 K. A comparison of the hyperfine results between diamond, Si, SiGe alloys, Ge and α-Sn shows a linear dependence between the hyperfine parameters (isomer shifts and quadrupole splittings) and the bond lengths. This dependence implies that these materials have similar local structures and secondly, the isomer shift of all spectral components show a similar increase i.e. a decreasing *s*-electron density with increasing nearest neighbourhood distance. Further, the *s*-electron density at the substitutional sites in diamond, Si and Ge is greater that the electron density at effective sites which is due to the compression of the electron shell volume of the Fe atoms in the above matrices. This implies that the volume compression is greater in non-damaged regions than in damaged regions in the materials compared above and it is suggested that such defects of similar nature can be formed in all group IV elements and its alloys upon implantation.

The CEMS investigations on the CVD diamond and the MS on the natural IIa and CVD diamonds indicate that substantial amounts of substitutional Fe can be achieved in high purity diamond by either room temperature implantation or annealing above 1400 K or by high temperature implantation. Our results for the synthetic CVD and HTHP diamonds clearly show that high quality nitrogen-free CVD synthesized diamonds are required if synthetic diamond based optoelectronic devices are to be realised. Further, we have gained a better understanding of the diffusivity of Fe in SiGe alloys and Ge single crystals. The results presented in this thesis shows that the spectral features, electronic and vibrational properties for Fe in $Si_{1-x}Ge_x$ ($0.017 \leq x \leq 0.50$) are similar to its behaviour in silicon[44,47], whilst for $x \geq 0.80$ the behaviour is comparable to Fe in Ge.

APPENDIX

The SiGe spectra were fitted with five spectral lines namely, the substitutional (sub), interstitial (int), Fe_i-V pair (vac), right leg damage (rightdam) and left leg damage (leftdam) using a Mössbauer fitting routine called RECOIL in combination with the solver routine in Microsoft Excel. A sample fitting process is shown below for $Si_{0.95}Ge_{0.05}$ alloy and this was applied consistently for all other data. The following procedures were followed for the different sites and other important fitting parameters are discussed.

(a) Substitutional Site

The positions for this site were well defined for all spectra, A1 to A14 (see Figure A for labels) however it was observed that the width in spectra A1 to A3 were larger than the rest, indicative of an additional component, most probably the damage site. Therefore, in the fitting procedure, the position parameter for the substitutional site was allowed to be free in spectra A4 to A14. In these spectra it was assumed that no damage was present. The theoretical positions were calculated using the equation:

$$\delta = \delta_o - \mathrm{SOD}(T, \theta_D)$$

where

δ_o is the isomer shift at room temperature,

T is the temperature in Kelvin,

θ_D is the Debye temperature and

SOD is the Second Order Doppler shift function used in the Microsoft Excel routine.

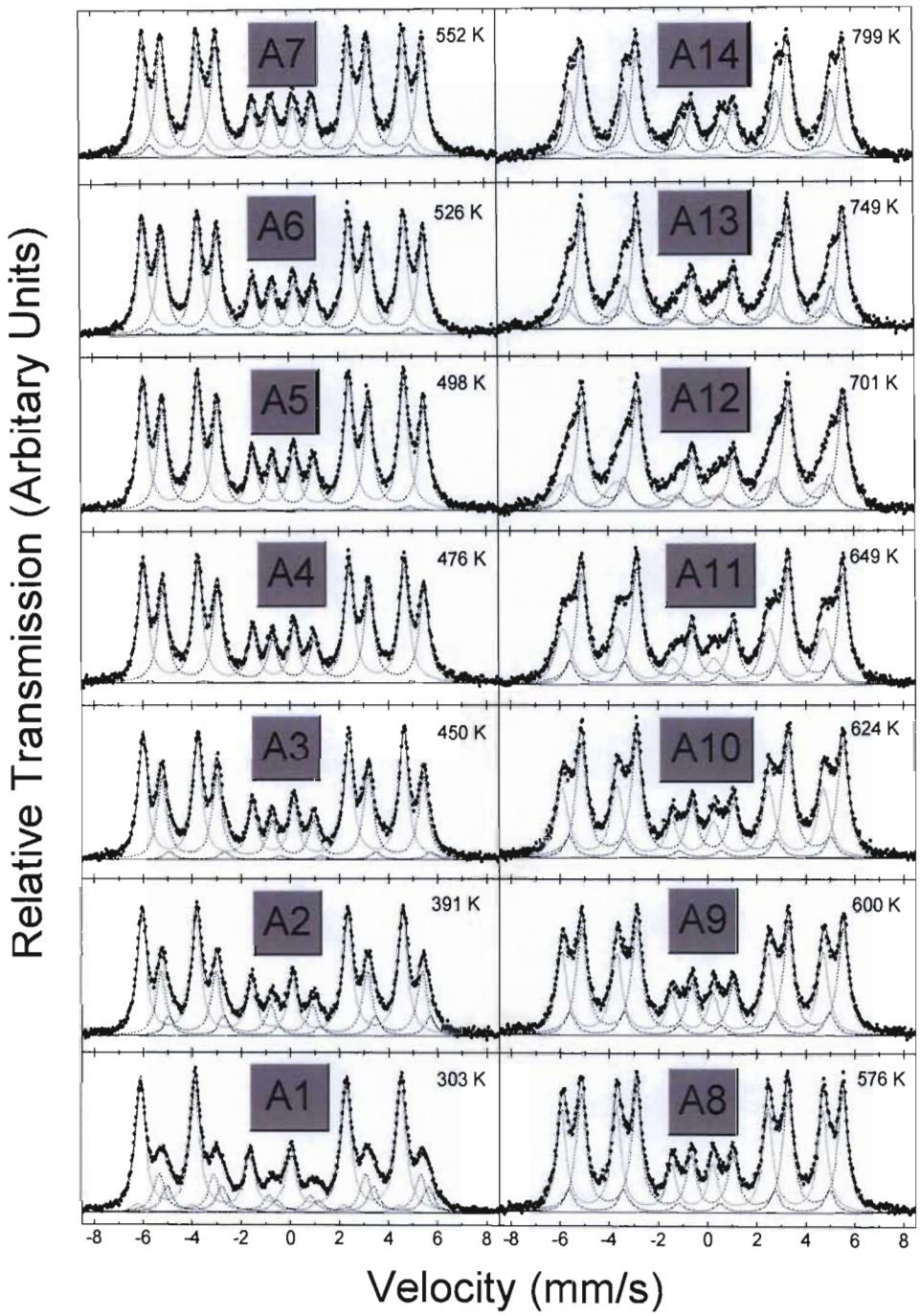

Figure A1: **Analysis of ^{57}Fe Mössbauer Spectroscopy spectra measured after implantation of ^{57}Mn into $Si_{0.95}Ge_{0.05}$ single crystal held at the temperatures indicated.**

The sum of the square of the differences between the calculated and refined values was minimized using the solver function in Microsoft Excel, by optimising the value of is_0 as shown in Table A1. The table below which was extracted from Microsoft Excel shows the maximum difference squared to be 0.0154 mm/s which was obtained from a number trial fits and minimization sequences. The positions of this site in spectra in A1 to A3 were therefore set to the calculated values.

Table A1: Refined and Calculated Isomer Shift values for the substitutional site extracted from RECOIL and Microsoft Excel.

		is_0	0.18 mm/s		
		Debye Temp.	460 K		
Spectra	Temp. (K)	Isomer Shift Refined	Isomer Shift Calculated	Difference	$(Difference)^2$
A1	303	0	-0.07	-0.07	0.0049
A2	391	-0.13	-0.14	-0.01	0.0001
A3	450	-0.13	-0.16	-0.03	0.0009
A4	476	-0.17	-0.19	-0.02	0.0004
A5	498	-0.18	-0.21	-0.03	0.0009
A6	526	-0.20	-0.22	-0.02	0.0004
A7	552	-0.23	-0.24	-0.01	0.0001
A8	576	-0.26	-0.25	0.01	0.0001
A9	600	-0.27	-0.26	0.01	0.0001
A10	624	-0.30	-0.27	0.03	0.0009
A11	649	-0.31	-0.28	0.03	0.0009
A12	701	-0.33	-0.29	0.04	0.0016
A13	749	-0.35	-0.31	0.04	0.0016
A14	799	-0.38	-0.33	0.05	0.0025
				Sum	0.0154

(b) Interstitial Site

The positions of A1 to A7 were refined and the theoretical positions were calculated in a similar way as that for the sub. site and a maximum difference value were obtained similar to the layout in Table A1. For spectra A8 to A15, the positions were fixed to that as the calculated.

(c) Vacancy Pair

At the high temperatures shown in Figure A (spectra A12 to A14), the positions of this site were well-defined; however the interstitial site was still present. Therefore, A14 was chosen to set the positions for this parameter in spectra A1 to A13. In spectrum A14, the position parameter of the vacancy site was allowed to be free.

(d) Damage Site- Right Leg

It was assumed that damage was present at room temperature and from the analysis of the interstitial site, annealing of the damage site occurred as the temperature increased, therefore spectrum A1 was chosen. The position of the substitutional site was fixed at the calculated position and its width was set to a maximum value of 0.08 mm/s (HWHM) which was obtained by the refinement of spectra A4 to A15. The damage site on the right-hand site was added and fitted and the positions for this site for spectra A2 and A3 were determined using the position of A1 as reference. The width of the damage sites in A2 and A3 was set to the value for A1 and then fitted.

(e) Damage Site- Left Leg

The left leg of the damage site was fitted using similar reasoning as that for the right leg of the damage site except for now the interstitial site was important in the fitting process. Spectrum A1 was again chosen, and the position of the interstitial site was fixed at the calculated position as described in part (a). The width of the interstitial site was set to 0.045 mm/s (HWHM) which was the average of the refined widths of A2 to A4 and then the left leg of the damage site was added and fitted into spectrum A1. The positions in A2 and A3 were determined using the position in A1 as a reference.

The damage on both right and left legs was checked for in subsequent spectra, but their contribution was zero, implying that the damage site annealed completely at $\approx$475 K.

Lorenztian Widths

In the initial fitting of all spectra, the lorentzian widths were freed and it was observed that in some spectra the height of the peaks were lower than what they should be resulting in corresponding larger widths in these spectra than those that were well fitted. The lorentzian widths for these spectra were thus taken as the average of the well fitted spectra.

Gaussian Widths

The Fe_i-V pair site was well defined in spectrum A14, therefore its width was refined and chosen for all other spectra. The width of the substitutional site was observed to have an upper limit of 0.08 mm/s (HWHM), therefore the width of A1 and A2 was set to this value. For both the damage sites, the refined widths of A1 were used for A2 and A3.

Gaussian Width for Interstitial Site

As an initial observation, it was found that the widths of A1 and A2 were greater than A3 to A5 and then the widths began to increase until A14. The average of A3 to A5 was taken and the widths of A1 and A2 were set to this value.

Population of Sites

The population of sites were calculated with the assumption there are K sites present in a spectrum at temperature T. Each site has an area A_i and Debye temperature θ_{Di}. The area

A_{BG} due to the background (BG) is multiplied by the velocity range $(V_{256} - V_1)$. The total area is given by:

$$A_{total} = A_{BG} + \Sigma A_i$$

where the contribution C_i due to each component and is given by A_i / A_{total}.

This contribution is related to the number of "particles", N_i in a sample which gives rise to this site via the equation:

$$C_i = ffac(T, \theta_{Di}) * N_i$$

where $ffac(T, \theta_{Di})$ is the recoilless fraction function which is used in the Microsoft Excel solver routine. The number "particles", N_i can thus be determined. The total number of particles, ΣN_i from all components is set to 100 for each temperature range. This is allowed only if there is no overlap of implantation temperatures i.e. they are not recorded in the Mössbauer spectrum for the subsequent temperature. The population of sites were essentially calculated using recoilless fractions and the Debye temperatures of different sites described above.

Quadrupole Splitting

The fitting procedure for all diamond samples was similar to that for SiGe alloys except that the spectral components were different. The diamond data was fitted consistently with two single lines and two quadrupole doublets. The line positions of these components were determined with RECOIL and Microsoft Excel similar to the strategies applied for the SiGe alloys. The theoretical values for the quadrupole splitting were calculated using the formula:

$$\Delta E_Q = \Delta E_{Q,O}\left[1-\left(\frac{T}{T_K}\right)^{3/2}\right]$$

where $\Delta E_{Q,O}$ and T_K are fitting parameters. The slope and the y-intercept variables that appear in Table A2 are due to the manipulation of the equation above. The well defined sites in the diamond data were those at the highest temperatures and they were used as the starting point of the analysis for line positions, widths and quadrupole splittings for the lower temperatures. The minimization procedure resulted in a comparison of theoretical and calculated values which gave a good indication of the various sites within the diamond lattice.

Table A2: Comparison of Experimental and Theoretical Values of Quadrupole Splitting.

Doublet		Slope (m)	-1.1E-05		
		Y-intercept (c)	2.309584		
Temp. (K))	$T^{3/2}$	ΔE_Q (Experiment)	ΔE_Q Theory)	Difference	(Difference)^2
304(1)	5300	2.25	2.25	0.00	0.0000
382(1)	7466	2.21	2.23	-0.02	0.0004
633(1)	15926	2.11	2.13	-0.02	0.0004
770(1)	21367	2.05	2.07	-0.02	0.0004
907(1)	27316	2.02	2.00	0.02	0.0004
1045(1)	33781	1.93	1.93	0.00	0.0000
				Sum	0.0016

REFERENCES

[1] "*Synthetic Diamond Emerging CVD Science and Technology*", Edited by Spear, K.E., and Dismukes, J.P., (Wiley, 1994).

[2] Davies, G. (Ed.), "*Properties and Growth of Diamond*" (IEE/INSPEC, 1994).

[3] Mayer, J.W., and Lau, S.S., "*Electronic Materials and Science for Integrated Circuits in Si and GaAs*" (MacMillan, 1990).

[4] Madelung, O (Ed.), "*Semiconductors: Group IV Elements and III-V Compounds*" (Data in Science and Technology: Springer-Verlag, 1991).

[5] Singh, J., "Physics *in Semiconductors and their Heterostructures*" (MaGraw-Hill, 1993).

[6] Sze, S.M., "*Semiconductor Devices-Physics and Technology*" (Wiley, 1985).

[7] Robertson, R., Fox, J.J. and Martin, A.E., *Phil. Trans. R. Soc.* **A232** 463-535 Scal, M. 1958b, *Proc. Soc. Lond.* **A248** (1934) 379-393.

[8] Sutherland, G.B.B.M., Blackwell, D.E. and Simeral, W.G., *Nature, Lond.* **174** (1954) 901-904.

[9] Clark, C.D., Ditchburn, R.W. and Dyer, H.B., *Proc. Roy. Soc. Lond.* **A234** (1956) 363-381.

[10] Custers, J.F.H., *Physica* **18** (1952) 489-496.

[11] Custers, J.F.H., *Physica* **20** (1954) 183-184.

[12] Hall, H. T., *Review of Scientific Instruments*, **31** (1960a) 125-131.

[13] Wentorf, Jr., R. H., *Journal of Chemistry*, **75** (1971) 1833-1837.

[14] Yazu, S., Tsuji, K. and Yshida, A., *European Patent B01J 3/06,* (1985) *C01 B3106 22222.*

[15] Wentorf Jr., R. H. and Bovenkerk, H. P. *Journal of Chemical Physics*, **36** (1962) 1987-1990.

[16] Wedlake, R. J., *In The Properties of Diamond* (ed. J. E. Field), Academic Press, London, (1979) pp. 501-535.

[17] http://www.onr.navy.mil/sci_tech/information/312_electronics/ncsr/materials.

[18] Sellschop, J.P.F., Connell, S.H., Bharuth-Ram, K., Appel, H., Sideras-Haddad, E. and Stemmet, M.C., *Mat. Sci. Eng.*, **B11** (1992) 227.

[19] Raudies, J.H., Appel, H., Then, G.M. and Thies, W.G., *Hyp. Int.* **15/16** (1983) 487.

[20] Kalish, R., Deicher, M., Recknagel, E. and Weichert, Th., *J. Appl. Phys.* **50** (1979) 6870.

[21] Restle, M., Bharuth-Ram, K., Quintel, H., Ronning, C., Wahl, U., Höfsäss, H. and Jahn, S.G., *Appl. Phys. Lett.* **66** (1995) 2733.

[22] Bharuth-Ram, K., Quintel, H., Restle, M., Ronning, C., Höfsäss, H. and Jahn, S.G., *J. Appl. Phys.* **78** (1995) 5180-5183.

[23] Quintel, H., Bharuth-Ram, K., Restle, M., Ronning, C. and Höfsäss, H., *Nucl. Instr. Meth.* **B118** (1996) 72-75.

[24] Latshaw, G.L., Russell, P.B., and Hanna, S.S., *Hyp. Int.* **8** (1980) 105.

[25] Sawicka, B.D., Sawicki, J.A. and de Waard, H., *Phys. Lett.* **85A** (1981) 303.

[26] Sawicka, B.D., Sawicki, J.A. and Stanek, J., *J. de Phys. Coll.* **37** (1976) C6-882.

[27] Sawicka, B.D., Sawicki, J.A., *Phys. Lett.* **64 A** (1977) 311.

[28] Sawicki, J.A., and Sawicka, B.D., *Nucl. Instrum. Meth.* **B46** (1990) 38.

[29] De Potter, M., Langouche, G., *Z. Phys.* **B53** (1983) 89.

[30] Sawicki, J.A., and Sawicka, B.D., *Nucl. Instrum. Meth.* **194** (1982) 465.

[31] Bharuth-Ram, K., Hatrick, M., Dorn, C., Held, P., Kankeleit, E., Sellschop, J.P.F., Sielemann, R., Wende, L. and Kübler, J., in I. Ortallli (ed.), Proceedings *ICAME 95*, **Vol. 50** 683.

[32] Vavilov, V.S., and Konorova, E.A., *Sov. Phys. Uspekhi* **19** (1976) 301.

[33] Höfsäss, H., Restle, M., Wahl, U., Recknagel, E., *Nucl. Instr. Meth.* **B80/81** (1993) 176.

[34] Quintel, H., Bharuth-Ram, K., Höfsäss, H., Restle, M., Ronning, C., *Nucl. Instr. Meth.* **B118** (1993) 72.

[35] Bharuth-Ram, K., Quintel, H., Restle, M., Ronning, C., Höfsäss, H., Jahn, S.G., *J. Appl. Phys.* **78** (1995) 5180.

[36] Bharuth-Ram, K., Burchard, A., Deicher, M. Höfsäss, H., Quintel, H., Restle, M., Ronning, C., *Phys. Rev.* **B64** (2001) 195207-1.

[37] Prawer, S., Kalish, R., *Phys. Rev.* **B51** (1995) 15711.

[38] Prawer, S., Uzay-Saguy, C., Braunstein, G., Kalish, R., *Appl. Phys. Lett.* **63** (1993) 2502.

[39] Istratov, A.A., Heiselmair, E.R., Weber, E.R., *Appl. Phys* **A69** (1999) 13.

[40] Heiser, T., Mesli, A., *Phys. Rev. Lett.* **68** (1992) 978.

[41] Koveshnikov, S.V., Rozgonyi, G.A., *Appl. Phys. Lett.* **66** (1995) 860.

[42] Heiser, T., Mesli, A., *Appl. Phys. Lett.* **68** (1996) 1868.

[43] Koveshnikov, S.V., Rozgonyi, G.A., *Appl. Phys. Lett.* **68** (1996) 1870.

[44] Gunnlaugsson, H.P., Dietrich, M., Fanciulli, M., Bharuth-Ram, K., Sielemann, R., Weyer, G., The ISOLDE Collaboration, *Physica B* **308-310** (2001) 418.

[45] Weyer, G., Burchard, A., Fanciulli, M., Fedoseyev, V.N., Gunnlaugsson, H.P., Mishin, V.I., Sielemann, R., The ISOLDE Collaboration, *Physica B* **273-274** (1999) 363.

[46] Schwalbach, P., Laubach, S., Hatrick, M., Kankeleit, E., Keck, B., Menningen, M., Sielemann, R., *Phys. Rev. Lett.* **64** (1990) 1274.

[47] Gunnlaugsson, H.P., Fanciulli, M., Dietrich, M., Bharuth-Ram, K., Sielemann, R., Weyer, G., The ISOLDE Collaboration, *Nucl. Intr. and Meth. In Phys. Res. B* **186** (2002) 55.

[48] Gunnlaugsson, H.P., Fanciulli, M., Dietrich, M., Bharuth-Ram, K., Sielemann, R., Weyer, G., The ISOLDE Collaboration, *To be published.*

[49] Nordlund, K., Ghaly, M., Averback, R.S., Cartula, M., Diaz de la Rubia, T., Tarus, J., *Phys. Rev.* **B57** (1998) 7556.

[50] Pelaz, L., Marques, L.A., Gilmer, G.H., Jaraiz, M, Barbolla, J., *Nucl. Instr. and Meth.* **B180** (2001) 12.

[51] Nord, J., Nordlund, K., Keinonen, J., *Phys. Rev.* **B65** (2002) 165329.

[52] Watkins, G.D., Corbett, J.W., *Phys. Rev.* **A543** (1965) 138.

[53] Lee., Y.H., *Appl. Phys. Lett.* **73** (1998) 1119.

[54] Partyka, P., Zhong, Y., Nordlund, K., Averback, R.S., Robinson, I.M., Ehrhart, P., *Phys. Rev.* **B64** (2001) 235207.

[55] Mössbauer, R.L., *Z. Physik,* **151** (1958), 124.

[56] Weisskopf, V., Wigner, E., *Z. Physik* **63**, 54 (1930); **65**, 18 (1930).

[57] Greenwood, N.N., Gibb, T.C., *Mössbauer Spectroscopy* (Chapman and Hall, London, 1971).

[58] Wegener, H.: *Der Mössbauer-Effekt und seine Anwendung in Physik und Chemie-Mannheim* : Bibliographisches Institut, Mannheim (1966).

[59] Wertheim, G.K., and Herber, R.H. *J. Chem. Phys.* **38**, 1206 (1963).

[60] Abragam, A.: *The Principles of Nuclear Magnetism* London-New York: Oxford University Press, Claredon (1961), p. 161.

[61] Wappling, R., *Hyp. Int.*, **47** (1989) 251.

[62] Rose, M.E.: *Multiple Fields*. London: Chapman and Hall (1955).

[63] Cohen-Tannoudji, C., Diu, B., and Lalöe, F., "Clebsch-Gordan coefficients" Complement B, *Quantum Mechanics, Vol 2,* New York: Wiley, , pp. 1035-1047, (1977).

[64] Weyer, G., Degroote, S., Fedoseyev, V.N., Langouche, G., Mishin, V.I., Van Bavel, A.M. and Vantomme, A., *Mater. Sci. Forum* **258** (1997) 437.

[65] Weyer, G., *Nuclear Instruments and Methods*, **186** (1981) 201.

[66] http://www.cern.ch

[67] http://isolde.web.cern.ch/ISOLDE

[68] Ravn, H.L., *Nucl. Instr. Met. B* **26** (1987) 72.

[69] http://www.ifa.au.dk/~hpg/vinda.htm

[70] Lagarec, K., Rancourt, D.G., Extended Voigt-based analytic lineshape method for determining N-dimensional correlated hyperfine parameter distributions in Mössbauer spectroscopy, *Nucl. Instrum. Meth. Phys. Res.* **B129** (1997) 266.

[71] Sawicki, J.A. and Sawicka, B.D., and De Waard, H., *Hyp. Interact.* **15/16** (1983) 483.

[72] Sawicka, B.D., Sawicki, J.A., and Stanek, J., *Phys. Lett.* **59A** (1976), 59.

[73] Ingalls, R., *Phys. Rev.* **155** (1967), 157; **B6** (1972) 41; *Solid State Commun.* **14** (1974) 11.

[74] Bharuth-Ram, K., Hartick, M., Kankeleit, E., Dorn, C., Held, P., Sielemann, R., Wende, L. and Sellschop, J.F.P., *Phys. Rev.* **B58** (1998), 8955.

[75] Weyer, G., Gunnlaugsson, H.P., Dietrich, M., Fanciulli, M., Bharuth-Ram, K., Sielemann, R., The ISOLDE Collaboration, *Nucl. Instr. and Meth.* **B206** (2003) 90.

[76] Kübler, J., Kumm, A.E, Overhof, H., Schwalbach, P., Hartick, M., Kankeleit, E., Keck, B., Wende, L. and Sielemann, R., *Z. Phys.* **B92** (1993) 155.

[77] Lannoo, M, Svane, A., Overhof, H. and Katayama-Yoshida, H, *in "Hyperfine Interactions of Defects in Semiconductors", (Ed. G. Langouche), (Elsevier, Amsterdam* (1992) 379.

[78] Singwi, K.S., Sjölander, A., *Phys. Rev.*, **120** (1960) 1093.

[79] Mesli, A., Nylandsted Larsen, A., *Nucl. Instr. and Meth. In Phys. Res.* **B211** (2003) 80.

[80] Zangenberg, N.R., Fage-Pedersen, J., Lundsgaard Hansen, J., and Nylandsted Larsen, A., *J. Appl. Phys.*, **94** (2003) 3883.

[81] Christensen, J.S., *PhD Thesis*, KTH Microelectronic and Information Technology, Sweden (2004)

[82] Laitinen, P., *PhD Thesis*, University of Jyväskylä, Finland (2004).

[83] Nylandsted Larsen, A., and Kringhoj, P., *Appl. Phys. Lett.*, **68** (1996) 2684.

[84] Kringhoj, P., Elliman, R.G., *Appl. Phys. Lett.*, **65** (1994) 324.

[85] Strohm, A., Voss, T., Frank, W., Laitinen, P., and Räisänen, J., *Z. Metallkd.*, **B93** (2002) 737.

[86] McVay, G.L., and DuCharme, A.R., *Phys. Rev.*, **B9** (1974) 627.

[87] Zangenberg, N.R., Lundsgaard Hansen, J., Fage-Pedersen, J., and Nylandsted Larsen, A., *Phys. Rev. Lett.*, **87** (2001) 125901.

[88] Frank, W., Gösele, U., Mehrer, H., Seeger, A., in *Diffusion in Crystalline Solids*, edited by Murch, G.E., and Nowick, A.S., (Academic , New York, 1984), p.64, and references therein.

[89] Venezuela, P., Dalphian, G.M., da Silva, A.J.R., and Fazzio, A., *Phys. Rev.*, **B65** (2002) 193306.

[90] Laitinen, P., Strohm, A., Huikari, J., Nieminen, A., Voss, T., Crodon, C., Riihimäki, I., Kummer, M., Äystö, Dendooven, P., Räisänen, J., Frank, W., and the ISOLDE Collaboration, *Phys. Rev. Lett.*, **89** (2002) 085902.

[91] Takahashi, H., Suezawa, M., Sumino, K., *Phys. Rev.* **B46** (1992) 1882.

[92] Weyer, G., Grebe, G., Kettschau, A., Deutch, B.I., Nylandsted Larsen, A., Holck, O., *J. de Physique* **C6** 893 (1976).

[93] Pauling, L., *The Nature of Chemical Bond*, (Ithaca, NY: Cornell University Press (1967).

[94] Chen, A.B., Sher, A., *Phys. Rev.* **B32** 3695 (1985).

[95] Shih, C.K., Spicer, W.E., Harrison, W.A., and Sher, A., *Phys. Rev.* **B31** 1139 (1985).

[96] Shen, S.G., Zhang, D.X, and Fan, X.Q, *J. Phys.: Condens. Matter* **7** 3529 (1995).

[97] Cargnoni, F., Gatti, C., Colombo, L., *Phys. Rev.* **B57**, 170 (1998).

[98] Goedecker, S., Deutsch, T., Billard, L, *Phys. Rev. Lett.* **88** (2002) 235501.

[99] Braunstein, G., Kalish, R., *Nucl. Instr. and Meth.* **182/183** (1981) 691: **209/210** (1983) 387.